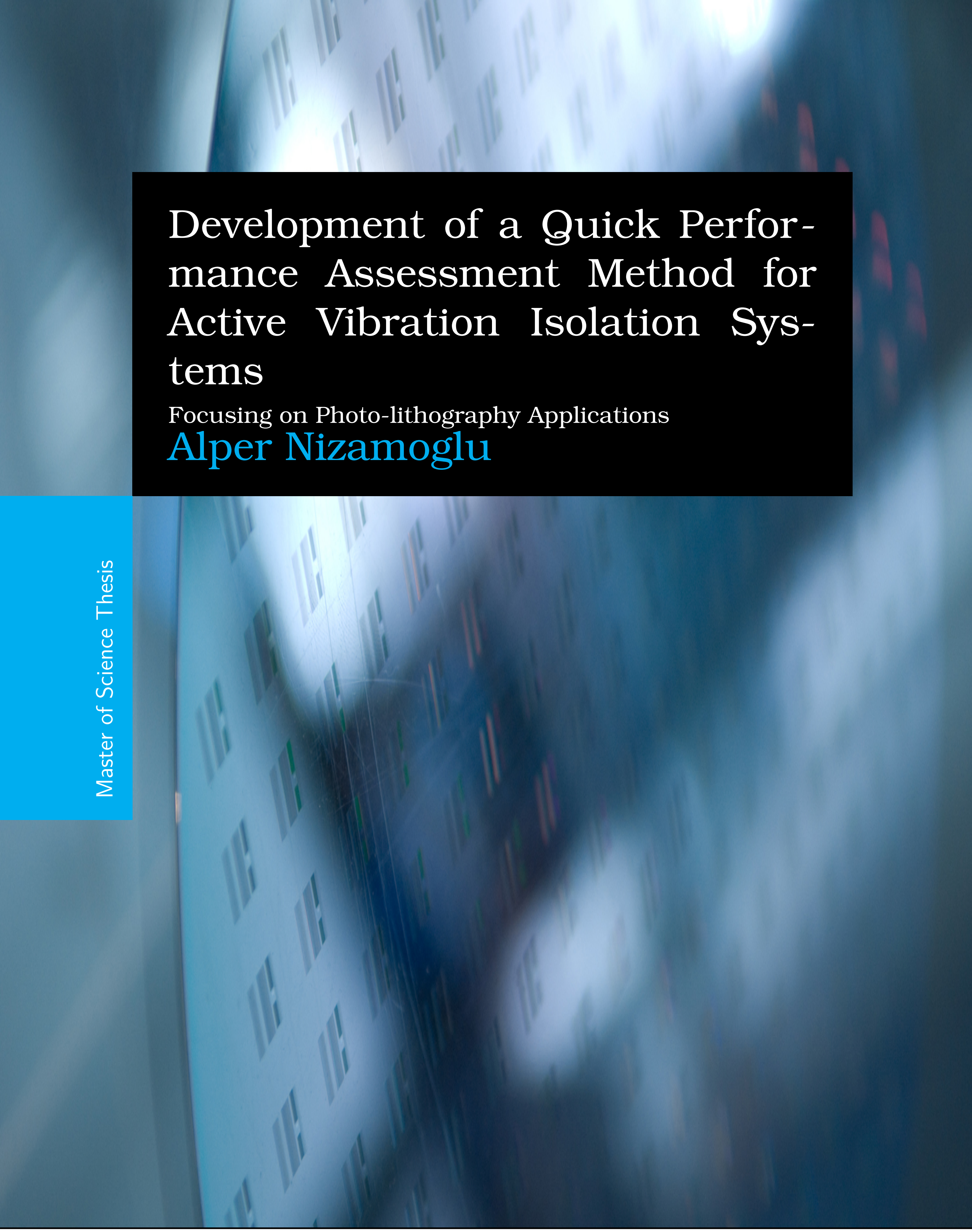

Development of a Quick Performance Assessment Method for Active Vibration Isolation Systems

Focusing on Photo-lithography Applications

Alper Nizamoglu

Master of Science Thesis

TU Delft
Delft University of Technology

Delft Center for Systems and Control

Development of a Quick Performance Assessment Method for Active Vibration Isolation Systems

Focusing on Photo-lithography Applications

MASTER OF SCIENCE THESIS

For the degree of Master of Science in Mechanical Engineering at Delft University of Technology

Alper Nizamoglu

August 17, 2015

Faculty of Mechanical, Maritime and Materials Engineering (3mE) · Delft University of Technology

The work in this thesis was supported by Carl Zeiss Semi-Manufacturing Technology (SMT) Gesellschaft mit beschränkter Haftung (GmbH). Their cooperation is hereby gratefully acknowledged.

Delft University of Technology
Department of
Delft Center for Systems and Control (dcsc)

The undersigned hereby certify that they have read and recommend to the Faculty of Mechanical, Maritime and Materials Engineering (3mE) for acceptance a thesis entitled

Development of a Quick Performance Assessment Method for Active Vibration Isolation Systems

by

Alper Nizamoglu

in partial fulfillment of the requirements for the degree of

Master of Science Mechanical Engineering

Dated: August 17, 2015

Supervisor(s): ____________________
dr.ir. J.W. van Wingerden

____
dr.ir. S. Dietz

Reader(s): ____________________
prof.dr.ir. M. Verhaegen

____
ir. E. van Solingen

Abstract

The performance of high precision applications highly depend on the ability to reject mechanical disturbances. Extreme accuracies can only be achieved if the object can be isolated from its environment. Vibration isolation is the process of isolating an object from the source of vibration. In active vibration isolation, an entire instrument of sensors, controllers and actuators are used to achieve a better performance. Future systems like Extreme Ultra-Violet (EUV) Lithography are expected to rely more and more on active isolation systems, which puts new requirements on analysis and simulation methods.

In high precision applications of complex systems high degree of vibration isolation is needed. In these cases it is required to have a more detailed model of the system, which is usually done with state of the art Finite Element Modelling (FEM) techniques. However, FEM is not appropriate when for example the details of the geometry, location of the isolators or components of the system are not yet known. This typical challenge is to be faced in the concept design phase of the complex systems like EUV-lithography.

In this thesis, we discuss how to develop a methodology with low fidelity models, where we can better understand the system and perform quick system assessment techniques to easily compare various design options. As particular case we derive the 3-Dimensional lumped elements model of the Active Vibration Isolation System (AVIS), defining the disturbance inputs in terms of their spectra and quantitatively measuring the performance of the system by using Cumulative Power Spectrum (CPS) and H_2 norm. Simulation experiments are done to evaluate the performance for different configurations of the system.

Table of Contents

List of Figures

List of Tables

Acknowledgements

Firstly, I want to thank to Michel Verhaegen, Jan-Willem van Wingerden, Martin Rath and Sjoerd Dietz for providing me this valuable opportunity to do my master thesis project at LIT-MMM Department of Carl Zeiss SMT in Germany.

I would like to express my sincere gratitude to my daily supervisor Sjoerd Dietz at Carl Zeiss SMT for sharing his immense knowledge and for the continuous support of my master thesis project. His guidance helped me a lot in all the time of research and writing of this thesis report. I could not have imagined having a better advisor and mentor for my master thesis.

I wish to acknowledge the motivation and support provided by my supervisor Jan-Willem van Wingerden at TU Delft DCSC when finishing my master thesis.

I would like to thank to Helmut Krause, Stefan Otto and Dietmar Neugebauer at Carl Zeiss SMT for sharing interesting knowledge about photo-lithography and active vibration isolation systems.

Lastly, I would like to offer my special thanks to my dear family and friends for their endless support and love.

I hope you will enjoy reading this report.

Delft, University of Technology
August 17, 2015

Alper Nizamoglu

“If the automobile industry had set a pace similar to that of the semiconductor industry, a Rolls Royce would drive 200,000 kilometers per liter of fuel today and it would be cheaper to throw it away than to park it.”

— *Gordon Moore, co-founder of Intel*

Chapter 1

Introduction

Vibration is an oscillatory motion that can cause serious damages to mechanical structures. They can lead to collapse of the buildings, breaking of the machines or decrease in the performance. In order to prevent the failure of a structure or to boost the performance of a system, vibrations need to be isolated.

This thesis focuses on the applications of vibration isolation in semi-conductor manufacturing industry. Therefore, this chapter is to introduce the reader to the vibration isolation problem in photo-lithography. First photo-lithography will be explained with a focus on the last developments in this field. The need for vibration isolation in photo-lithography will be underlined. Second several key concepts in vibration isolation will be summarized and two important techniques to isolate vibrations will be discussed. Last the motivation and the goal of this thesis will be stated.

1-1 Photo-lithography

Lithography is the process of producing electronic chips. Photo-lithography uses the light to make the circuit patterns of a Printed Circuit Board (PCB), hence the name 'photo'-lithography.

The machines that produce the chips using photo-lithography are called wafer steppers. Wafer steppers have 4 important parts: illuminator, reticle stage, projective optics and wafer stage. Figure 1-1 shows a simple description of a photo-lithographic system for chip production.

Illuminator is the source of light, which makes sure that the reticle stage has the optimum lighting.

On the reticle stage lies a photo-mask. The photo-mask is an opaque plate with holes and spaces that allow the light to pass through a defined pattern. The geometric patterns on the photo-mask are to be transferred by the light to the wafer stage.

The projective optics between the reticle stage and the wafer stage is responsible for the accurate guidance of the light beam. This is a special system that consists of lenses and/or mirrors which shrinks 4-5 times the dimensions of the mask. In other words, the projective optics does the exact inverse job of a projector.

Below the projective optics is the wafer stage. On top of the wafer stage lies the silicon wafer. The wafer is coated with light sensitive photo-resist material, which later goes through some chemical process and becomes a chip.

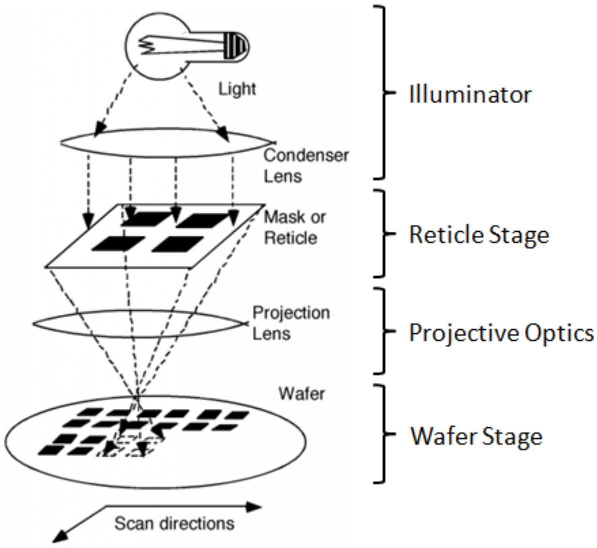

Figure 1-1: Simple Description of Lithographic Chip Production [1]

Another application of photo-lithography with the same procedure is the mask inspection system. The photo-masks that are used in semiconductor production are very fragile and they often need inspection. The inspection is done by projecting the image of the mask onto a camera instead of a wafer stage.

The chips are the heart of all electronic devices that we use in our daily lives. More complex the systems become, larger chips are required for increasing number of structures on the chip. Research and development in this industry involves reducing the sizes of the structures on the chips, which would enable Integrated Circuits (IC) producers more space and more functionality. This is only possible by increasing the resolution in the photo-lithography using technological advances.

1-1-1 Developments in Photo-lithography

We can make a similar analogy between photo-lithography and line drawing to explain the importance of resolution. Assume we have one centimeter square paper, on which we want to draw some vertical lines, where the paper represents the circuit board and the lines represent the circuit patterns. Moreover, we have two pencils for drawing. One of the pencils is sharpened and has a thinner end. With this pencil, we can draw thinner lines with a better resolution and we can fit more lines on the paper. That would allow us to integrate more structures onto the chip.

As the resolution depends on the thickness of the pencil when drawing lines; in photo-lithography systems, the wavelength of the light and the resolution of the optical system have an important effect on the achievable smallest dimension. A general equation for the critical dimension in lithography machines determines the minimum size of a feature that can be possibly projected [6]:

$$CD = k\frac{\lambda}{NA} \tag{1-1}$$

In Eq (1-1), CD is the critical dimension, λ is the wavelength of the light, NA is the numerical aperture which depends on the properties of the optical lenses, and k captures the further process characteristics.

Ultra-violet (UV) lithography uses a wavelength of 193nm. Using UV lithography 50nm precision can be achieved, where the manufacturing tolerance scales of the optical lenses that are used, are at individual atoms [7].

Next generation lithography systems will use Extreme Ultra-Violet (EUV) light, which has 13.5nm wavelength. With EUV technology, a resolution of less than 20nm can be achieved. In order to better appreciate the extreme performance of the EUV lithography, one can compare it to the growth of grass [8]: Grass grows roughly 2cm per week, corresponding to 33nm per second! To be able to achieve this utmost precision, EUV works in vacuum and instead of lens elements, mirrors are used so that the energy is not absorbed by the typical optical system. Production of these mirrors is also very challenging, because they have to be extremely smooth such that if you would compare its surface for example with Germany over a length of 1000km, you would encounter with a mountain of maximum 1mm [9].

To be able to achieve high resolution and produce tiny semi-conductor devices in nanometer levels, the photo-lithography systems must have tight performance criteria. The overall performance of a lithography machine can be split into two main parts. One of them is the performance in terms of optics. The optic performance depends on the quality of the illuminator and the projective optics. The illuminator should provide the EUV light and the projective optics should be able to take care of the even lighting of the mask and accurate guidance of the light beam.

The other performance criteria is about the dynamics of the system. For example in mask inspection systems, the camera and the projective optics should not have any relative motion in order to capture a sharp image of the mask. If they have a relative motion, then one would get a blurry image with a bad resolution. In order to achieve the best performance, it is important to keep the projective optics still. Due to the promising small features of lithographic systems, a small vibration that occur in the surrounding could affect the precision of the lithographic machines. Therefore, vibration isolation systems can improve the dynamic performance of these machines.

In this thesis, focusing on vibration isolation, dynamic performance criteria for lithography machines is investigated. In the next section, vibration isolation systems in photolitography will be introduced.

1-2 Vibration Isolation

The performance of lithographic systems, as used for chip production or mask inspection, strongly relies on the ability to isolate component systems from disturbances that come from floor, water cooling or the light source. In order to handle structures in nano scales, the machines that produce them have to vibrate much less. Therefore, vibration isolation problem is very important for high precision systems.

A simple lumped element model for the lithographic device with an isolation system is provided in Figure 1-2. The device that needs to be kept still is the Projective Optics Box (POB). Therefore, isolators are attached between the device and the base in order to isolate the POB from base vibrations.

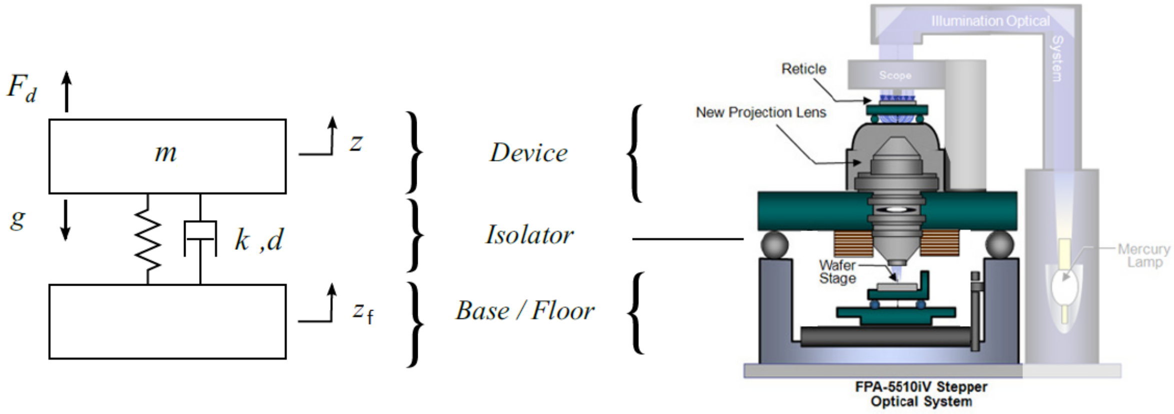

Figure 1-2: Lumped Mass Model of a Lithographic Device [2]

In the literature, mostly two main disturbance sources are defined for isolation systems, the direct force F_d and the floor motion z_f. These disturbances can create motion on the device, hence they need to be suppressed. Two dynamic performance measures need to be mentioned here. One is the compliance, which is the effect of the force F_d on the device motion z. The other is the transmissibility, which is the effect of the floor motion z_f on the device motion z. Whatever the source of disturbance, the aim of the vibration isolators is to keep the objective device motionless.

The isolation is done by means of mounts, k and d. The stiffness of the isolator k together with the mass of the device m determine the suspension frequency of the system f_{susp}. In the literature, the suspension frequency is also called natural frequency (f_n) or eigenfrequency (f_e). A distinction should be made between two classes of mounts for vibration isolation: hard mounts and soft mounts. The division is, somewhat arbitrarily, chosen at $f_{susp} = 5\text{Hz}$, with soft mount systems having a suspension frequency smaller than this value and hard mount systems a higher one [10]. In this thesis soft mount systems are considered. For a good study of hard mount systems, the interested reader can refer to [10], [11].

The compliance and the transmissibility need to be reduced as much as possible for a better performance. If this is translated to systems and control framework, that means the transfer functions from F_d to z and from z_f to z should be as small as possible for a better performance.

These transfer functions for the lumped mass model in Figure 1-2 can be calculated from the equations of motion:

$$m\ddot{z} = F_d + d(\dot{z}_f - \dot{z}) + k(z_f - z) \tag{1-2}$$

Applying the Laplace Transform on (1-2), the transmissibility (T) and the compliance (Q) can be calculated as:

$$T = \frac{z}{z_f} = \frac{ds + k}{ms^2 + ds + k} \tag{1-3}$$

$$Q = \frac{z}{F_d} = \frac{1}{ms^2 + ds + k} \tag{1-4}$$

The aim of the vibration isolation is to have the magnitude of the Frequency Response Functions (FRF) of Q and T as small as possible for the best performance. This can be done by tuning the parameters k and d. This approach is called passive vibration isolation and is explained next.

1-2-1 Passive Vibration Isolation

In the lumped mass model of the system, which can be seen in Figure 1-2, the isolators are modelled by a spring (k) and a damper (d). In passive vibration isolation the goal is to find the optimum values for these tunable parameters. For lithography systems, floor vibration is the main concern, thus transmissibility curve will be used as the performance evaluation. The effect of these parameters on the transmissibility can be seen in Figures 1-3 and 1-4. For this example, the mass is $m = 2$kg. The units of the spring stiffness and damping are N/m and N/(m/s) respectively.

As it can be seen from the Figure 1-3, the stiffness changes the suspension frequency. Increasing stiffness increases both the suspension frequency and the peak. Therefore, a low suspension frequency with low spring stiffness is desired for transmissibility. Air mounts are soft mount vibration isolators which have low stiffness values, hence they are suitable for lithography systems.

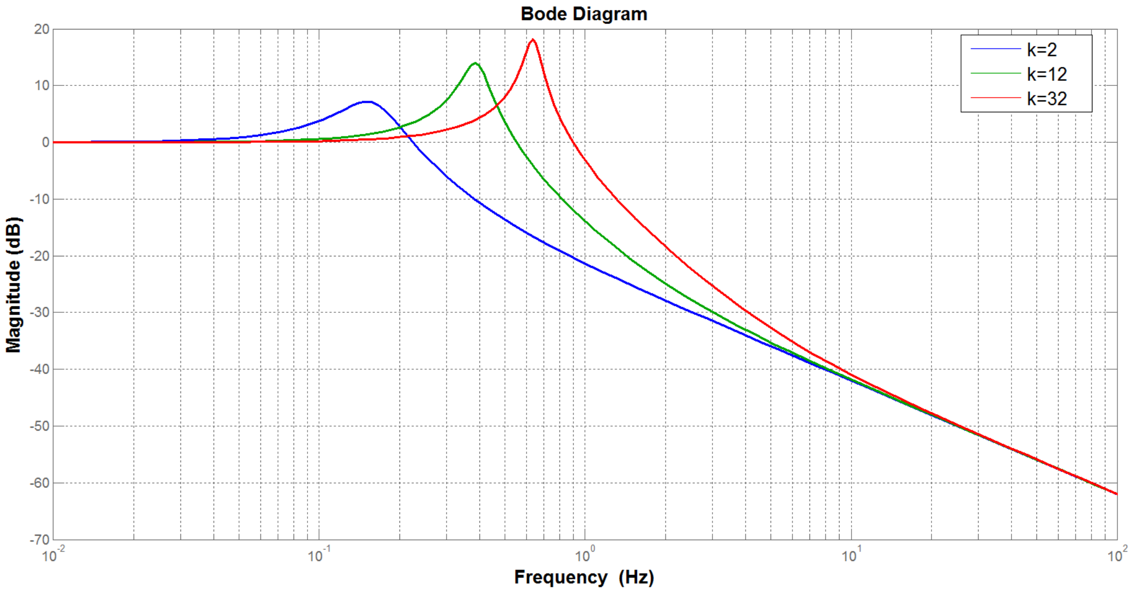

Figure 1-3: Effect of Stiffness on Transmissibility

In Figure 1-4, we see the effect of damping. Damping reduces the peak at the suspension frequency. However, for the frequencies higher than the suspension frequency, the amplification from floor motion to the device motion is increased. This trade-off needs to be tackled, which brings us to the next section: active vibration isolation.

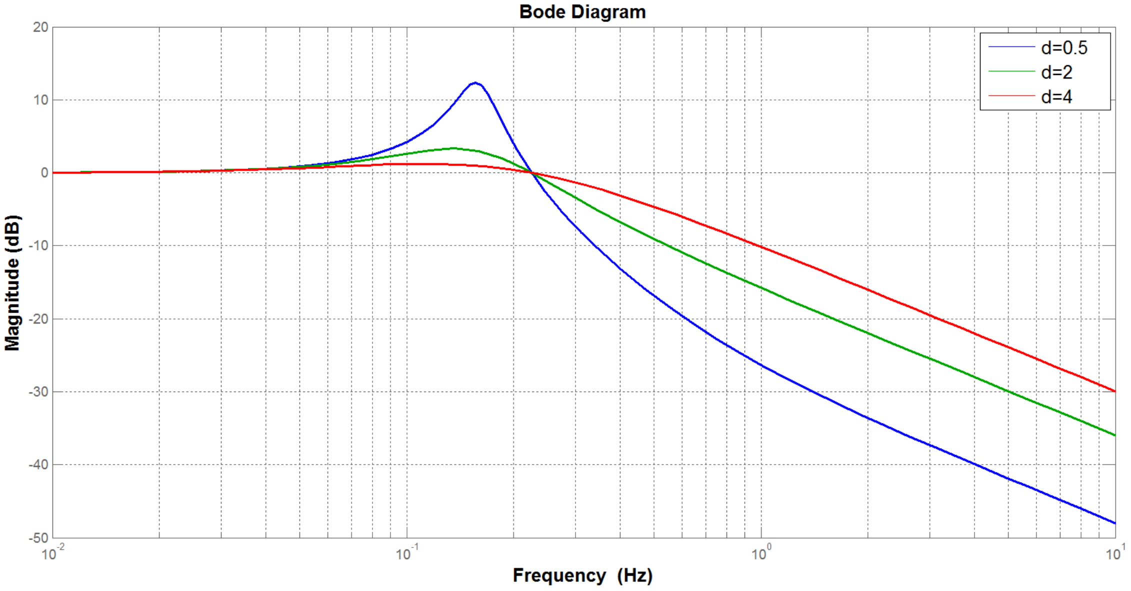

Figure 1-4: Effect of Damping on Transmissibility

1-2-2 Active Vibration Isolation

Passive isolation is incapable of both suppressing the peak at the suspension frequency and achieving a high roll-off at higher frequencies at the same time. This challenge can be attacked by using some control methodology. The most popular strategy is to use absolute velocity feedback with an entire instrument supported by actuators and sensors [12]. Such a system is called Active Vibration Isolation System (AVIS). The lumped mass model for the AVIS is provided in Figure 1-5.

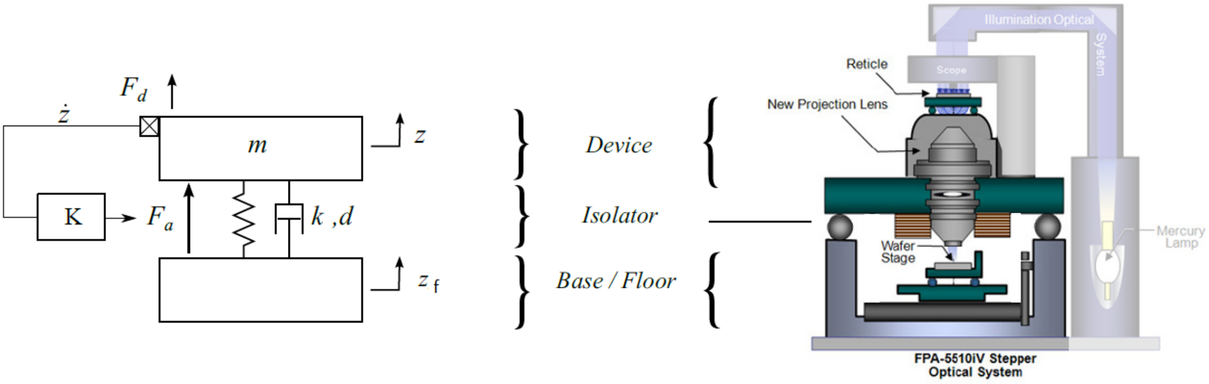

Figure 1-5: Lumped Mass Model for Active Vibration Isolation [2]

As can be seen in Figure 1-5, the velocity of the device $\dot{z}$ is fedback to the controller K, where the isolation is done by the actuator F_a together with the passive elements k and d. This control strategy is called skyhook damping and will be explained in more detail in Chapter 3. For this configuration, the transmissibility function becomes:

$$T = \frac{z}{z_f} = \frac{ds + k}{ms^2 + (d + K)s + k} \tag{1-5}$$

The effect of the active parameter K on the transmissibility can be seen in Figure 1-6. Looking at Figure 1-6, one can derive a fair conclusion that for a better performance, the controller gain K should be increased as much as possible. However, similar to most of the control systems, there is a trade-off between transmissibility and sensor noise sensitivity. Sensor noise sensitivity is the transfer function from sensor noise to the device motion z. It will be explained in more detail in Chapter 3. For the configuration in Figure 1-5, the effect of K on the sensor noise sensitivity is provided in Figure 1-7.

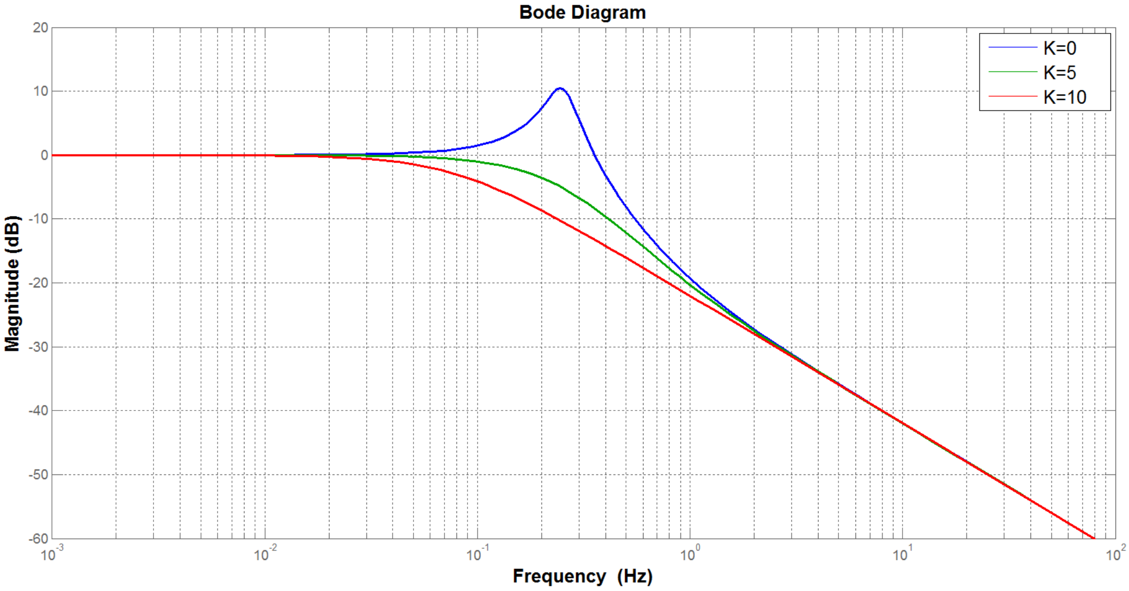

Figure 1-6: Effect of Controller Gain on Transmissibility

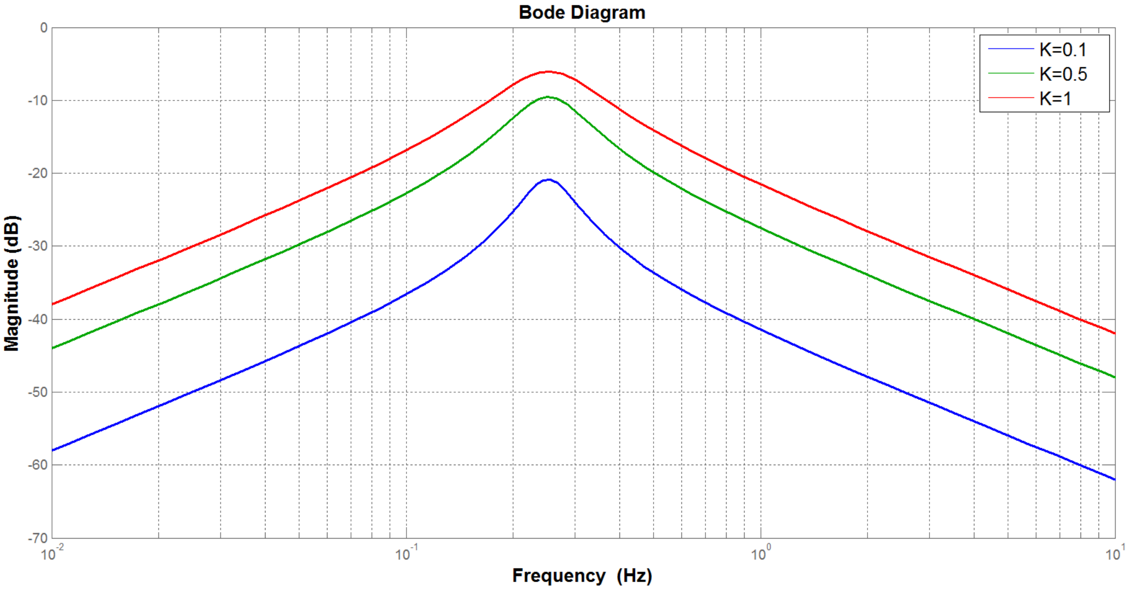

Figure 1-7: Effect of Controller Gain on Sensor Noise Sensitivity

Looking at Figure 1-7 we see that the controller gain amplifies the sensor noise, thus degrading the performance. Therefore, more advanced control methods are investigated in the literature [13].

In this introductory part, the main challenges of vibration isolation systems are briefly explained using a Single Degree of Freedom (SDOF) lumped element model. On the other hand, in 3 Dimensional (3D) space, in order to know the exact position and orientation of a rigid body with respect to a reference frame, one needs 6 Degree of Freedom (DOF) model. Therefore, latest researches in this area use 3D models with 6 DOF to make a more thorough analysis of the vibration isolation system and they focus on finding Multi-input Multi-output (MIMO) control solutions [14] [15] [16].

1-3 Motivation and the Goal of the Thesis

Until now, we introduced the photo-lithography systems with the most recent developments in this technology. It was explained that with the new improvements, these systems require tight dynamic performance criteria in order to be able to handle structures in nano scales. To achieve high performance, the importance of active vibration isolation is underlined. Two important performance criteria are mentioned for evaluating the level of vibration isolation: transmissibility and sensor sensitivity. Furthermore, the effect of passive and active parameters on transmissibility and sensor sensitivity are discussed for SDOF vibration isolation systems.

Future systems like EUV lithography are expected to rely more and more on active vibration isolation systems. Specifications of vibration isolators are mostly based on the SDOF transmissibility curves, which show the suspension frequency and the level of vibration isolation. On the other hand, for high precision applications, SDOF performance criteria is not always enough for a 3D body as the couplings of different DOFs become important for large dimensions. Most of the time, a more detailed modelling is required, which is usually done with state of the art Finite Element Modelling (FEM) techniques. However, FEM is not appropriate when for example the details of the geometry, location of the isolators or components of the system are not yet known. This typical challenge is to be faced in the concept design phase of the complex photo-lithography systems.

Our research question in this thesis is how can we develop a methodology with a simple lumped elements model, where we can better understand the system and perform quick system assessment techniques to easily compare various design options.

The impacts of mass, stiffness, damping and controller gain on the performance of vibration isolation systems are widely studied in the literature. On the other hand, for multiple DOF systems, location of the isolators, gravitational field and coupling between different DOFs also change the dynamic equations. There are several approaches in the literature in recent years, which aim at finding the 6 DOF model of an isolation system based on the physical parameters [17], [18], [11], [3]. Most of these 6 DOF models are based on the older study [19], which provide linear equations describing the rigid body dynamics of a supported mass. However, none of these models show the effect of gravity explicitly. Into our best knowledge, there is no study in the literature for the effect of gravity on the dynamics of a supported rigid body. Therefore, the first step to answer our research question is to derive the analytical model of the system, where the effect of gravitational field is taken into account.

The second step is to define the disturbances of the system. The overall performance of an isolation system depends on the isolation performance of the isolator itself, as well as level of the disturbances. The objective device vibrates around its equilibrium position due to the contributions of different disturbance sources like floor vibration and sensor noise. To assess the performance of the isolation system, floor vibration and sensor noise will be defined in terms of their spectra.

The third step is to introduce quantitative performance measures to compare different system configurations. For vibration isolation, the performance is defined by the standstill specification. Therefore, the standard deviation of the position error resulting from disturbance sources will be calculated. To do this, two performance measures will be discussed: Cumulative Power Spectrum (CPS) and H_2 norm.

1-4 Outline

The thesis explains the methodology that is developed in order to quickly answer design questions about performance, where different system configurations can be simultaneously analyzed.

In Chapter 2, we will derive the equations of motion for two different cases. The first system is a point mass supported by 2 springs. The second system is a 2 Dimensional (2D) body, like a plane supported by 4 springs from below its Center of Gravity (CoG). With the study of these two cases, we will investigate effects of the physical parameters on the dynamics and couplings between different DOFs.

In Chapter 3, we will show the 3D configuration of the air mounts for our model, which puts several constraints on a few parameters. Moreover, we will introduce a method based on [19] to calculate the state space model of 3D passive vibration isolation system. Furthermore, active components of the isolation system will be briefly described and the state space model of the active vibration isolation system will be obtained. We will also put the model in generalized plant framework to easily analyze the transmissibility and sensor noise sensitivity transfer functions.

In Chapter 4, floor vibration and sensor noise modelling will be discussed. Level of floor vibration will be modelled based on general vibration criteria [5]. Moreover, we will discuss a technique [4] to obtain the sensor noise level of the system based on doing some measurements.

In Chapter 5, we will introduce and discuss the applications of two performance criteria, CPS and H_2 norm. Moreover, we will consider a case study, which is a simple design question, that will be attacked by the methodology developed in this thesis.

In Chapter 6, a summary of the methodology and the conclusions will be provided. Lastly, recommendations for future work will be discussed.

Chapter 2

Effects of Physical Parameters in 2D Isolation Systems

We will use a simple shaped rigid body in order to model our objective, which is the Projective Optics Box (POB). We can make a rigid body assumption, because the internal resonances are assumed to occur at higher frequencies. Therefore, the 6 rigid body modes are the most dominant ones for our system and they determine the main characteristics of the dynamics. The rigid body modes can be calculated using mass and stiffness matrices.

Stiffness matrix transforms the relative displacements between two bodies into change of force which is applied by a connection between them. This mapping between displacement and change of force is altered with the configuration of the connection between two bodies. Therefore, the effects of physical parameters and coupling between different Degree of Freedom (DOF)s can be analyzed by obtaining the stiffness matrix for a certain configuration of the system.

In the literature, a common assumption for calculating the stiffness matrix is that the flexible connection stays close to its unloaded configuration. This assumption neglects the effect of gravity, because gravity causes compression at the vertical springs. We want to derive the stiffness matrix for the loaded configuration (meaning that the vertical spring has pre-stress force), such that we can include gravity's effect. [20] discusses a general method to obtain the stiffness matrix for the loaded configuration of the springs. Therefore, we will use his results to model the gravity in our system.

In the first section of this chapter, the method of [20] will be shortly introduced with an example of point mass connected by two springs to the ground. The stiffness matrix will be obtained for a certain configuration of the springs. The resulting stiffness matrix will be used to interpret the effect of gravity and the spring lengths on the dynamics.

In the second part, we will obtain the stiffness matrix for a 2 Dimensional (2D) rigid body, like a plane, supported from below its Center of Gravity (CoG). We will discuss the effects of several physical parameters on the dynamics as well as the coupling between horizontal motion and rotation.

In the last part, we will summarize important results of this chapter.

2-1 Point Mass Supported by 2 Springs

The configuration of a point mass supported by 2 springs is shown in Figure 2-1. Two springs represent a 2D model of an isolator.

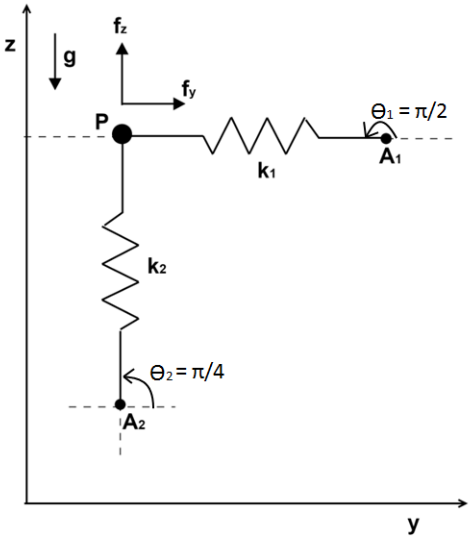

Figure 2-1: Configuration of the Point Mass Supported by 2 Springs

One end of the springs are grounded at A_1 and A_2, other end is pivoted at point P. Cartesian coordinates (y, z) describe the position of P. Moreover, an external force f, is applied to springs at P. The components of f in y and z are denoted f_y and f_z respectively.

The springs apply two independent forces due to the change in their free lengths (L_{01}, L_{02}). Therefore, angles (θ_1, θ_2) and current lengths of the springs (L_1, L_2) are important.

Non-linear Equations for the Stiffness

The stiffness matrix corresponding to the system in Figure 2-1 is defined as the matrix that describes how a change of the position of P leads to a change of the forces act on P by all springs to which it is connected:

$$\begin{Bmatrix} \delta f_y \\ \delta f_z \end{Bmatrix} = \begin{bmatrix} k_{11} & k_{12} \\ k_{21} & k_{22} \end{bmatrix} \begin{Bmatrix} \delta y \\ \delta z \end{Bmatrix} \tag{2-1}$$

where the entries k_{ij} can be found by [20]:

$$
\begin{aligned}
K = \begin{bmatrix} k_{11} & k_{12} \\ k_{21} & k_{22} \end{bmatrix} = \begin{bmatrix} c_1 & c_2 \\ s_1 & s_2 \end{bmatrix} \begin{bmatrix} k_1 & 0 \\ 0 & k_2 \end{bmatrix} \begin{bmatrix} c_1 & s_1 \\ c_2 & s_2 \end{bmatrix} \\
+ \begin{bmatrix} -s_1 & -s_2 \\ c_1 & c_2 \end{bmatrix} \begin{bmatrix} k_1(1-\rho_1) & 0 \\ 0 & k_2(1-\rho_2) \end{bmatrix} \begin{bmatrix} -s_1 & c_1 \\ -s_2 & c_2 \end{bmatrix}
\end{aligned} \tag{2-2}
$$

where c_i =cosθ_i, s_i =sinθ_i and $\rho_i = L_{0i}/L_i$. Note that the angles and the lengths of the springs depend on the position of P in y and z axes.

Linearizing Around the Equilibrium

The stiffness matrix in (2-2) is obtained from the general non-linear equations of motion for any configuration of the springs. On the other hand, for vibration isolation systems, the motion is very small, such that we neglect the change in the lengths and angles of the springs:

Assumption 1: Change in the lengths of the springs are very small.

Assumption 2: Change in the angles of the springs are very small.

According to the Assumptions 1 and 2, the stiffness matrix in (2-2) does not change during the motion. By putting the equilibrium lengths and angles of the springs into (2-2) we can find the constant stiffness matrix that describes the equations of motion around the equilibrium state.

Now we assume that the configuration in Figure 2-1 is the equilibrium, where gravity is acting on the mass along the vertical direction. Therefore, vertical spring is loaded due to gravity, meaning that it has a pre-stress force in the opposite direction of the gravity and equal to the weight of the body. The spring lengths at the equilibrium can then be found as:

$$
\begin{aligned}
L_1 &= L_{01} \\
L_2 &= L_{02} - (mg/k_2)
\end{aligned} \tag{2-3}
$$

Moreover, the angles at the equilibrium are:

$$
\begin{aligned}
\theta_1 &= \pi/2 \\
\theta_2 &= \pi/4
\end{aligned} \tag{2-4}
$$

Now in order to derive the stiffness matrix for the equilibrium state, we just put (2-3) and (2-4) into (2-2).

Accordingly (2-2) becomes:

$$\begin{aligned} k_{11} &= k_1 - mg/L_2 \\ k_{22} &= k_2 \\ k_{12} &= k_{21} = 0 \end{aligned} \tag{2-5}$$

As a result, the stiffness matrix for the point mass, which is supported by the horizontal and the loaded vertical spring at its equilibrium, can be written as:

$$K_{LOADED} = \begin{bmatrix} k_1 - mg/L_2 & 0 \\ 0 & k_2 \end{bmatrix} \tag{2-6}$$

However, if we assume that the vertical spring is not loaded in equilibrium (no pre-stress force due to gravity, $L_2 = L_{02}$), then $-mg/L_2$ term in (2-6) drops out:

$$K_{UNLOADED} = \begin{bmatrix} k_1 & 0 \\ 0 & k_2 \end{bmatrix} \tag{2-7}$$

To summarize, using the results from [20], first we wrote the non-linear equations (2-2). Then using Assumptions 1 and 2, non-linear equations are linearized around the equilibrium state. The stiffness matrix is obtained for both loaded and unloaded configurations of the vertical spring.

On the other hand, we argued that the vibrations in isolation systems are very small. Therefore, a simpler approach to find the stiffness matrix is to directly write the linear equations for the springs. However, we underline that, directly writing the linear equations results in the same stiffness matrix for the loaded and unloaded configurations. In both situations, we obtain the stiffness matrix as in (2-7), where $-mg/L$ term is not there. That means, we lose some dynamics when we directly use the linear equations. Therefore, we should add terms that should represent the neglected dynamics. In the next subsection it will be shown that if we consider the loaded vertical spring as an inverted pendulum, then we capture $-mg/L$ term for the loaded configuration.

Linear Equations for the Loaded Vertical Spring

An inverted pendulum has an unstable equilibrium. Little deviation from the equilibrium results in large motions. Notice that, when the vertical spring is loaded, it acts as an inverted pendulum. Figure 2-2 shows the free body diagram for inverse pendulum configuration. The solid line depicts the loaded vertical spring at its unstable equilibrium where the pre-stress force F_P balances the gravitational force mg. The dashed line shows a little deviation from the equilibrium, where the pre-stress force is separated into its y and z components.

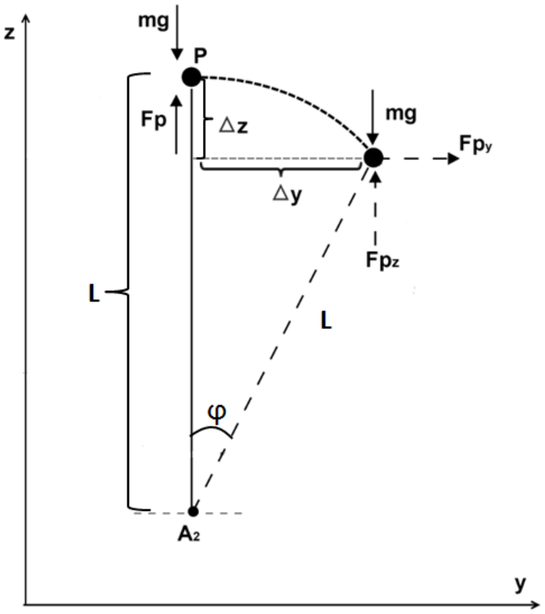

Figure 2-2: Free Body Diagram for Inverse Pendulum

Because of the Assumption 1, the magnitude of the pre-stress force $F_p = mg$ does not change in the deviated position and it acts along the direction of the spring. Using the free body diagram, we can then write the total forces and the displacements in y and z:

$$\begin{aligned} \Delta y &= L\sin\varphi & \sum F_y &= F_p\sin\varphi = mg\sin\varphi \\ \Delta z &= L\cos\varphi - L & \sum F_z &= F_p\cos\varphi - mg = mg\cos\varphi - mg \end{aligned} \tag{2-8}$$

Moreover, due to Assumption 2, we can approximate the sine and cosine functions using 1^{st} order Taylor expansion:

$$\begin{aligned} \sin\varphi &\approx \varphi \\ \cos\varphi &\approx 1 \end{aligned} \tag{2-9}$$

By putting (2-9) into (2-8), we obtain:

$$\begin{aligned} \Delta y &= L\varphi & F_y &= mg\varphi \\ \Delta z &= 0 & F_z &= 0 \end{aligned} \tag{2-10}$$

Hence, the linear relation between the force and displacement in y direction is:

$$\frac{F_y}{\Delta y} = \frac{mg}{L} \tag{2-11}$$

For a spring, this means a negative stiffness, because unlike a vibration around the stable equilibrium, here the force is pulling the pendulum away from its unstable equilibrium. Therefore, it is usually called negative stiffness in the literature:

$$k_- = \frac{-mg}{L} \tag{2-12}$$

Consequently, we showed that, for very small motions, the dynamics of an inverse pendulum can be modelled by an horizontal spring with negative stiffness value. Then we can directly write the linear equations by considering the inverse pendulum configuration of the loaded vertical spring. This way, instead of finding the non-linear equations to analyze the loaded configuration, we can still directly write the elementary linear equations for the springs and add the negative stiffness value due to pre-stress ($-mg/L$) to the horizontal springs. The negative stiffness can be found by dividing the pre-stress force caused by gravity to the length of the vertical spring. Accordingly, we can analyze the effects of gravity and the spring lengths on the dynamics of the system.

In the following parts the symbol ${k_i}'$ will be used for a horizontal spring without the negative stiffness added:

$$k_i = {k_i}' + k_{i-} \tag{2-13}$$

Correspondingly, for horizontal springs, k_i represents spring constant with negative stiffness added.

In the next section, we will calculate stiffness matrix for a two dimensional body, like a plane, which is supported by four springs from below its CoG. We will find the linear equations of motion and calculate the pre-stress force to obtain the negative stiffness due to pre-stress. Effects of the physical parameters and couplings between different DOFs will be discussed.

2-2 2 Dimensional Body Supported by 4 Springs

2-2-1 Description of the Model

Configuration of a 2D body supported by 4 springs is shown in Figure 2-3. Despite not being a complete 3 Dimensional (3D) model, we can still observe effects of several physical parameters on the dynamics by investigating the stiffness matrix. With this model, effects of gravity, spring stiffness, isolator locations and couplings between rotation and horizontal motions will be discussed.

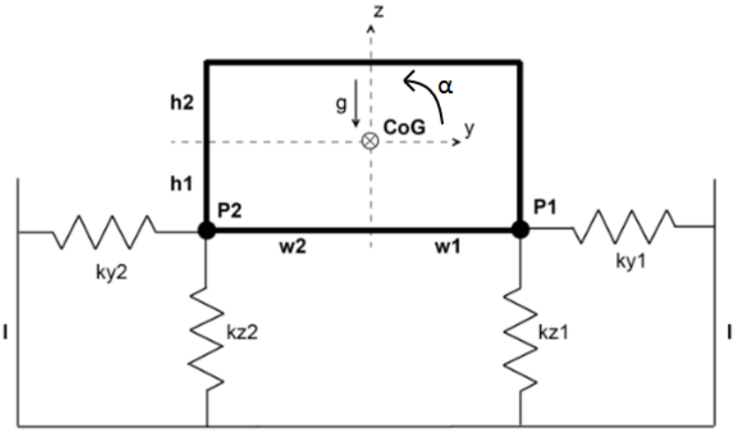

Figure 2-3: 2D Body Supported by 4 Springs

The position and orientation of CoG (y, z, α) is described by relative displacement and rotation of body's coordinate axis attached at CoG to a fixed reference frame. The coordinate axis of the reference frame coincide with the body's coordinate axes in its equilibrium position.

The springs apply forces at points of action (P_1, P_2) along their axis only, which are aligned with (y, z). In order to imply this clearly, the notation for the spring constants are changed compared to the previous section. For example the spring k_{y1} applies force at point P_1 only in y direction. Spring forces F_{yi} and F_{zi} are proportional to spring constants k_{yi}, k_{zi} and displacements of P_i from the equilibrium ΔP_{iy}, ΔP_{iz}:

$$
\begin{aligned}
F_{yi} &= -k_{yi} * (\Delta P_{iy}) \\
F_{zi} &= -k_{zi} * (\Delta P_{iz})
\end{aligned}
\tag{2-14}
$$

where,

$$
\begin{aligned}
\Delta P_{1y} &= P_{1y} - P_{1y0} = y + h_1 \text{sin}\alpha + w_1 \text{cos}\alpha - w_1 \\
\Delta P_{2y} &= P_{2y} - P_{2y0} = y + h_1 \text{sin}\alpha - w_2 \text{cos}\alpha + w_2 \\
\Delta P_{1z} &= P_{1z} - P_{1z0} = z - h_1 \text{cos}\alpha + w_1 \text{sin}\alpha + h_1 \\
\Delta P_{2z} &= P_{2z} - P_{2z0} = z - h_1 \text{cos}\alpha - w_2 \text{sin}\alpha + h_1
\end{aligned}
\tag{2-15}
$$

P_{iy0}, P_{iz0} being the corresponding equilibrium positions of P_i in y and z directions with respect to the CoG. The aim is to obtain equations of motion in terms of generalized coordinates for the CoG about its equilibrium and find the mass and the stiffness matrices, where gravity is the only external force. To do this, we need to calculate the pre-stress forces at the vertical springs.

2-2-2 Finding Pre-stress Forces

In order to calculate the pre-stress forces at springs, we need to make several assumptions about some parameters. All vertical springs are assumed to have same free length L_0 and same length at the equilibrium L. Moreover, the body is assumed to be parallel to the ground at its equilibrium position.

Horizontal distances of the points P_1 and P_2 to CoG are w_1 and w_2 respectively. Vertical distances to CoG are both equal to h_1.

Gravity g acts along $-z$ direction at CoG. Other than gravitation, there is no external force acting on the body. At the equilibrium, vertical springs are assumed to be compressed due to weight of the body mg, which causes pre-stress force.

According to these assumptions, it can be shown that:

$$k_{z1} * w_1 = k_{z2} * w_2 \tag{2-16}$$

Moreover, using the moment equations, we can obtain pre-stress forces $F_{p1,z}$ and $F_{p2,z}$ as:

$$\begin{aligned} F_{p1,z} &= mg * \frac{w_2}{w_1 + w_2} \\ F_{p2,z} &= mg * \frac{w_1}{w_1 + w_2} \end{aligned} \tag{2-17}$$

Adding Negative Stiffness as Caused by Gravity

Due to gravitational force acting on the body, the vertical springs act as an inverse pendulum which results in negative stiffness at horizontal springs. Negative stiffness can be found by dividing the pre-stress forces at the vertical springs $F_{pi,z}$ to the lengths at the equilibrium:

$$\begin{aligned} k_{y1,-} &= -\frac{mg}{L} * \frac{w_2}{w_1 + w_2} \\ k_{y2,-} &= -\frac{mg}{L} * \frac{w_1}{w_1 + w_2} \end{aligned} \tag{2-18}$$

Adding negative stiffness values in (2-18) to the horizontal springs, we can more accurately define the stiffness for horizontal springs as:

$$\begin{aligned} k_{y1} &= k'_{y1} - \frac{mg}{L} * \frac{w_2}{w_1 + w_2} \\ k_{y2} &= k'_{y2} - \frac{mg}{L} * \frac{w_1}{w_1 + w_2} \end{aligned} \tag{2-19}$$

Next, equations of motion around the equilibrium position for CoG of the body will be found and the stiffness matrix will be obtained.

2-2-3 Deriving the Stiffness Matrix

Free body diagram of the 2D body supported by 4 springs in vibration is shown below in Figure 2-4.

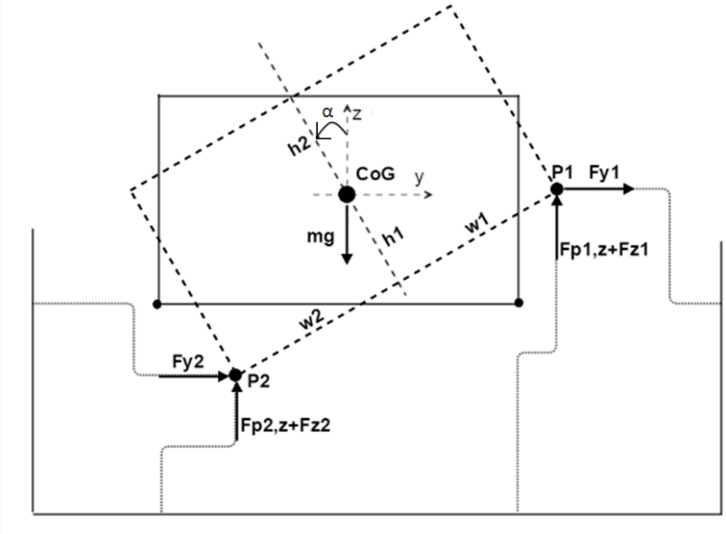

Figure 2-4: Free Body Diagram of 2D Body Supported by 4 Springs

As discussed before, we can assume that angle α always stays close to zero. Hence, we will use the approximation (2-9) due to Assumption 2:

$$\begin{aligned} \sin\alpha &\approx \alpha \\ \cos\alpha &\approx 1 \end{aligned} \tag{2-20}$$

By looking at Figure 2-4, we can sum up the forces and moments at CoG in terms of the generalized coordinates y, z, α:

$$\begin{aligned} \sum F_y &= m\ddot{y} = F_{y1} + F_{y2} \\ \sum F_z &= m\ddot{z} = F_{z1} + F_{p1,z} + F_{z2} + F_{p2,z} - mg \\ \sum M_x &= J_x\ddot{\alpha} = F_{y1} * (h_1 - w_1\alpha) + F_{y2} * (h_1 + w_2\alpha) \\ &\quad + (F_{z1} + F_{p1,z}) * (h_1\alpha + w_1) - (F_{z2} + F_{p2,z}) * (-h_1\alpha + w_2) \end{aligned} \tag{2-21}$$

The forces F_{yi}, F_{zi} and $F_{pi,z}$ are given in (2-14) and (2-17) respectively. By using the approximations in (2-20) they amount to:

$$\begin{aligned}
F_{y1} &= -k_{y1} * \Delta P_{1y} = -k_{y1} * (y + h_1\alpha) \\
F_{y2} &= -k_{y2} * \Delta P_{2y} = -k_{y2} * (y + h_1\alpha) \\
F_{z1} &= -k_{z1} * \Delta P_{1z} = -k_{z1} * (z + w_1\alpha) \\
F_{z2} &= -k_{z2} * \Delta P_{2z} = -k_{z2} * (z - w_2\alpha) \\
F_{p1,z} &= mg * (w_2/(w_1 + w_2)) \\
F_{p2,z} &= mg * (w_1/(w_1 + w_2))
\end{aligned} \tag{2-22}$$

Putting these into the equations of motion (2-21), one obtains:

$$\begin{aligned}
\sum F_y = m\ddot{y} &= F_{y1} + F_{y2} \\
&= -k_{y1} * (y + h_1\alpha) - k_{y2} * (y + h_1\alpha) \\
\sum F_z = m\ddot{z} &= F_{z1} + F_{p1,z} + F_{z2} + F_{p2,z} - mg \\
&= -k_{z1} * (z + w_1\alpha) + mg\frac{w_2}{w_1 + w_2} - k_{z2} * (z - w_2\alpha) + mg\frac{w_1}{w_1 + w_2} - mg \\
\sum M_x = J_x\ddot{\alpha} &= F_{y1} * (h_1 - w_1\alpha) + F_{y2} * (h_1 + w_2\alpha) \\
&\quad + (F_{z1} + F_{p1,z}) * (h_1\alpha + w_1) - (F_{z2} + F_{p2,z}) * (-h_1\alpha + w_2) \\
&= -k_{y1} * (y + h_1\alpha) * (h_1 - w_1\alpha) - k_{y2} * (y + h_1\alpha) * (h_1 + w_2\alpha) \\
&\quad - \Big(k_{z1} * (z + w_1\alpha) - mg\frac{w_2}{w_1 + w_2}\Big) * (h_1\alpha + w_1) \\
&\quad + \Big(k_{z2} * (z - w_2\alpha) - mg\frac{w_1}{w_1 + w_2}\Big) * (-h_1\alpha + w_2)
\end{aligned} \tag{2-23}$$

Using (2-16) and by ignoring higher order terms, the equations in (2-23) can be further simplified to:

$$\begin{aligned}
m\ddot{y} + (k_{y1} + k_{y2}) * y + h_1(k_{y1} + k_{y2}) * \alpha &= 0 \\
m\ddot{z} + (k_{z1} + k_{z2}) * z &= 0 \\
J_x\ddot{\alpha} + h_1(k_{y1} + k_{y2}) * y + \big(h_1^2(k_{y1} + k_{y2}) + w_1^2 k_{z1} + w_2^2 k_{z2} - mgh_1\big) * \alpha &= 0
\end{aligned} \tag{2-24}$$

By partitioning (2-24), we can collect the equations of motion in matrix form using:

$$\begin{bmatrix} m & 0 & 0 \\ 0 & m & 0 \\ 0 & 0 & J_x \end{bmatrix} \begin{Bmatrix} \ddot{y} \\ \ddot{z} \\ \ddot{\alpha} \end{Bmatrix} + \begin{bmatrix} k_{yy} & k_{yz} & k_{y\alpha} \\ k_{zy} & k_{zz} & k_{z\alpha} \\ k_{\alpha y} & k_{\alpha z} & k_{\alpha\alpha} \end{bmatrix} \begin{Bmatrix} y \\ z \\ \alpha \end{Bmatrix} = 0 \tag{2-25}$$

where, J_x is the inertia and the underscore x stands for the third dimension whose positive direction is out of the paper, as right hand rule implies. The stiffness matrix K is then calculated as:

$$K = \begin{bmatrix} k_{yy} & k_{yz} & k_{y\alpha} \\ k_{zy} & k_{zz} & k_{z\alpha} \\ k_{\alpha y} & k_{\alpha z} & k_{\alpha\alpha} \end{bmatrix} = \begin{bmatrix} k_{y1} + k_{y2} & 0 & h_1(k_{y1} + k_{y2}) \\ 0 & k_{z1} + k_{z2} & 0 \\ h_1(k_{y1} + k_{y2}) & 0 & h_1^2(k_{y1} + k_{y2}) + w_1^2 k_{z1} + w_2^2 k_{z2} - mgh_1 \end{bmatrix} \tag{2-26}$$

2-2-4 Discussion

We can look at the symmetric K matrix in (2-26) to observe some important dynamic characteristics of a rigid body supported from below its CoG.

First, couplings between corresponding motions, which are shown by the off-diagonal terms in K matrix, can be analyzed. For this configuration we do not observe any coupling between translational motions y and z, because the spring forces act along the coordinate axes of the CoG. If this is not the case, then orientation of the isolators determine the level of the coupling between translational movements. On the other hand, coupling between rotation α and horizontal translation y depend both on the orientation and location of the isolators. In particular, the level of coupling is proportional to vertical distance between CoG and supports, which is h_1. That means, fully decoupled rigid body modes is only possible if horizontal forces act through CoG.

Second, we can analyze which physical parameters have an effect on the dynamics. K matrix is linearly dependent on the spring stiffness. Moreover, vertical distance of the isolators h_1 also appears linearly for the coupled dynamics. However, the dynamics of pure rotation ($k_{\alpha\alpha}$) is quadratically dependent on the isolator location.

Gravity changes the dynamics as well. To see its effect more clearly, we partition k_{yi} as in (2-13). Accordingly, the stiffness matrix looks like:

$$K = \begin{bmatrix} k'_{y1} + k'_{y2} - \frac{mg}{L} & 0 & h_1(k'_{y1} + k'_{y2} - \frac{mg}{L}) \\ 0 & k_{z1} + k_{z2} & 0 \\ h_1(k'_{y1} + k'_{y2} - \frac{mg}{L}) & 0 & h_1^2(k'_{y1} + k'_{y2} - \frac{mg}{L}) + w_1^2 k_{z1} + w_2^2 k_{z2} - mgh_1 \end{bmatrix} \tag{2-27}$$

Consequently, it is clear that gravity changes the horizontal dynamics, due to the negative stiffness caused by inverse pendulum configuration. This is captured by $-mg/L$ term, which also shows that this effect is proportional to m/L. Moreover, the pre-stress force due to gravity changes the rotational dynamics, which can be seen from $-mgh_1$ term. This term is also important as h_1 can be rather large for lithographic systems.

2-3 Summary

In this chapter, first it was argued that in order to model a 2D vibration isolation system with linear lumped elements, we should add negative stiffness to the horizontal springs. This was motivated with the results from [20]. Second we obtained the 3x3 stiffness matrix of a 2D rigid body with 3 DOF. The resulting stiffness matrix was investigated to analyze the couplings between motions and the effects of several physical parameters. The results of the discussion further motivate us to obtain a complete 3D model of the isolation system to examine effects of different physical parameters and compare various design options. Therefore, in the next chapter, analytical modelling of a 3D rigid body supported by 4 isolators will be studied.

Chapter 3

3D Modeling of the Active Vibration Isolation System

In the previous chapter, the dynamics of a 2 Dimensional (2D) rigid body supported from below its Center of Gravity (CoG) is studied. We have calculated the pre-stress forces for a certain configuration of the system, where the z-mode is decoupled. Using the pre-stress forces of vertical springs, we have obtained the negative stiffness values for horizontal springs.

In this chapter, we will extend this analysis to 3 Dimensional (3D) rigid body and find the equations of motion for the CoG. Again, in order to decouple the z-mode of the system, we will make several assumptions about configuration of the isolators which then introduce constraints on certain parameters.

Manipulating the equations describing the 3D rigid body dynamics with 6 Degree of Freedom (DOF) is rather complicated. Therefore, in the second part, we will introduce a general matrix method from [3] to find the stiffness matrix of a 3D rigid body supported by 4 isolators. Using the parametric stiffness matrix that satisfies constraints on several parameters, state space model of the passive vibration isolation system will be obtained.

In the last part, the active components of the vibration isolation system will be briefly explained. The state space model for passive isolation will be extended to Active Vibration Isolation System (AVIS). As the next step, we will put the model in a generalized plant framework where we can easily calculate the transmissibility and noise sensitivity functions. This chapter concludes the analytical 3D modelling of the AVIS.

3-1 Configuration of the Isolators

The isolators supporting the Projective Optics Box (POB) can be modelled by parallel springs and dampers. However, in this section, they will be represented only with springs for the sake of simplicity.

An illustration of a rigid mass supported by four isolators is shown in Figure 3-1.

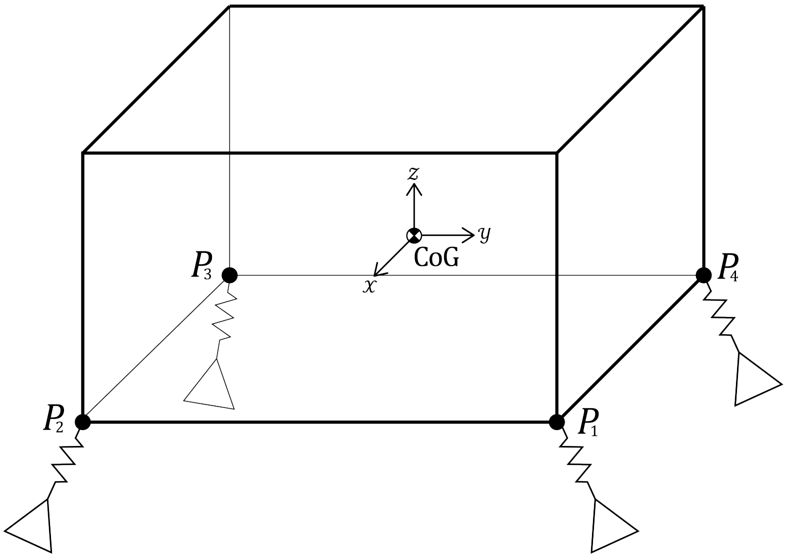

Figure 3-1: Rigid Body Supported by 4 Isolators [3]

The (hanging) body is modelled as a box which is connected to the ground by four isolators located at the points of action P_1, P_2, P_3, P_4. One isolator consists of 3 lumped spring elements (orthogonal springs) that act along 3 axes of a coordinate system with directions p_i, q_i, r_i. Hence, the model of an isolator is:

$$\begin{pmatrix} f_{p_i} \\ f_{q_i} \\ f_{r_i} \end{pmatrix} = \boldsymbol{K_{pi}} \begin{pmatrix} p_i \\ q_i \\ r_i \end{pmatrix} \tag{3-1}$$

where

$$\boldsymbol{K_{pi}} = \begin{bmatrix} k_{pi} & 0 & 0 \\ 0 & k_{qi} & 0 \\ 0 & 0 & k_{ri} \end{bmatrix} \tag{3-2}$$

The rigid body is parallel to the ground at the equilibrium. The origin of the reference frame is CoG of the body with axes x, y, z parallel to the box. Figure 3-2 illustrates the location and orientation of the coordinate axis at CoG and P_i.

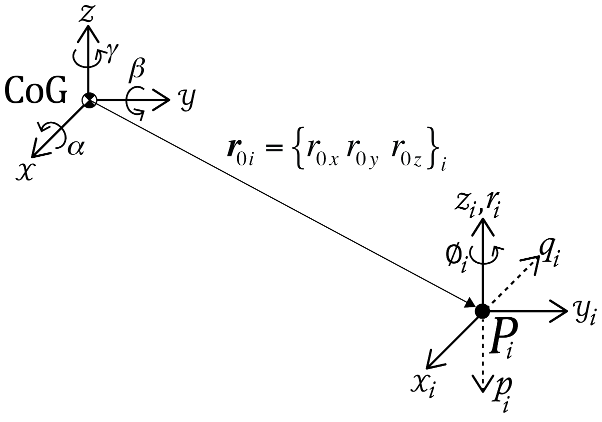

Figure 3-2: Location and Orientation of the Coordinate Axes [3]

The vertical axes of the isolators r_i are aligned with the vertical axis of the body z whereas horizontal springs can be rotated along r_i axis by ϕ_i. Furthermore, we assume that the location of the four isolators have certain symmetry with respect to the CoG. Figure 3-3 shows the configuration of the isolators with respect to CoG of the body.

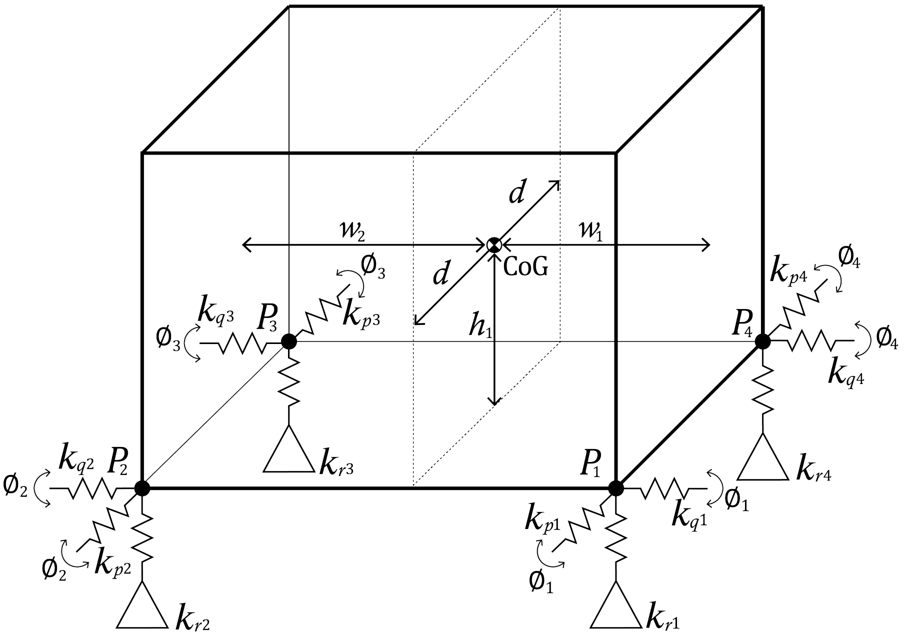

Figure 3-3: Configuration of the Isolators wrt CoG

The distances of the points of action for the 4 isolators with respect to CoG can be found as:

$$\begin{aligned}
\boldsymbol{r_{01}} &= \{r_{0x} \quad r_{0y} \quad r_{0z}\}_1 = \{\ d \quad w_1 \quad -h_1\} \\
\boldsymbol{r_{02}} &= \{r_{0x} \quad r_{0y} \quad r_{0z}\}_2 = \{\ d \quad -w_2 \quad -h_1\} \\
\boldsymbol{r_{03}} &= \{r_{0x} \quad r_{0y} \quad r_{0z}\}_3 = \{-d \quad -w_2 \quad -h_1\} \\
\boldsymbol{r_{04}} &= \{r_{0x} \quad r_{0y} \quad r_{0z}\}_4 = \{-d \quad w_1 \quad -h_1\}
\end{aligned} \tag{3-3}$$

Moreover, the lengths of the vertical springs at the equilibrium are equal to L.

In order to achieve that the rigid body is parallel to ground in equilibrium, we need to add constraints to vertical stiffness values k_{r_i}. To explain this, projections on yz plane and xz plane are illustrated in Figure 3-4.

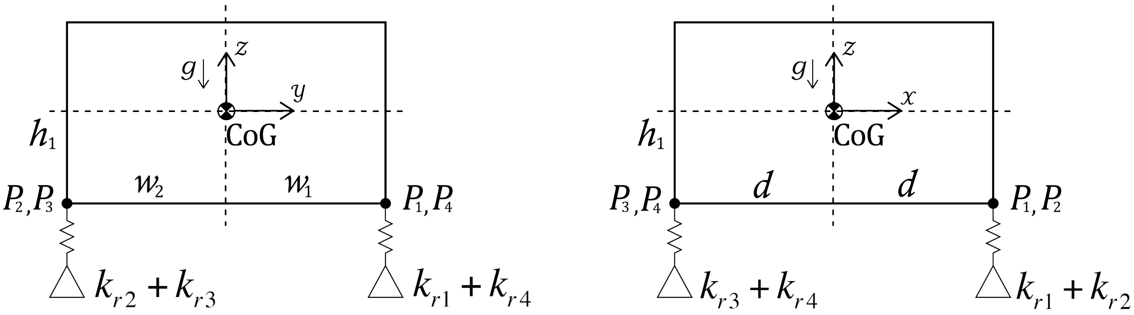

Figure 3-4: Projections on yz Plane (Left) and xz Plane (Right)

From the moment equations around CoG, the relationships between vertical stiffness become:

$$\begin{aligned}
k_{r1} + k_{r2} &= k_{r3} + k_{r4} \\
(k_{r2} + k_{r3}) * w_2 &= (k_{r1} + k_{r4}) * w_1
\end{aligned} \tag{3-4}$$

The gravity g is acting in $-z$ direction. Hence the vertical springs are compressed at the equilibrium due to the weight of the body mg. In order to calculate the pre-stress forces of each spring, we further assume:

$$\begin{aligned}
k_{zR} &= k_{r1} = k_{r4} \\
k_{zL} &= k_{r2} = k_{r3}
\end{aligned} \tag{3-5}$$

where k_{zR} and k_{zL} stands for the vertical stiffness of the right (k_{r1}, k_{r4}) and the left (k_{r2}, k_{r3}) isolators respectively. Consequently, pre-stress forces at the vertical springs can be calculated as:

$$\begin{aligned}
F_{p1,z} = F_{p4,z} &= \frac{mg}{2} * \frac{w_2}{w_1 + w_2} \\
F_{p2,z} = F_{p3,z} &= \frac{mg}{2} * \frac{w_1}{w_1 + w_2}
\end{aligned} \tag{3-6}$$

Accordingly, the negative stiffness for the horizontal springs k_{pi-} and k_{qi-} become:

$$\begin{aligned} k_{q1-} &= k_{p1-} = -\frac{mg}{2L} * \frac{w_2}{w_1 + w_2} \\ k_{q2-} &= k_{p2-} = -\frac{mg}{2L} * \frac{w_1}{w_1 + w_2} \\ k_{q3-} &= k_{p3-} = -\frac{mg}{2L} * \frac{w_1}{w_1 + w_2} \\ k_{q4-} &= k_{p4-} = -\frac{mg}{2L} * \frac{w_2}{w_1 + w_2} \end{aligned} \tag{3-7}$$

Notice that, (3-7) still holds if $\phi_i \neq 0$, because for an inverse pendulum in 3D, it does not matter to which direction the pendulum bends over.

3-1-1 Discussion

In this section, we introduced several assumptions to achieve a certain configuration of the rigid body. These assumptions are:

- the rigid body is assumed to be a box parallel to the ground at its equilibrium, hence the vertical mode is decoupled from other rigid body modes
- the location of the isolators have certain symmetry with respect to the CoG
- the gravity causes pre-stress forces at the vertical springs

As a result, the constraints (3-4), (3-5), (3-6) are needed to satisfy the assumptions.

After all, parameters that remain can be analyzed independently to compare the effects of different parameter values on the dynamics of a 3D rigid body. The free physical parameters for the equations of motion are: mass (m); inertia tensor (J); location of the isolators (h_1, d, w_1, w_2); rotation of the isolators around their vertical axis (ϕ_i); horizontal (k_{pi}, k_{qi}) and vertical (k_{zL}, k_{zR}) stiffness; length of the vertical springs (L) and gravity (g).

3-2 Matrix Equations for Vibration Isolation System

Deriving a complete analytical model for the equations of motion of a 3D rigid body is tedious. Interested reader can refer to Appendix A to see derivation of the parametric 6x6 K matrix for a certain configuration. However, we underline that even with the assumptions made in the previous section, where several parameter values are restricted, manipulating the symbolic equations can be cumbersome. Therefore, we will introduce an algorithm from [3], which can be used to obtain the stiffness matrix. This algorithm is based on the study of [19]. The reader is directed to the original reference [19] for further details on the derivation. Here we show the results according to the assumptions we made in the previous section.

Each isolator has a local axis p_i, q_i, r_i whose origin is located at the point of action P_i. Vectors in (3-3) describe the location of P_i with respect to the CoG.

Displacements and rotations of the CoG are described by a 6x1 vector: $\{x\ y\ z\ \alpha\ \beta\ \gamma\}$. Moreover, $\boldsymbol{r_{0i}}$ describes location and ϕ_i describes vertical rotation of the isolator i. Configuration of the isolators is explained in the previous section and can be seen in Figure 3-3.

Each isolator has translational stiffness along their orthogonal local axes that is described by the diagonal 3x3 matrix $\boldsymbol{K_{pi}}$ (3-2).

Negative stiffness values in (3-7) are considered to be added to the horizontal springs k_{pi} and k_{qi}.

Looking at Figure 3-2, we can transform the displacements along the spring axes $\boldsymbol{p_i} = \{p_i\ \ q_i\ \ r_i\}_i^T$ into the displacements along the body axes $\boldsymbol{x_i} = \{x_i\ y_i\ z_i\}_i^T$:

$$R_{\phi i}\{p_i \quad q_i \quad r_i\}^T = \{x_i \quad y_i \quad z_i\}^T \tag{3-8}$$

by using the rotation matrix $R_{\phi i}$:

$$R_{\phi i} = \begin{bmatrix} \cos\phi_i & \sin\phi_i & 0 \\ -\sin\phi_i & \cos\phi_i & 0 \\ 0 & 0 & 1 \end{bmatrix} \tag{3-9}$$

The rotation matrix $R_{\phi i}$ also transforms the forces along p_i, q_i, r_i into forces along x_i, y_i, z_i respectively. Hence, using $R_{\phi i}$ we can add the effects of pre-stress forces (3-6) into the stiffness matrix to be obtained.

If setting up the equations of motion around the CoG then we can still use the principle axis, where the mass matrix is:

$$\begin{bmatrix} \mathbf{m} & 0 \\ 0 & J \end{bmatrix} \tag{3-10}$$

with $\mathbf{J}$ is full matrix. Moreover, the body is assumed to have a certain symmetry, thus off-diagonal terms of the inertia tensor are zero.

Accordingly, the equations of motion can be written in terms of mass and stiffness matrices as [3]:

$$\left[\begin{array}{ccc|ccc} m & 0 & 0 & 0 & 0 & 0 \\ 0 & m & 0 & 0 & 0 & 0 \\ 0 & 0 & m & 0 & 0 & 0 \\ \hline 0 & 0 & 0 & J_{xx} & 0 & 0 \\ 0 & 0 & 0 & 0 & J_{yy} & 0 \\ 0 & 0 & 0 & 0 & 0 & J_{zz} \end{array}\right] \begin{Bmatrix} \ddot{x} \\ \ddot{y} \\ \ddot{z} \\ \ddot{\alpha} \\ \ddot{\beta} \\ \ddot{\gamma} \end{Bmatrix} + \left[\begin{array}{ccc|ccc} k_{xx} & k_{xy} & k_{xz} & k_{x\alpha} & k_{x\beta} & k_{x\gamma} \\ k_{yx} & k_{yy} & k_{yz} & k_{y\alpha} & k_{y\beta} & k_{y\gamma} \\ k_{zx} & k_{zy} & k_{zz} & k_{z\alpha} & k_{z\beta} & k_{z\gamma} \\ \hline k_{\alpha x} & k_{\alpha y} & k_{\alpha z} & k_{\alpha\alpha} & k_{\alpha\beta} & k_{\alpha\gamma} \\ k_{\beta x} & k_{\beta y} & k_{\beta z} & k_{\beta\alpha} & k_{\beta\beta} & k_{\beta\gamma} \\ k_{\gamma x} & k_{\gamma y} & k_{\gamma z} & k_{\gamma\alpha} & k_{\gamma\beta} & k_{\gamma\gamma} \end{array}\right] \begin{Bmatrix} x \\ y \\ z \\ \alpha \\ \beta \\ \gamma \end{Bmatrix} = 0 \tag{3-11}$$

or with 3x3 block matrices:

$$\left[\begin{array}{c|c} \boldsymbol{m} & 0 \\ \hline 0 & \boldsymbol{J} \end{array}\right] \begin{Bmatrix} \ddot{\boldsymbol{x}} \\ \ddot{\boldsymbol{\alpha}} \end{Bmatrix} + \left[\begin{array}{c|c} \boldsymbol{K_{xx}} & \boldsymbol{K_{x\alpha}} \\ \hline \boldsymbol{K_{\alpha x}} & \boldsymbol{K_{\alpha\alpha}} \end{array}\right] \begin{Bmatrix} \boldsymbol{x} \\ \boldsymbol{\alpha} \end{Bmatrix} = 0 \tag{3-12}$$

where

$$\begin{aligned} \boldsymbol{K_{xx}} &= \sum_{i=1}^{4} \boldsymbol{K_{xi}} \\ \boldsymbol{K_{x\alpha}} &= \sum_{i=1}^{4} \boldsymbol{K_{xi}} R_{0i}^T = \boldsymbol{K_{\alpha x}^T} \\ \boldsymbol{K_{\alpha\alpha}} &= \sum_{i=1}^{4} R_{0i} \boldsymbol{K_{xi}} R_{0i}^T + diag\{-mgh_1,\ -mgh_1,\ 0\} \\ \boldsymbol{K_{xi}} &= R_{\phi i} K_{pi} R_{\phi i}^T \\ R_{0i} &= \begin{pmatrix} 0 & -r_{0z} & r_{0y} \\ r_{0z} & 0 & -r_{0x} \\ -r_{0y} & r_{0x} & 0 \end{pmatrix}_i \end{aligned} \tag{3-13}$$

Note that $diag\{-mgh_1,\ -mgh_1,\ 0\}$ term comes from the pre-stress forces at the vertical springs. It is not included in the original algorithm, since [3] considers the unloaded configuration.

3-2-1 Obtaining the State Space Model

Similar as done for the springs, we can also include damping of the isolators $\{c_{pi}\ c_{qi}\ c_{ri}\}$. Damping matrix D can be found using the same algorithm (3-13). Notice that, for damping, the extra term $diag\{-mgh_1,\ -mgh_1,\ 0\}$ should not be included in the equations. Consequently, equations of motion for CoG of the supported body under gravitational field can be written as:

$$M\ddot{q} + D\dot{q} + Kq = 0 \tag{3-14}$$

where M, D and K are the mass, damping and stiffness matrices and have dimensions $M, D, K \in \mathbb{R}^{6x6}$ respectively. Moreover, $q = \{x\ y\ z\ \alpha\ \beta\ \gamma\}^T \in \mathbb{R}^{6x1}$ describes the position of CoG with respect to the fixed reference frame.

We define inputs and outputs for the system (3-14) as follows: 12 inputs are defined as the forces acting along the local axis of each isolator, $\{f_{pi}\ f_{qi}\ f_{ri}\}^T$. Furthermore, velocity of the CoG is assumed to be available as output. Accordingly, state space equations become:

$$\begin{aligned} \dot{\mathbf{x}} &= \mathbf{Ax} + \mathbf{Bu} \\ \mathbf{y} &= \mathbf{Cx} + \mathbf{Du} \end{aligned} \tag{3-15}$$

or in terms of block matrices:

$$\dot{\mathbf{x}}_{12x1} = \left[\begin{array}{c|c} 0_{6x6} & I_{6x6} \\ \hline -M^{-1}K & -M^{-1}D \end{array}\right] \left\{\begin{array}{c} q \\ \hline \dot{q} \end{array}\right\} + \left[\begin{array}{c} 0_{6x12} \\ \hline B_2 \end{array}\right] \mathbf{u}$$

$$\mathbf{y}_{6x1} = \left[\begin{array}{c|c} 0_{6x6} & I_{6x6} \end{array}\right] \left\{\begin{array}{c} q \\ \hline \dot{q} \end{array}\right\} \tag{3-16}$$

where B_2 can be found as:

$$B_2 = \left[\begin{array}{cccc} M^{-1}B^{(1)} & M^{-1}B^{(2)} & M^{-1}B^{(3)} & M^{-1}B^{(4)} \end{array}\right]_{6x12} \tag{3-17}$$

being the input vector of isolator i, $B^{(i)}$ can be calculated as:

$$B^{(i)} = \left[\begin{array}{c} R_{\phi i} \\ R_{0i}R_{\phi i} \end{array}\right]_{6x3} \tag{3-18}$$

where $R_{\phi i}$ and R_{0i} are given in (3-9) and (3-13) respectively.

For the rest of the thesis, **G** represents the state space model (3-15) of Passive Vibration Isolation System (PVIS), where the inputs are 12 forces acting along the local axis of 4 isolators, and the outputs are velocities of the CoG.

3-2-2 Effect of Gravity on the Natural Frequencies

As we discussed in the previous chapter, the gravity changes the horizontal dynamics due to the negative stiffness caused by inverse pendulum configuration, which is captured by $-mg/L$ term shown in (3-7). Moreover, the pre-stress force due to gravity changes the rotational dynamics which can be seen from the $-mgh_1$ term in (3-13). In order to see the effect of gravity clearly, we calculate the 6 natural frequencies of the system for two cases, where in the first case the gravity is set to zero ($g = 0mm/s^2$) and in the second case it is included in our model ($g = 9810mm/s^2$). The length of the vertical springs are L = 113.5mm and the vertical distance of the isolators to CoG is h_1 = 210mm. The result is shown in Table 3-1. Consequently, there is an important difference between the two cases, where the natural frequencies of the system change more than 20%.

Table 3-1: Natural Frequencies of the System

	Natural Frequencies [Hz]					
g=$0mm/s^2$	0.8621	0.9199	1.0184	1.8704	1.8937	2.3993
g=$9810mm/s^2$	0.6471	0.7006	0.9199	0.9913	1.0953	1.1558

3-2-3 Discussion

In the previous section we had introduced a few constraints on several parameters. In this section, we provided an algorithm in order to obtain the stiffness matrix of a supported 3D body according to these assumptions. The introduced matrix method to find the parametric 6x6 stiffness matrix is based on transforming the stiffness and damping of each isolator from their local axis into the coordinate axis attached at the CoG. The effect of isolators are added together to find the overall stiffness matrix, where the gravity and length of the springs are included in the linear equations.

Using parametric mass, stiffness and damping matrices, state space equations of the system are calculated. Since all the parameters have physical meaning, the state space model (3-16) can be used to compare different configurations of the system and their effects on the overall dynamic performance. In other words, we can analyze effects of mass (m); inertia tensor (J); location of the isolators (h_1, d, w_1, w_2); rotation of the isolators around their vertical axis (ϕ); horizontal (k_{pi}, k_{qi}) and vertical (k_{zL}, k_{zR}) stiffness values; length of the vertical springs (L) and gravity (g).

3-3 Transmissibility

Figure 3-5 illustrates the transmissibility and compliance of isolator i with 1 DOF.

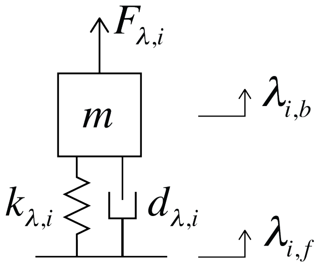

Figure 3-5: Transmissibility and Compliance in SDOF

The equations of motion can be written as:

$$m\ddot{\lambda}_{i,b} = F_{\lambda,i} + k_{\lambda,i}(\lambda_{i,f} - \lambda_{i,b}) + d_{\lambda,i}(\dot{\lambda}_{i,f} - \dot{\lambda}_{i,b}) \tag{3-19}$$

where $\lambda_{i,b}$ and $\lambda_{i,f}$ represent the displacements of the body and floor along any of the local axis p_i, q_i, r_i of isolator i. Moreover, $F_{\lambda,i}$, $k_{\lambda,i}$, $d_{\lambda,i}$ represent the force, stiffness and damping along the local axis of isolator i. By manipulating these equations we can calculate the transfer function from floor velocity $\dot{\lambda}_{i,f}$ and force $F_{\lambda,i}$ to body velocity $\dot{\lambda}_{i,b}$ as:

$$T_{\lambda,i} = \frac{\dot{\lambda}_{i,b}}{\dot{\lambda}_{i,f}} = \frac{d_{\lambda,i}s + k_{\lambda,i}}{ms^2 + d_{\lambda,i}s + k_{\lambda,i}} \tag{3-20}$$

$$\dot{Q}_{\lambda,i} = \frac{\dot{\lambda}_{i,b}}{F_{\lambda,i}} = \frac{s}{ms^2 + d_{\lambda,i}s + k_{\lambda,i}} \tag{3-21}$$

Moreover, we provide the 3D model in Figure 3-6, where the connection points between isolator i and floor (P_i'); and the connection points between isolator i and the body (P_i) are shown.

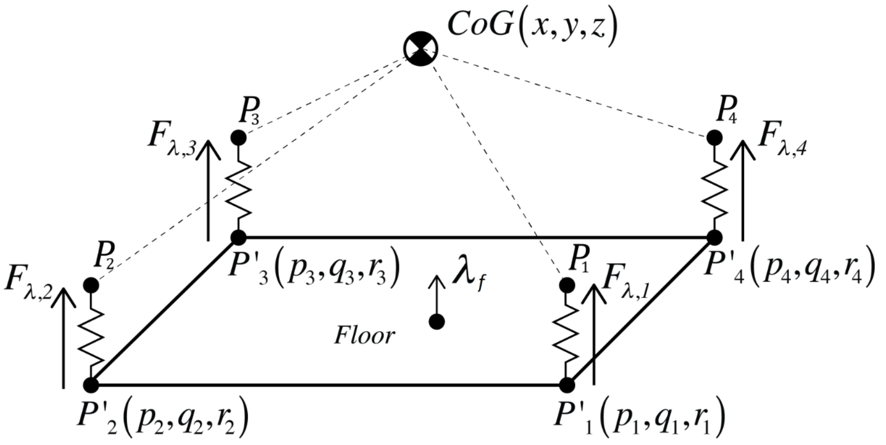

Figure 3-6: Connection Points

One end of the isolator i is attached to the floor at point P_i', the other end is attached to the body at point P_i. Vibrations at the surrounding are transmitted to POB through the floor.

Magnitudes of the floor oscillations along the local axes are depicted with x_f, y_f, z_f. Notice that, floor is modelled as a massive rigid body which can oscillate in horizontal and vertical directions. Hence, the displacement of the point P_i' along any of the local axis is the same for each isolator. For example, the magnitude of the floor motion in r_i is the same for each P_i' and equal to z_f etc. The rotations of the floor are neglected. Furthermore x_f, y_f, z_f are assumed to be generated by independent stochastic processes.

Floor motion leads to forces on the payload, that can be easily derived as:

$$Z_{\lambda,i} = \frac{F_{\lambda,i}}{\dot{\lambda}_{i,f}} = \frac{d_{\lambda,i}s + k_{\lambda,i}}{s} \tag{3-22}$$

Hence in order to include the floor motion as a disturbance to the model, we have:

$$Z_i = \begin{bmatrix} \frac{F_{p,i}}{\dot{x}_f} & 0 & 0 \\ 0 & \frac{F_{q,i}}{\dot{y}_f} & 0 \\ 0 & 0 & \frac{F_{r,i}}{\dot{z}_f} \end{bmatrix}_{3x3} \tag{3-23}$$

The transfer function from 3x1 floor velocities to 12x1 isolator forces can be written as:

$$\mathbf{G_d} = \begin{bmatrix} Z_1 \\ Z_2 \\ Z_3 \\ Z_4 \end{bmatrix}_{12x3} \tag{3-24}$$

Consequently, transmissibility for passive vibration isolation system can be calculated by a series connection of the transfer function from floor velocity to isolator forces ($\mathbf{G_d}$) and the transfer function from isolator forces to CoG velocity ($\mathbf{G}$):

$$\mathbf{T_P} = \begin{bmatrix} \mathbf{G G_d} \end{bmatrix}_{6x3} \tag{3-25}$$

Since we have assumed the floor is very large and rigid, then rotations must be small enough and this leads to correlation 1 of the 4 isolators. If correlations between x_1, x_2, x_3, x_4 are certainly not close to 1, one might extend the model by rotations or keep rotations zero and introduce 12 independent sources for floor vibration.

Notice that $\mathbf{T_P}$ is a multidimensional transmissibility function depending on physical parameters. Hence, we can investigate the effects of different parameters and coupling between different DOFs on the transmissibility curve to analyze the performance of vibration isolation system.

3-4 Active Components

3-4-1 Controller

In the first chapter, we mentioned the skyhook damping as a control strategy to dampen out the motion at natural frequencies. Skyhook damping is based on absolute velocity feedback. Hence in Figure 3-5, the actuator force along the local axis is:

$$F_{\lambda,i} = -k_{vi} * \dot{\lambda}_{i,b} \tag{3-26}$$

where $F_{\lambda,i}$ represents the actuator force of isolator i and k_{vi} is the negative feedback gain. Thus, putting (3-26) into the equations of motion in (3-19), we obtain:

$$m\ddot{\lambda}_{i,b} = -k_v\dot{\lambda}_{i,b} + k_{\lambda,i}(\lambda_{i,f} - \lambda_{i,b}) + d_{\lambda,i}(\dot{\lambda}_{i,f} - \dot{\lambda}_{i,b}) \tag{3-27}$$

By manipulating (3-27) we can calculate the closed loop transfer function from floor velocity to body velocity in local axis as:

$$T_{CL,\lambda,i} = \frac{\dot{\lambda}_{i,b}}{\dot{\lambda}_{i,f}} = \frac{d_{\lambda,i}s + k_{\lambda,i}}{ms^2 + (d_{\lambda,i} + k_{vi})s + k_{\lambda,i}} \tag{3-28}$$

Notice that, if we keep the damping $d_{\lambda,i}$ very small, we can obtain a $-40dB$ roll-off after the natural frequency, where the feedback gain k_{vi} suppresses the peak at the natural frequency.

This benefit of skyhook control is used in many vibration isolation systems to obtain an optimum transmissibility curve. Therefore, $d_{\lambda,i}$ are designed such that damping of each rigid body mode of POB is very small.

As a result of the absolute velocity feedback, the body becomes as if it is hooked to the sky with a damper, hence the name skyhook damping. Figure 3-7 illustrates this effect.

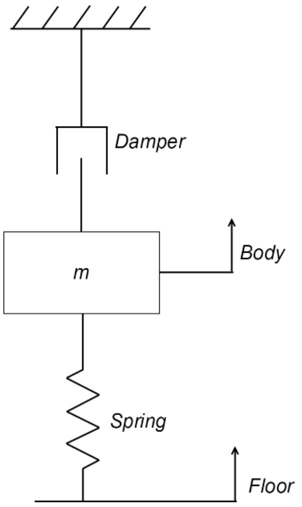

Figure 3-7: Illustration of Skyhook Damping

3-4-2 Sensors and Actuators

Sensors

In order to measure the absolute velocity, geophones are used. Figure 3-8 explains the working principle of a geophone. The cage is attached to the body, whose absolute velocity is to be measured. The absolute velocity can be measured along the cylindrical axis of the geophone (coil).

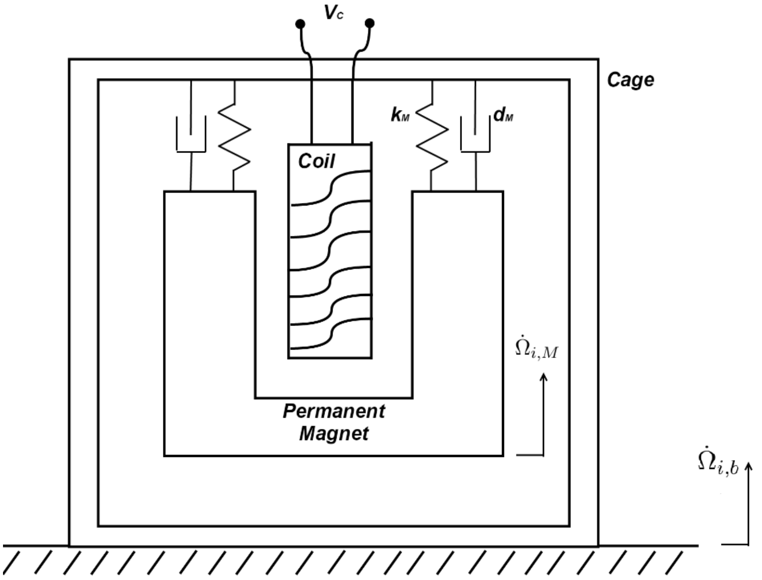

Figure 3-8: Main Parts Inside a Geophone

In AVIS, geophones are fixed to the points of action P_i and part of the isolator. We assume the cylindrical axis of geophone is aligned with any of x_i, y_i and z_i. Remember that, x_i, y_i, z_i are the axes at P_i that are aligned with the coordinate axes at CoG x, y, z. Hence, geophones measure the absolute velocity of P_i along any of the coordinate axes $\Omega_{i,b}$ $(x,\, y,\, z)$.

The voltage of the coil V_c is proportional to the change of the magnetic flux with respect to time. Moreover, change of flux is also proportional to relative displacement of the magnet with respect to coil: $\Omega_{i,M} - \Omega_{i,b}$. Therefore, the voltage V_c is directly proportional to the relative velocity $\dot{\Omega}_{i,M} - \dot{\Omega}_{i,b}$.

We can write the equations of motion for the magnet as:

$$m_M \ddot{\Omega}_{i,M} = d_M(\dot{\Omega}_{i,b} - \dot{\Omega}_{i,M}) + k_M(\Omega_{i,b} - \Omega_{i,M}) \tag{3-29}$$

where m_M, k_M and d_M are the mass, stiffness and damping of the magnet respectively. Moreover, $\dot{\Omega}_{i,M}$ and $\dot{\Omega}_{i,b}$ represent the absolute velocities of the magnet and P_i -or coil- in any of the axes x, y, z. Adding $-m_M\ddot{\Omega}_{i,b}$ to both sides and manipulating the equations we get:

$$m_M(\ddot{\Omega}_{i,M} - \ddot{\Omega}_{i,b}) + d_M(\dot{\Omega}_{i,M} - \dot{\Omega}_{i,b}) + k_M(\Omega_{i,M} - \Omega_{i,b}) = -m_M\ddot{\Omega}_{i,b} \tag{3-30}$$

If we take the Laplace Transform of (3-30) we can obtain the transfer function from absolute velocity $\dot{\Omega}_{i,b}$ to relative velocity $\dot{\Omega}_{i,M} - \dot{\Omega}_{i,b}$ as:

$$\frac{V_c}{\dot{\Omega}_{i,b}} : \quad \frac{\Omega(s)_{i,M} - \Omega(s)_{i,b}}{\Omega_{i,b}(s)} = \frac{-s^2 m_M}{s^2 m_M + s d_M + k_M} \tag{3-31}$$

In Figure (3-9) sensitivity of a geophone ($V_c/\dot{\Omega}_{i,b}$), which is taken from a producer [21] is shown.

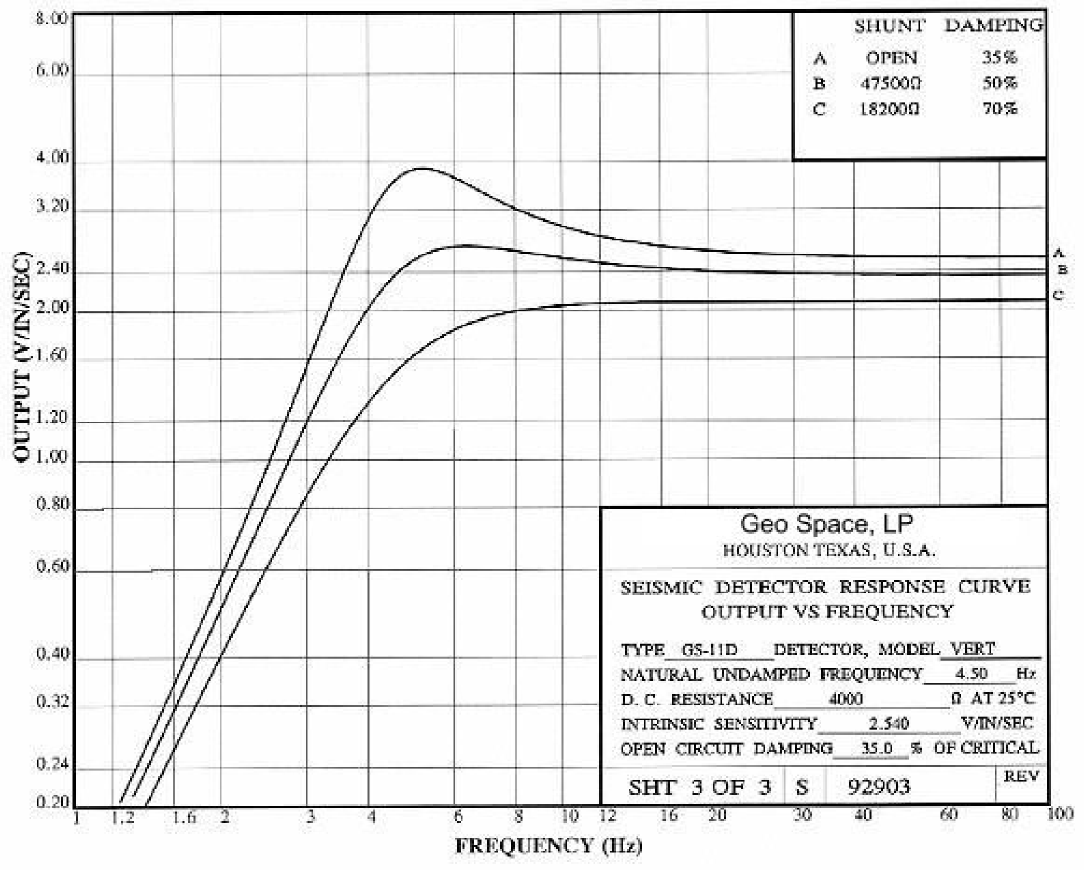

Figure 3-9: Sensitivity of the Geophone GS-11D [4]

Natural frequency of a geophone is around 4.5Hz. That means, the geophone can only accurately measure the velocities at the frequencies higher than 4.5Hz. However, the rigid body modes of the AVIS lie between 0.5Hz - 1.5Hz. Therefore, in order to estimate the velocities at lower frequencies, geophones are combined with digital stretcher filters, where the stretcher filters have inverse dynamic characteristics of the geophone. Hence, the total transfer function becomes a constant. This is illustrated in Figure 3-10.

On the other hand, amplifying low frequency signals of the geophone results in amplification of the noise at lower frequencies. Hence, geophones with lower natural frequencies should be preferred for high precision applications. Nevertheless, to keep the formulation simple, we will neglect the internal dynamics of the geophone (k_M, d_M) and assume that the coil voltage is directly proportional to the absolute velocity of P_i.

Moreover, rotational movement of the POB cause rotation of the geophone itself, which then changes the magnetic flux inside the coil. This results in an unwanted parasitic voltage that disturbs the accuracy of the measurement. For simplicity, we will not consider this parasitic effect. However, it should be underlined that, for a more accurate model, internal dynamics of the sensor and the parasitic effect should be included, which is left as a future work. For this thesis, transfer function between absolute velocity of P_i and controller K_v is considered to be one.

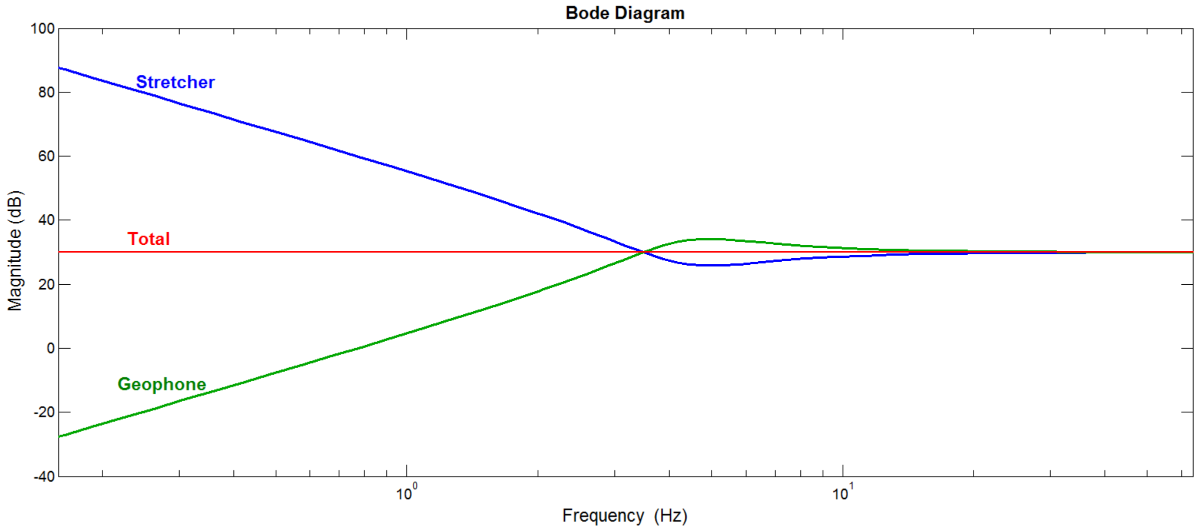

Figure 3-10: Bode Magnitude Diagram for Velocity Measurement

Actuators

Actuators will not be discussed in detail. We assume transfer function from controller to actuator force is equal to one.

3-5 AVIS

The goal of the thesis is to build a framework for analyzing the performance of the active vibration isolation system in terms of transmissibility and sensor sensitivity. To develop such a framework, we need to obtain the closed loop model of the AVIS for a certain configuration as can be seen in practice. The AVIS that we will analyze has 4 isolators where the orthogonal local axes of each isolator p_i, q_i, r_i coincide with the coordinate axes x, y and z respectively ($\phi = 0$).

In theory, 6 actuators and 6 sensors should be enough to control the 6 DOF. However, the AVIS that we consider has 8 actuators and 7 sensors connected to four isolators at points P_i. Actuators apply force and sensors measure the velocity at P_i. Numbers and directions of actuators and sensors at each isolator can be seen in Figure 3-11. Note that, the direction of the z axis is out of the paper.

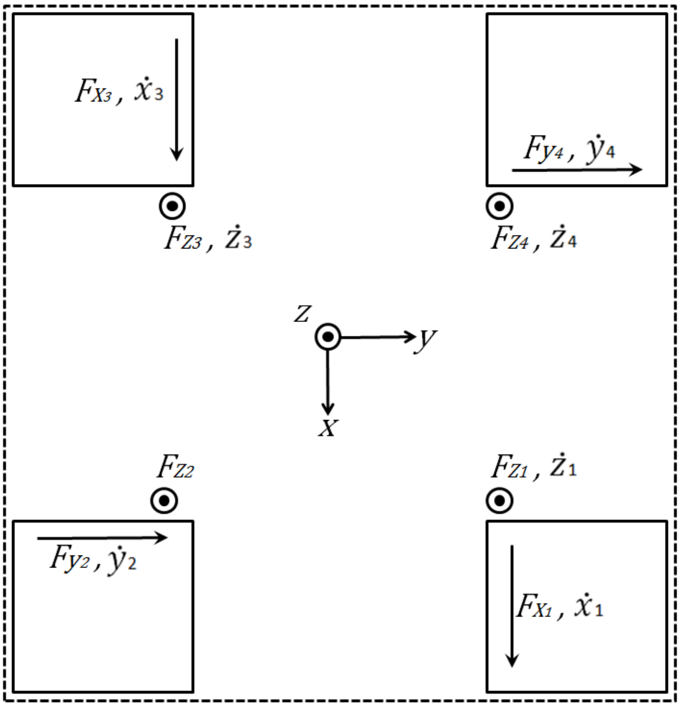

Figure 3-11: Top View of the Isolation System

For a clear view of the system, the linear fractional representation with generalized plant $\mathbf{P}$ and multidimensional controller $\mathbf{K_v}$ in positive feedback interconnection is illustrated in Figure 3-12:

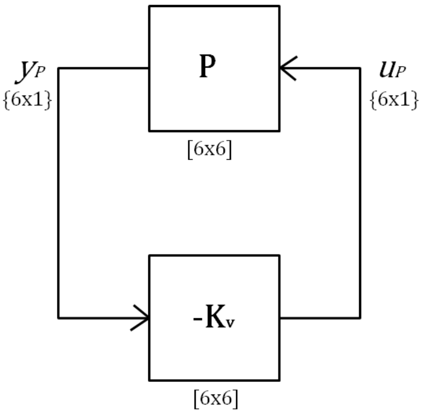

Figure 3-12: Linear Fractional Representation of AVIS

where $[n_y \text{ x } n_u]$ shows the size of the transfer functions in which n_u is the number of inputs and n_y is the number of outputs. u_P and y_P are control signals and output signals respectively with a size of $\{6x1\}$. Next, we will explain the controller $\mathbf{K_v}$ and the generalized plant $\mathbf{P}$.

3-5-1 Controller K$_v$

In order not to confuse the controller with the stiffness matrix and underline that we have absolute velocity feedback, the controller is denoted with underscore $\mathbf{K_v}$.

The diagonal controller of the AVIS is modelled as skyhook control:

$$\mathbf{K_v} = \begin{bmatrix} k_{v1} & 0 & 0 & 0 & 0 & 0 \\ 0 & k_{v2} & 0 & 0 & 0 & 0 \\ 0 & 0 & k_{v3} & 0 & 0 & 0 \\ 0 & 0 & 0 & k_{v4} & 0 & 0 \\ 0 & 0 & 0 & 0 & k_{v5} & 0 \\ 0 & 0 & 0 & 0 & 0 & k_{v6} \end{bmatrix} \tag{3-32}$$

The controller $\mathbf{K_v}$ controls the velocity in so called 'logical axis', which are defined as:

$$\begin{aligned} x_L &= 0.5 * (x_1 + x_3) \\ y_L &= 0.5 * (y_2 + y_4) \\ z_L &= 0.5 * (z_1 + z_3) \\ \alpha_L &= 0.5 * (z_4 - z_3) \\ \beta_L &= 0.5 * (z_4 - z_1) \\ \gamma_L &= 0.5 * (x_3 - x_1) \end{aligned} \tag{3-33}$$

Therefore, k_{vj} represents the feedback gain for the corresponding logical axis. Moreover, notice that since the logical axis α_L, β_L and γ_L are obtained from the translational motions of P_i, they are scaled versions of the rotations along the CoG.

3-5-2 Generalized Plant

The AVIS in Figure 3-11 is modelled with the controller $\mathbf{K_v}$ and the generalized plant $\mathbf{P}$, which is shown in Figure 3-13.

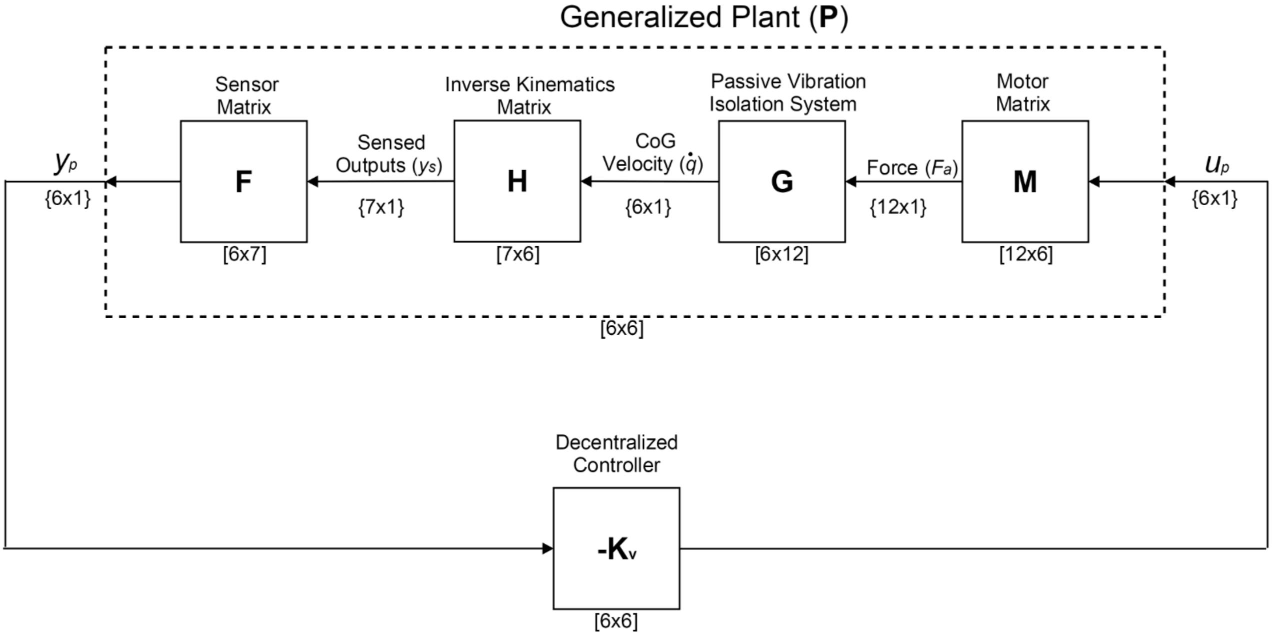

Figure 3-13: Block Matrices Inside the Generalized Plant

Each block represents the transfer function from its input to the output. For example, $\mathbf{G}$, which is already explained in Section 3-2-1, is the transfer function from 12 actuator forces (F_a) in local axis to 6 CoG velocities $(\dot{q})$ in body axis etc.

Transformation between logical axes of the controller and body axes are done using sensor matrix $\mathbf{F}$ and motor matrix $\mathbf{M}$, which depend on the directions of the geophones and actuator forces. Moreover, since the velocity of the CoG, as we have modelled in our model (3-16), is not available as output, an additional transformation matrix $\mathbf{H}$ is needed for our analysis purposes in order to calculate the velocities of P_i as they are measured in practice. Next, we will explain the blocks $\mathbf{F}$, $\mathbf{M}$ and $\mathbf{H}$.

Sensor Matrix (F)

Sensor matrix transforms 7 available velocities of points of action $\dot{x}_1$, $\dot{z}_1$, $\dot{y}_2$, $\dot{x}_3$, $\dot{z}_3$, $\dot{y}_4$, $\dot{z}_4$ into 6 velocities in the logical axes $\dot{x}_L$, $\dot{y}_L$, $\dot{z}_L$, $\dot{\alpha}_L$, $\dot{\beta}_L$, $\dot{\gamma}_L$:

$$\begin{aligned}
\dot{x}_L &= 0.5 * (\dot{x}_1 + \dot{x}_3) \\
\dot{y}_L &= 0.5 * (\dot{y}_2 + \dot{y}_4) \\
\dot{z}_L &= 0.5 * (\dot{z}_1 + \dot{z}_3) \\
\dot{\alpha}_L &= 0.5 * (\dot{z}_4 - \dot{z}_3) \\
\dot{\beta}_L &= 0.5 * (\dot{z}_4 - \dot{z}_1) \\
\dot{\gamma}_L &= 0.5 * (\dot{x}_3 - \dot{x}_1)
\end{aligned} \tag{3-34}$$

From (3-34), we can obtain the sensor matrix **F**:

$$\mathbf{F} = \begin{bmatrix} 0.5 & 0 & 0 & 0.5 & 0 & 0 & 0 \\ 0 & 0 & 0.5 & 0 & 0 & 0.5 & 0 \\ 0 & 0.5 & 0 & 0 & 0.5 & 0 & 0 \\ 0 & 0 & 0 & 0 & -0.5 & 0 & 0.5 \\ 0 & -0.5 & 0 & 0 & 0 & 0 & 0.5 \\ -0.5 & 0 & 0 & 0.5 & 0 & 0 & 0 \end{bmatrix}_{6x7} \tag{3-35}$$

Motor Matrix (M)

The velocities in logical axes are controlled by the controller using actuator forces. For our system, 8 actuator forces F_{x_1}, F_{z_1}, F_{y_2}, F_{z_2}, F_{x_3}, F_{z_3}, F_{y_4}, F_{z_4} control 6 logical axes. As we find it in practical vibration isolation systems, the motor matrix **M** is suggested to be:

$$\mathbf{M} \quad = \begin{array}{c} \begin{array}{cccccc} U_{x_L} & U_{y_L} & U_{z_L} & U_{\alpha_L} & U_{\beta_L} & U_{\gamma_L} \end{array} \\ \begin{bmatrix} 0.5 & 0 & 0 & 0 & 0 & -0.5 \\ 0 & 0 & 0 & 0 & 0 & 0 \\ 0 & 0 & 0.25 & 0.25 & -0.25 & 0 \\ 0 & 0 & 0 & 0 & 0 & 0 \\ 0 & 0.5 & 0 & 0 & 0 & 0 \\ 0 & 0 & 0.25 & -0.25 & -0.25 & 0 \\ 0.5 & 0 & 0 & 0 & 0 & 0.5 \\ 0 & 0 & 0 & 0 & 0 & 0 \\ 0 & 0 & 0.25 & -0.25 & 0.25 & 0 \\ 0 & 0 & 0 & 0 & 0 & 0 \\ 0 & 0.5 & 0 & 0 & 0 & 0 \\ 0 & 0 & 0.25 & 0.25 & 0.25 & 0 \end{bmatrix}_{12x6} \end{array} \tag{3-36}$$

Notice that, the input of our model is defined as 12x1 vector which are the forces along the local axes of 4 isolators. On the other hand, since there are only 8 actuators in our system, corresponding four rows of the motor matrix in (3-36) are zero, which represent missing 4 actuator forces F_{y_1}, F_{x_2}, F_{y_3}, F_{x_4}.

Accordingly, the resulting control forces in logical axes U_{x_L}, U_{y_L}, U_{z_L}, U_{α_L}, U_{β_L}, U_{γ_L} can be found as:

$$\begin{aligned}
U_{x_L} &= 0.5 * (F_{x_1} + F_{x_3}) \\
U_{y_L} &= 0.5 * (F_{y_2} + F_{y_4}) \\
U_{z_L} &= 0.25 * (F_{z_1} + F_{z_2} + F_{z_3} + F_{z_4}) \\
U_{\alpha_L} &= 0.25 * (F_{z_1} + F_{z_4}) - 0.25 * (F_{z_2} + F_{z_3}) \\
U_{\beta_L} &= 0.25 * (F_{z_3} + F_{z_4}) - 0.25 * (F_{z_1} + F_{z_2}) \\
U_{\gamma_L} &= 0.5 * (-F_{x_1} + F_{x_3}) \qquad (3\text{-}37)
\end{aligned}$$

In theory, the actuator inputs should also have the same ratio as arm-lengths in order to eliminate the resulting moments that occur due to non-symmetry. However, the unknown disturbances, unmodelled dynamics, as well as possible non-linearities in the isolators that are not taken into account, have a large influence on the overall performance as well, so that we rather not focus too much on this detail and neglect the different arm-lengths. Therefore, the isolators are given the same input despite the non-symmetrical geometry.

Inverse Kinematics Matrix (H)

When the model **G** was derived, we naturally arrived at having the CoG velocity and rotational velocity $\dot{x}$, $\dot{y}$, $\dot{z}$, $\dot{\alpha}$, $\dot{\beta}$, $\dot{\gamma}$. On the other hand, geophones measure the velocities of 4 points of action P_i. In order to compute the motion at P_i, we need to find the so-called inverse kinematics matrix for the rigid body that we consider. Figure 3-14 shows the CoG and the points of action P_i.

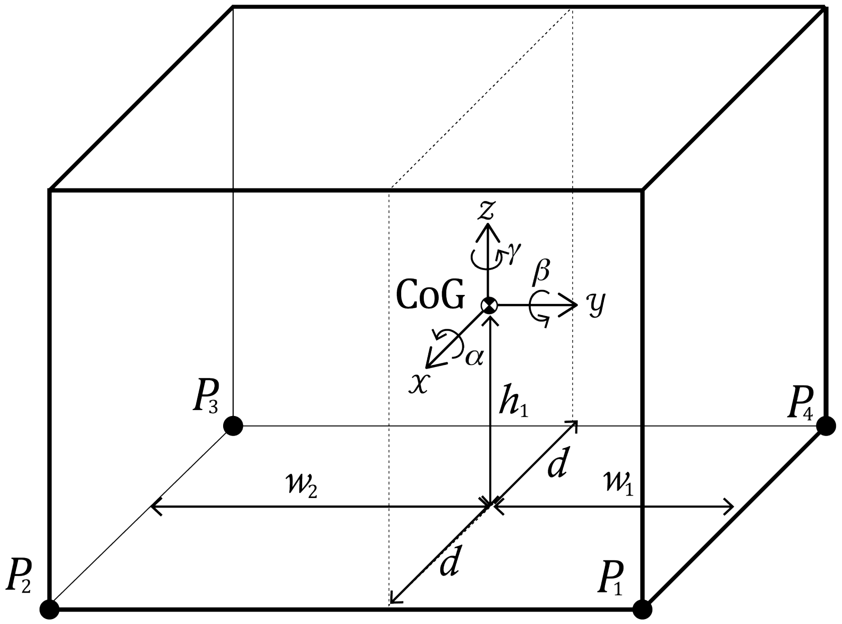

Figure 3-14: Center of Gravity and Points of Action

By looking at Figure 3-14 and using the approximation (2-20) we can relate the velocities of CoG $\dot{x}$, $\dot{y}$, $\dot{z}$, $\dot{\alpha}$, $\dot{\beta}$, $\dot{\gamma}$ with the velocities of P_i $\dot{x}_i$, $\dot{y}_i$, $\dot{z}_i$ as:

$$\begin{aligned}
\dot{x}_1 &= \dot{x} - h_1\dot{\beta} - w_1\dot{\gamma} \\
\dot{y}_1 &= \dot{y} + h_1\dot{\alpha} + d\dot{\gamma} \\
\dot{z}_1 &= \dot{z} + w_1\dot{\alpha} - d\dot{\beta} \\
\dot{x}_2 &= \dot{x} - h_1\dot{\beta} + w_2\dot{\gamma} \\
\dot{y}_2 &= \dot{y} + h_1\dot{\alpha} + d\dot{\gamma} \\
\dot{z}_2 &= \dot{z} - w_2\dot{\alpha} - d\dot{\beta} \\
\dot{x}_3 &= \dot{x} - h_1\dot{\beta} + w_2\dot{\gamma} \\
\dot{y}_3 &= \dot{y} + h_1\dot{\alpha} - d\dot{\gamma} \\
\dot{z}_3 &= \dot{z} - w_2\dot{\alpha} + d\dot{\beta} \\
\dot{x}_4 &= \dot{x} - h_1\dot{\beta} - w_1\dot{\gamma} \\
\dot{y}_4 &= \dot{y} + h_1\dot{\alpha} - d\dot{\gamma} \\
\dot{z}_4 &= \dot{z} + w_1\dot{\alpha} + d\dot{\beta}
\end{aligned} \tag{3-38}$$

From (3-38) we can obtain the inverse kinematics matrix H' that transforms CoG velocities $\dot{q} = \{\dot{x}\ \dot{y}\ \dot{z}\ \dot{\alpha}\ \dot{\beta}\ \dot{\gamma}\}^T$ into points of action velocities $v = \{\dot{x}_1\ \dot{y}_1\ \dot{z}_1\ \dot{x}_2\ \dot{y}_2\ \dot{z}_2\ \dot{x}_3\ \dot{y}_3\ \dot{z}_3\ \dot{x}_4\ \dot{y}_4\ \dot{z}_4\}^T$ as:

$$v = H' * \dot{q} \tag{3-39}$$

where

$$H' = \begin{bmatrix} 1 & 0 & 0 & 0 & -h_1 & -w_1 \\ 0 & 1 & 0 & h_1 & 0 & d \\ 0 & 0 & 1 & w_1 & -d & 0 \\ 1 & 0 & 0 & 0 & -h_1 & w_2 \\ 0 & 1 & 0 & h_1 & 0 & d \\ 0 & 0 & 1 & -w_2 & -d & 0 \\ 1 & 0 & 0 & 0 & -h_1 & w_2 \\ 0 & 1 & 0 & h_1 & 0 & -d \\ 0 & 0 & 1 & -w_2 & d & 0 \\ 1 & 0 & 0 & 0 & -h_1 & -w_1 \\ 0 & 1 & 0 & h_1 & 0 & -d \\ 0 & 0 & 1 & w_1 & d & 0 \end{bmatrix}_{12x6} \tag{3-40}$$

From 12 velocities that (3-40) provides, only 7 are part of the AVIS that we have modelled. Hence, we need only a subset of the rows of H', which is done by picking a matrix S'. As a result, the inverse kinematics matrix **H** for the 7 velocities of the geophones in (3-34) can be found as:

$$\mathbf{H} = S'H' \tag{3-41}$$

where

$$S' = \begin{bmatrix} 1 & 0 & 0 & 0 & 0 & 0 & 0 & 0 & 0 & 0 & 0 & 0 \\ 0 & 0 & 1 & 0 & 0 & 0 & 0 & 0 & 0 & 0 & 0 & 0 \\ 0 & 0 & 0 & 0 & 1 & 0 & 0 & 0 & 0 & 0 & 0 & 0 \\ 0 & 0 & 0 & 0 & 0 & 0 & 1 & 0 & 0 & 0 & 0 & 0 \\ 0 & 0 & 0 & 0 & 0 & 0 & 0 & 0 & 1 & 0 & 0 & 0 \\ 0 & 0 & 0 & 0 & 0 & 0 & 0 & 0 & 0 & 0 & 1 & 0 \\ 0 & 0 & 0 & 0 & 0 & 0 & 0 & 0 & 0 & 0 & 0 & 1 \end{bmatrix}_{7x12} \tag{3-42}$$

Now that we have successfully modelled our system AVIS, we continue with obtaining the transmissibility and sensor noise sensitivity transfer functions in the next section.

3-5-3 General Control Problem for Analysis of Disturbances

Figure 3-15 shows the block matrices of the overall system. **w** represents the floor vibration in terms of velocity in x, y and z directions. **n** represents the sensor noise of the 7 geophones. **z** is the performance signal we wish to analyze, which is the velocity of the CoG.

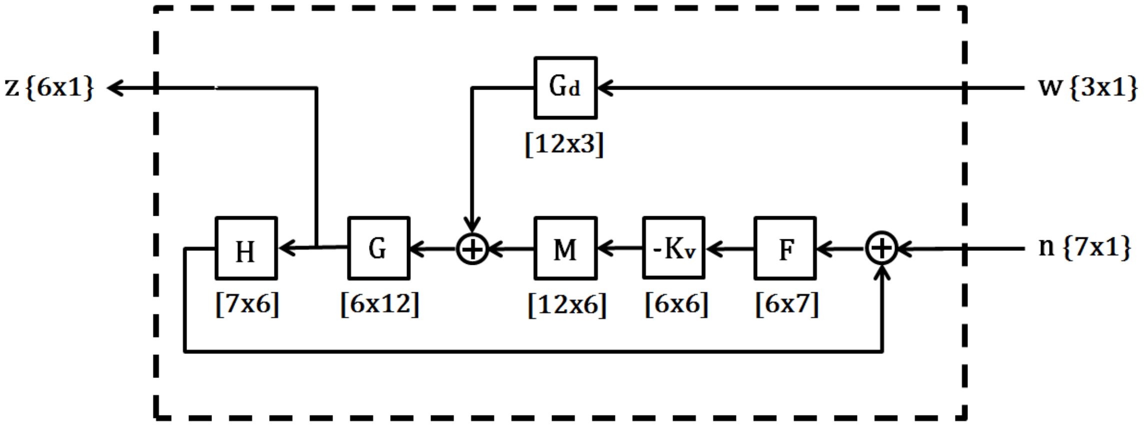

Figure 3-15: Block Matrices of the AVIS

Each of the block diagrams in Figure 3-15 are explained in the previous sections of this chapter.

As a result, using the block matrices in Figure 3-15, Multi-input Multi-output (MIMO) transfer functions from floor vibration $\mathbf{w}$ and sensor noise $\mathbf{n}$ to performance signal $\mathbf{z}$ can be found as:

$$G_{wz} = \Big[(I + \mathbf{GMK_vFH})^{-1}\mathbf{GG_d}\Big]_{6x3} \tag{3-43}$$

$$G_{nz} = \Big[(I + \mathbf{GMK_vFH})^{-1}\mathbf{GM}(-\mathbf{K_v})\mathbf{F}\Big]_{6x7} \tag{3-44}$$

where I is 6x6 identity matrix. Since both floor vibration and performance signal are defined in terms of velocity, (3-43) represents the closed loop transmissibility, (3-44) is the sensor sensitivity. These two transfer functions will be used as performance measures in order to determine the contribution of floor vibration and sensor noise to the oscillations of the POB.

As discussed before Bode magnitude diagrams are used extensively to show the performance of isolators. As our focus is not on stability issues, we are only interested in the magnitude of the vibration. Therefore, phase plots of the transfer functions are not considered. The trade-off between transmissibility and sensor noise sensitivity is shown before for SDOF systems using the Bode plot. Here, we present an example that shows this trade-off between the two performance measures for the 6 DOF MIMO model that we have obtained in this chapter.

3-5-4 Illustrative Example 1

For this example, we will use specific configuration of the system, which satisfies the constraints that we have obtained in Section 3-1. To keep the analysis simple, AVIS is assumed to be fully symmetric, where horizontal stiffness values are the same ($k_{p_i} = k_{q_i}$); horizontal distances are the same ($w_1 = w_2 = d$); local axes of the isolators are aligned with CoG axes

($\phi_i = 0$); 6 controller gains (k_{v_i}) are equal. The definition of all parameters are summarized in Figure 3-3.

In Figures 3-16 and 3-17, transmissibility functions for the translation and rotation of the CoG with different controller gains are provided while keeping all other parameters constant. Looking at the Figures 3-16 and 3-17, we see that controller gain suppresses the peaks at natural frequencies, hence improving the performance in terms of transmissibility for each performance channel (x, y, z, α, β, γ). Since the system is fully symmetric, rotation around vertical axis is decoupled and it is not influenced by the floor vibration. Notice that, vertical motion is also decoupled from the other 5 modes. On the other hand, the motion in x and y is coupled with the rotation along β and α respectively.

Sensitivity of seven geophones (S_{x1}, S_{z1}, S_{y2}, S_{x3}, S_{z3}, S_{y4}, S_{z4}) with different controller gains can be seen in Figures 3-18 and 3-19. It is clear that increasing controller gain increases the sensitivity to sensor noise, hence degrading the performance for each performance channel.

As a result, looking at the MIMO Bode diagrams, we can observe the trade-off between the two performance measures: transmissibility and sensor noise sensitivity.

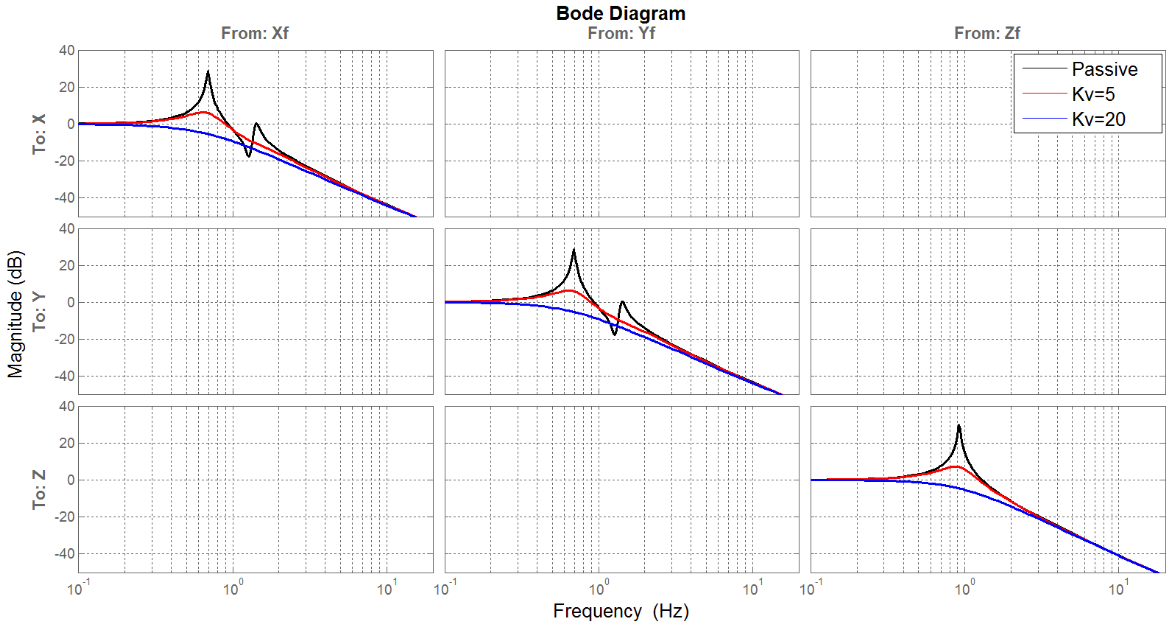

Figure 3-16: MIMO Transmissibility for CoG Translations with Different Skyhook Gains

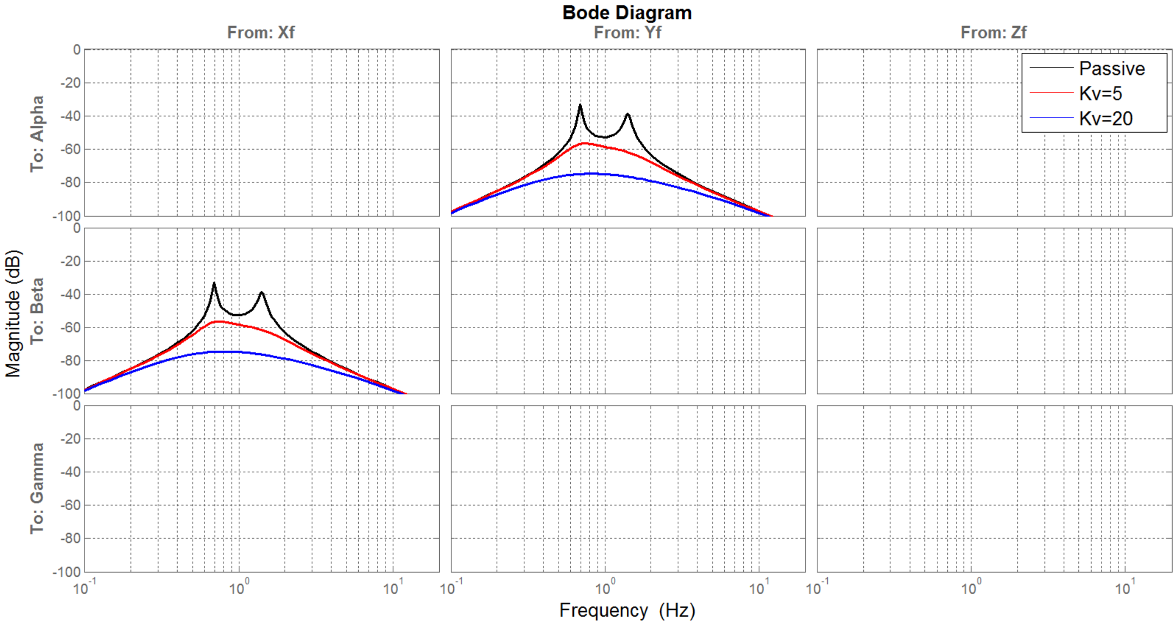

Figure 3-17: MIMO Transmissibility for CoG Rotations with Different Skyhook Gains

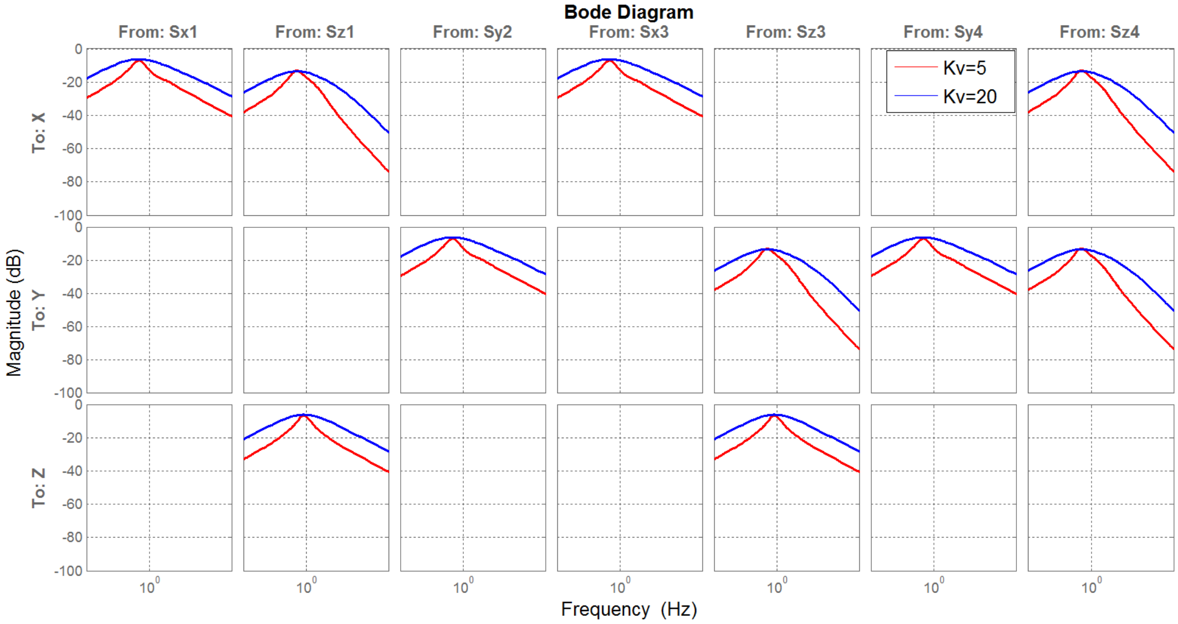

Figure 3-18: MIMO Sensor Sensitivity for CoG Translations with Different Skyhook Gains

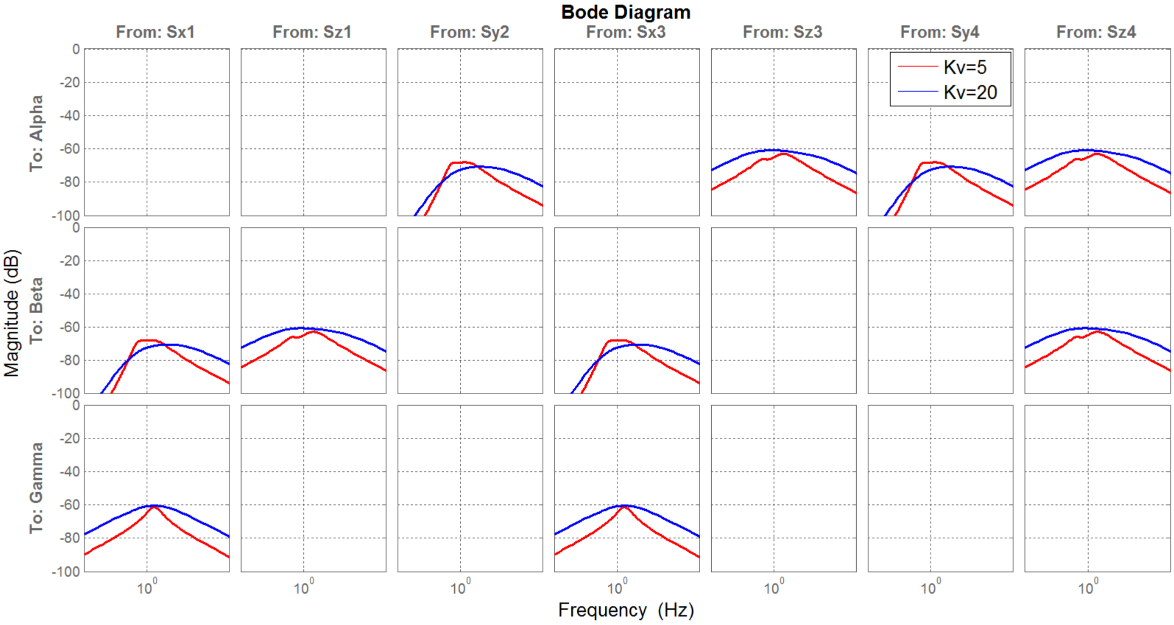

Figure 3-19: MIMO Sensor Sensitivity for CoG Rotations with Different Skyhook Gains

3-5-5 Discussion

In the previous section, we have obtained the multidimensional transmissibility function for a certain configuration of the passive vibration isolation system. In this section, we have extended the MIMO analysis to AVIS and calculated the closed loop transmissibility and sensor noise sensitivity. We can use these performance measures to analyze different configurations of the system. However, the overall performance is also affected and sometimes even determined by the level of external disturbances. Hence, the disturbances need to be included in the model for the nature of the analysis, which is the topic of the next chapter.

3-6 Summary

In this chapter, first we derived the state space model for a certain configuration of the passive vibration isolation system. Secondly, we discussed system transmissibility and constructed it for the MIMO model. Thirdly, active components of the vibration isolation system are introduced and the overall system is put into generalized plant framework to clearly show external disturbances of the system. Lastly, closed loop transmissibility and sensor noise sensitivity transfer functions are calculated for the MIMO system. This chapter concludes the modeling of AVIS. In the next chapter, we will discuss modeling of the floor vibration and sensor noise.

Chapter 4

Disturbance Modeling

In the literature, disturbances for isolation systems are divided into two categories: direct disturbance and indirect disturbance. Direct disturbances are forces caused by the equipment inside the operating machine. In photolithography applications, these can be stage motions and resulting reaction forces, air pumps, cooling equipment or acoustic noise. In case of Active Vibration Isolation System (AVIS), noise in active components like geophones, amplifiers or converters also cause direct disturbance forces on the objective device. We assume that the direct disturbances other than the sensor noise can be measured. Therefore, they are assumed be counteracted by the controller. For this thesis, we will only consider sensor noise as a direct disturbance source.

On the other hand, indirect disturbances are those that come from outside the machine. They are transmitted through the floor. Hence this type of disturbances can be modelled as floor vibration. Floor vibrations may occur due to many reasons. They can be caused by an external source outside the building like seismic motions, waves crashing on the shore, blowing wind, vehicle traffic like street, rail- or subway, construction activities nearby etc. These are mostly random vibrations and constitute a non-stationary and non-ergodic random process [22]. On the other hand, the floor vibration can also be caused by a source inside the building like foot steps of the personnel, opening and closing doors or nearby operating machines. A nice overview about how to avoid direct and indirect disturbances in high precision applications is given by [22].

The aim of the vibration isolation system is to keep the objective device standstill. On the other hand, the objective device vibrates around the equilibrium due to the collection of many disturbance sources. Therefore, to find the total level of the resulting motion, magnitudes of the disturbances in the system should be taken into account. In this chapter, we will discuss modelling of floor vibration and sensor noise in terms of their spectra.

4-1 Floor Vibration

4-1-1 Vibration Criteria Curves

In order to compare floor vibration characteristics and specify accordingly, vibration criteria have been developed. One of these vibration criteria which is widely used in the literature is called VC-curves or BBN-Curves [5].

Figure 4-2 shows all Vibration Criteria Curves (VC-curves) as they are used in practice. In addition, it shows ISO guidelines that show the relation to vibration levels in everyday life. With this family of VC-curves one can specify the type of environment needed in order our application to fulfill its task. More details and an interpretation of the VC-curves can be found in Figure 4-1, see also reference [5].

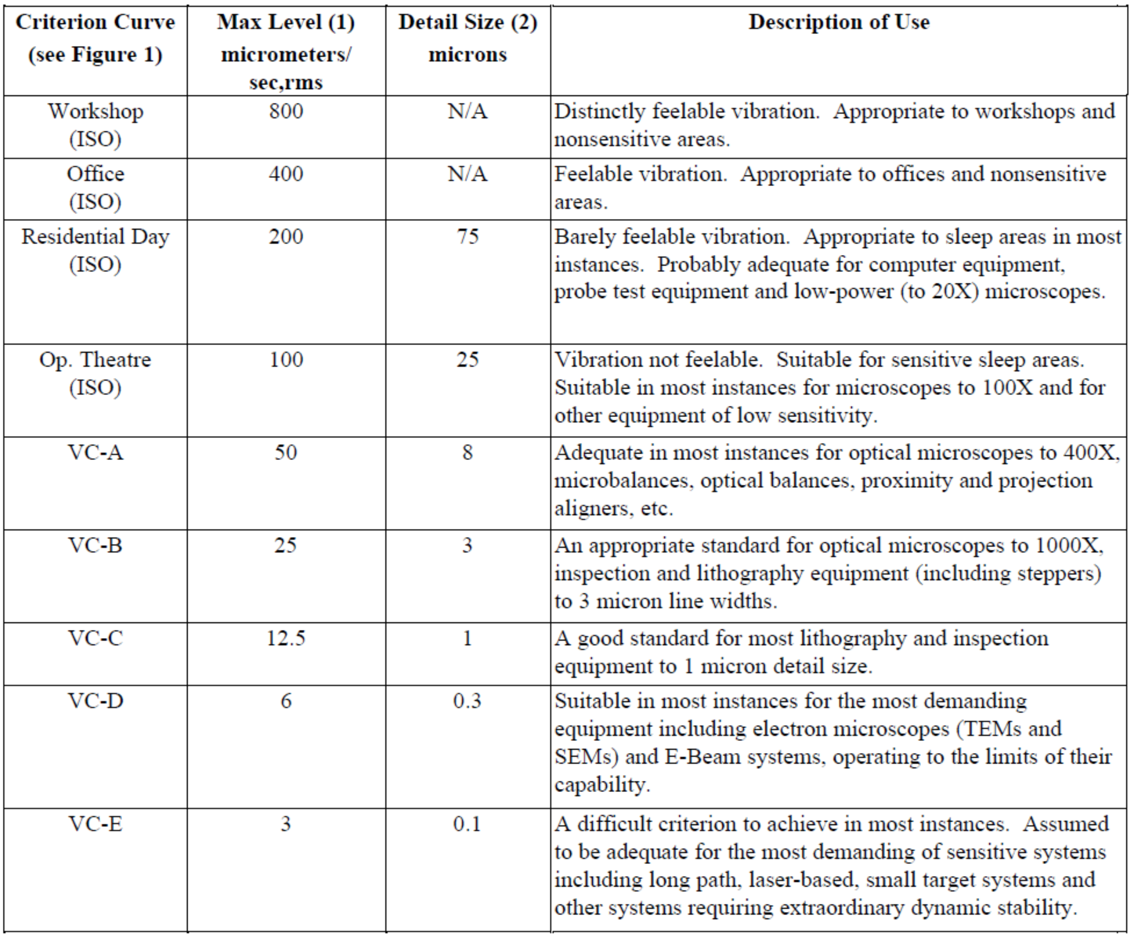

Criterion Curve (see Figure 1)	**Max Level (1) micrometers/ sec,rms**	**Detail Size (2) microns**	**Description of Use**
Workshop (ISO)	800	N/A	Distinctly feelable vibration. Appropriate to workshops and nonsensitive areas.
Office (ISO)	400	N/A	Feelable vibration. Appropriate to offices and nonsensitive areas.
Residential Day (ISO)	200	75	Barely feelable vibration. Appropriate to sleep areas in most instances. Probably adequate for computer equipment, probe test equipment and low-power (to 20X) microscopes.
Op. Theatre (ISO)	100	25	Vibration not feelable. Suitable for sensitive sleep areas. Suitable in most instances for microscopes to 100X and for other equipment of low sensitivity.
VC-A	50	8	Adequate in most instances for optical microscopes to 400X, microbalances, optical balances, proximity and projection aligners, etc.
VC-B	25	3	An appropriate standard for optical microscopes to 1000X, inspection and lithography equipment (including steppers) to 3 micron line widths.
VC-C	12.5	1	A good standard for most lithography and inspection equipment to 1 micron detail size.
VC-D	6	0.3	Suitable in most instances for the most demanding equipment including electron microscopes (TEMs and SEMs) and E-Beam systems, operating to the limits of their capability.
VC-E	3	0.1	A difficult criterion to achieve in most instances. Assumed to be adequate for the most demanding of sensitive systems including long path, laser-based, small target systems and other systems requiring extraordinary dynamic stability.

Figure 4-1: Application and Interpretation of VC-curves [5]

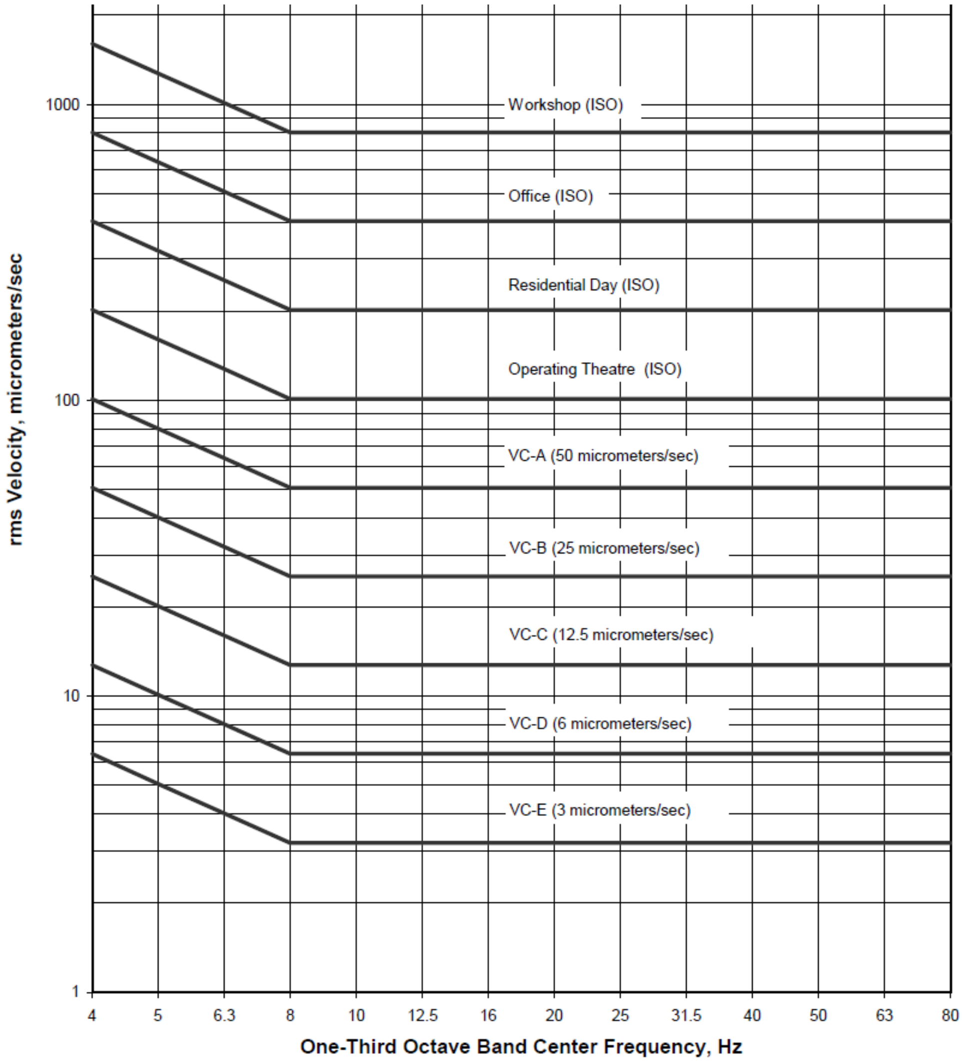

Figure 4-2: Vibration Criteria Curves [5]

Rather than using a specific floor vibration measurement, we will use VC-curves to define the level of floor vibration, which allows us to keep our analysis more general. Hence, we will use for example VC-D criteria as disturbance level and assume that manufacturer facility satisfies this criteria.

Frequency range of the VC-curves are from 4Hz to 80Hz, sometimes to 100 Hz. When they were developed, the frequencies lower than 4 Hz were out of interest. However, with the new pneumatic isolators natural frequencies of the system lie below 4 Hz. Therefore, low frequencies become important as the isolation system can amplify the floor vibration at its natural frequency. Nevertheless, a suggestion for modifying the VC-curves is provided in [22] such that the range is extended to 1 Hz and the constant velocity limit is kept. This low frequency modification is given in Figure 4-3.

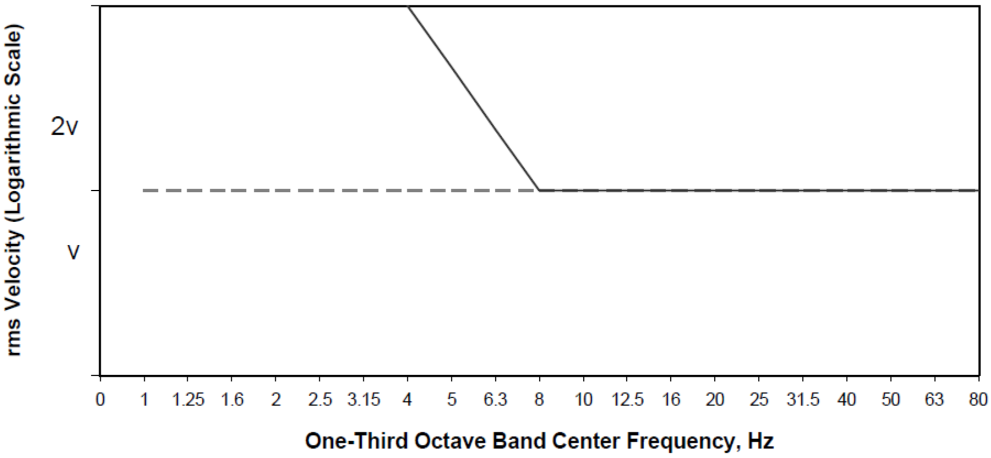

Figure 4-3: Low Frequency Modification of VC-curves [5]

For low frequency pneumatic isolation, dashed line in Figure 4-3 shows the suggested specification for a VC-Curve, where on the x-Axis are the center frequencies of one-third octave bands. The rigid body modes of our model are usually between $0.5 - 1.5$ Hz. Therefore, in our analysis, the first center frequency for the vibration criteria is decreased to 0.5 Hz. As a result, we will use the modified vibration criteria shown in Figure 4-4.

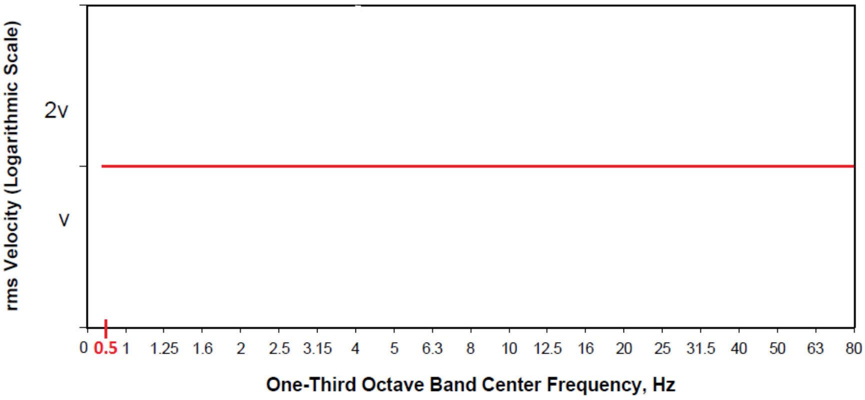

Figure 4-4: Modified Vibration Criteria

4-1-2 Data Representation in VC Curves

VC-curves are defined in Root Mean Square (RMS) speed values. The conversion between the metrics (acceleration-velocity-displacement) is rather straightforward: the velocity at frequency f_0 can be found by multiplying the displacement at f_0 with $2\pi f_0$; similarly, multiplying the velocity with $2\pi f_0$ will give the acceleration at f_0. Therefore, one can use any of the metrics for representing the spectrum of a signal as long as it is clearly stated which one is used. Note that, in our generalized plant model (3-15), we have defined the floor vibration in terms of its velocity, hence we do not need any transformation for the metrics.

Most common spectrum representations in vibration analysis are constant bandwidth RMS spectrum (narrow-band), one-third octave RMS spectrum (proportional bandwidth) or Power Spectral Density (PSD) [23]. VC-curves are defined as a one-third octave RMS spectrum. One-third octave RMS spectra $R_{1/3oct}(f)$ can be approximated from PSD $S(f)$ by using [24]:

$$R_{1/3oct}(f) = \left(\int\limits_{\sqrt[-6]{2}f_i^{ctr}}^{\sqrt[6]{2}f_i^{ctr}} S(f)df \right)^{1/2} \tag{4-1}$$

As a result, the PSD values of VC-curves $S_{VC}(f)$, in a bandwidth BW_i can be estimated as:

$$S_{VC}(f) = \frac{\left(RMS_{VC}\right)^2}{BW_i} \quad , \sqrt[-6]{2}f_i^{ctr} \leq f \leq \sqrt[6]{2}f_i^{ctr} \tag{4-2}$$

where RMS_{VC} is the constant velocity RMS value of any of the VC-curves:

$$\begin{aligned} VC_A &= 50\mu/s \\ VC_B &= 25\mu/s \\ VC_C &= 12.5\mu/s \\ VC_D &= 6\mu/s \\ VC_E &= 3\mu/s \end{aligned} \tag{4-3}$$

Moreover, the bandwidth BW_i in (4-2) is proportional to the center frequency f_i^{ctr}:

$$BW_i = f_i^{ctr}(\sqrt[6]{2} - \sqrt[-6]{2}) \tag{4-4}$$

and relationship between 2 consecutive center frequencies are [25]:

$$f_{i+1}^{ctr} = 2^{1/3} f_i^{ctr} \tag{4-5}$$

PSDs of the VC-C, VC-D and VC-E curves according to the modified vibration criteria (Figure 4-4) are provided below in Figure 4-5, which are obtained by using the formula (4-2) where the center frequencies can be found in Table 4-1.

Table 4-1: Center Frequencies for Modified Vibration Criteria

$i =$	1	2	3	4	5	6	7	8	9
f_i^{ctr}	0.5Hz	0.63Hz	0.79Hz	1Hz	1.26Hz	1.59Hz	2Hz	2.52Hz	3.17Hz
$i =$	10	11	12	13	14	15	16	17	18
f_i^{ctr}	4Hz	5.04Hz	6.35Hz	8Hz	10.08Hz	12.7Hz	16Hz	20.16Hz	25.4Hz
$i =$	19	20	21	22	23				
f_i^{ctr}	32Hz	40.32Hz	50.8Hz	64Hz	80.64Hz				

.

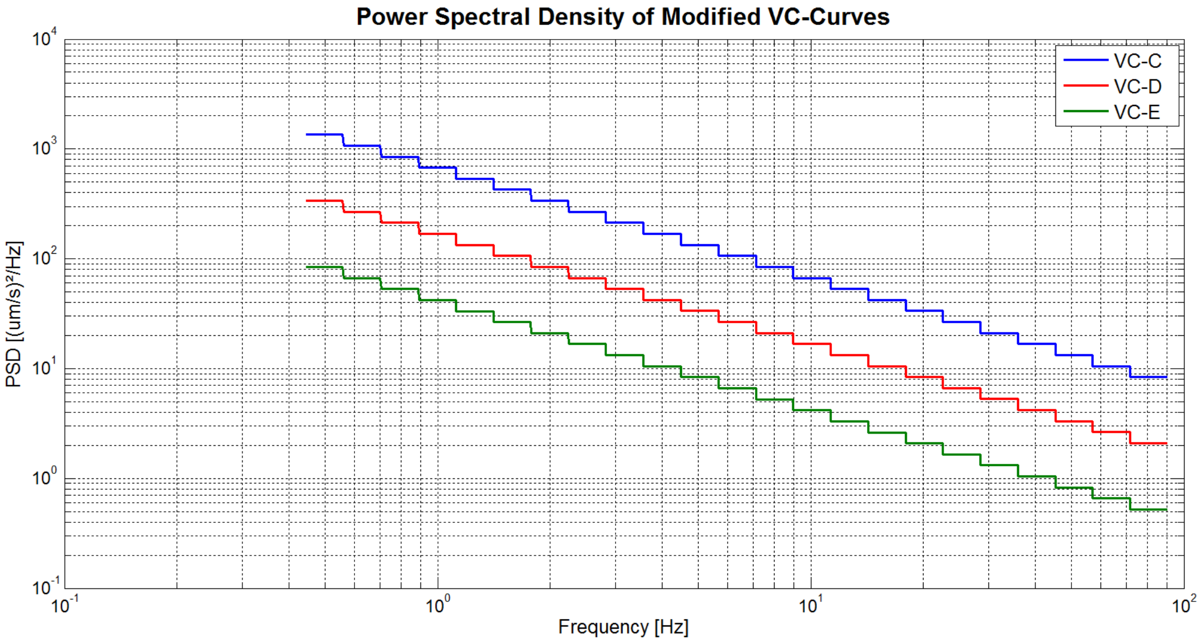

Figure 4-5: PSD of VC-curves for the Modified Vibration Criteria

Figure 4-5 shows that power of the floor vibration becomes smaller as we go to higher frequencies. Recall that, we have used the center frequencies between 0.5 Hz and 80 Hz. In other words, the power of the floor vibration between 0.44 Hz and 90.49 Hz is modelled according to the modified VC-curves.

One of the important concerns for the performance evaluation is to define the frequency range of interest. The idea of using soft mount isolation is to eliminate the vibration at high frequencies and actively dampen out the peaks at natural frequencies. The frequency range $0.44 - 90.49$ Hz for PSD of ground vibration is therefore adequate for performance analysis of our system. As the rigid body modes are inside this frequency range, the performance of both active and passive vibration isolation can be evaluated.

4-1-3 Discussion on Modeling Floor Vibration

In this section, we have introduced VC-curves, which are floor specifications used for performance evaluation of the facility floor. Typically, VC-curves are used in the concept design phase as a guidance for the level of floor vibration. Nevertheless, we can analyse the performance of AVIS for different VC-curves, meaning for different floor specifications. VC-curves show flat characteristics in one-third octave band RMS velocity. They are converted to PSD, which is the power of a signal in terms of frequency.

4-2 Sensor Noise

Sensor noise can be included in the model by considering that different origins (thermal noise, shot noise, $1/f$ noise etc.) have a flat spectrum up to a certain frequency. Then the total sensor noise can be found by summing up the power contributions of each origin [26].

A straightforward solution to estimate the noise is to excite the geophone with a known signal U and measure the output X as shown in Figure 4-6.

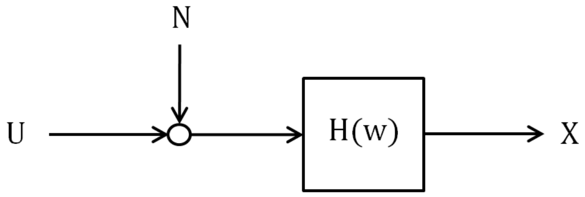

Figure 4-6: Input, Noise and Output for Geophone H(w)

We have seen how a model of $H(w)$ can be derived in Section 3-4-2. The motion U requires some kind of shaker that we did not have available. For this thesis, we got a reference [4], which is a suggestion for determination of the sensor noise based on measuring the coherence of the output of two geophones without knowing the input. Next, we will summarize the technique presented in [4] and discuss its practical value. The block diagram model in Figure 4-7 illustrates the experiment.

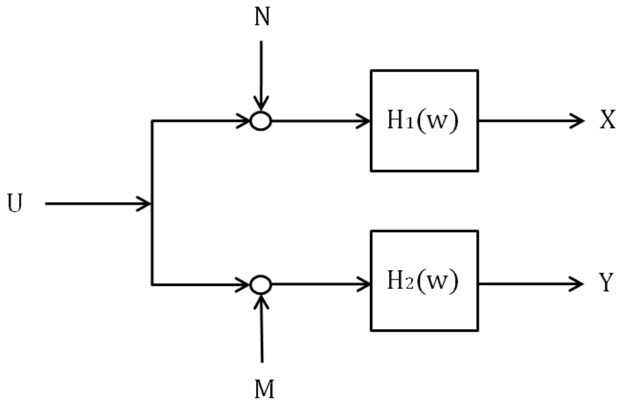

Figure 4-7: Block Diagram of the Noise Modeling Experiment [4]

Two geophones with transfer functions $H_1(w)$, $H_2(w)$ are put on the floor next to each other, such that they are driven by the same input signal U, which is the floor vibration. Instrumental noise at each geophone is represented by N and M. It is assumed that noise generators within the separate instruments, while statistically independent, produce equal levels of noise power:

$$S_{NN}(w) = S_{MM}(w) \tag{4-6}$$

Furthermore, the geophones are considered to have an identity transfer function:

$$H_1(w) = H_2(w) = 1 \tag{4-7}$$

Under these assumptions, PSD of the noise $S_{NN}(w)$ can be calculated from PSD of the output $S_{XX}(w)$ by using the coherence γ^2_{XY} between the two outputs [4]:

$$S_{NN}(w) = S_{XX}(w)(1 - \sqrt{\gamma^2_{XY}}) \tag{4-8}$$

where the coherence γ^2_{XY} can be obtained from the PSDs using:

$$\gamma^2_{XY}(w) = \frac{|S_{XY}(w)|^2}{S_{XX}(w)S_{YY}(w)} \tag{4-9}$$

The equation (4-8) suggests that, when the assumptions (4-6) and (4-7) are satisfied, then the PSD of the sensor noise can simply be calculated by using the measured PSD of the output signal S_{XX} and the coherence between the two output signals γ_{XY}. On the other hand, (4-7) is not a good assumption because due to internal dynamics of the geophone, transfer function from the floor velocity to the measured velocity is not equal to one at the frequencies lower than the natural frequency of the geophone. This was already discussed in the previous chapter, see also Figure 3-9, where the natural frequency is given as approximately 4.5 Hz in the datasheet of the producer. Therefore, the method is expected to be valid for frequencies higher than the natural frequency of the geophone ($f > 4.5$Hz), where the transfer function is 1. Note that, once dynamics $H_1(w)$, $H_2(w)$ are introduced, we could not estimate the noise. Before using the method to estimate the noise level after 4.5 Hz, we make a simulation experiment to test it.

4-2-1 Testing the Robustness of the Method

In order to test the method, we simulate the experiment described in Figure 4-7. We assume that the noise levels are equal and the transfer functions $H_1(w)$ and $H_2(w)$ are both equal to 1. Hence the assumptions (4-6) and (4-7) are satisfied. PSDs of the output signals $S_{XX}(w)$, $S_{YY}(w)$ and noise signals $S_{NN}(w)$, $S_{MM}(w)$ are provided in Figure 4-8. Notice that, output PSD was chosen 100 times bigger than the noise PSD. Then we applied the formula (4-8) to estimate the noise level using the coherence (4-9). The result is shown in Figure 4-9. Moreover, the mean values for the real noise PSD and calculated noise PSD are shown for comparison. The ratio of the mean values are approximately 1.8 which is not bad from engineering point of view.

To summarize, the technique can be used to approximate the noise level for frequencies bigger than 4.5 Hz, where the transfer function of the geophone is 1. In order to estimate the noise level after 4.5 Hz, the experiment is conducted with GS-11D type of geophones [4].

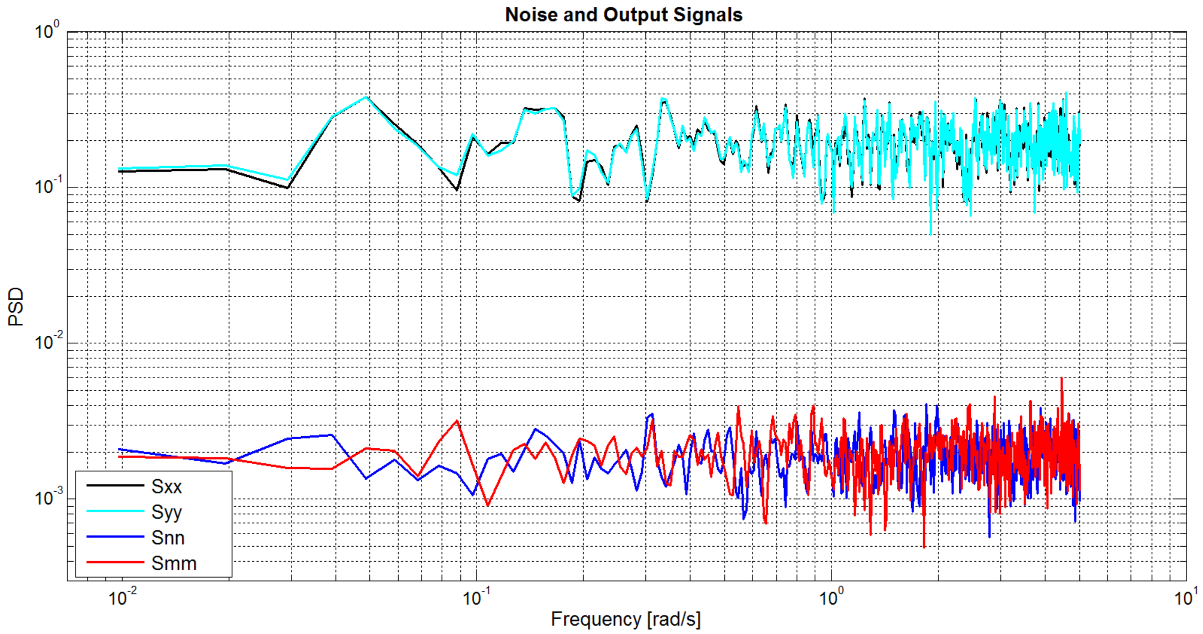

Figure 4-8: PSD of the Output Signals X,Y and Noise N,M

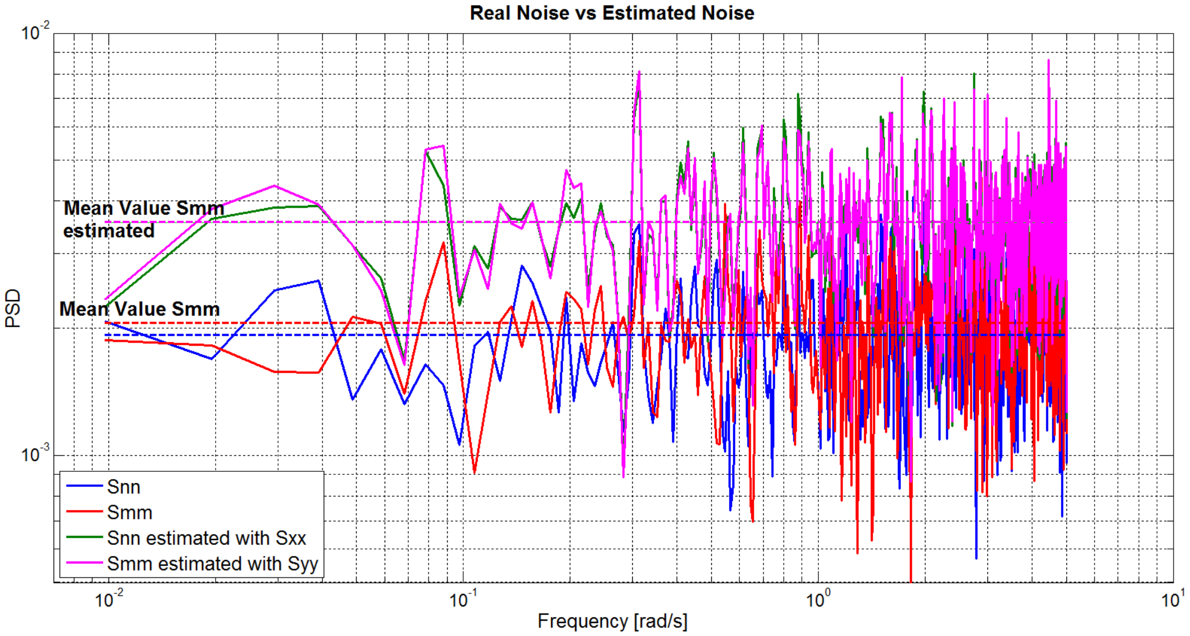

Figure 4-9: Real vs Estimated Noise Levels and Their Mean Values

4-2-2 Conducting the Experiment

Experiment described in Figure 4-7 is conducted by putting 2 same geophone types (GS-11D) next to each other onto the factory floor. Since the geophones are very close to each other, we expect that the velocity inputs are the same. The noise level is calculated according to the formula (4-8).

In Figure 4-10, PSD of the output signal $X(f)$ and noise $N(f)$ are shown. PSD of the output signal X represents the measured PSD of the floor vibration in velocity squared. We can analyze level of the floor vibration with respect to level of the noise by looking at Figure 4-10. For comparison VC-E curve is also provided.

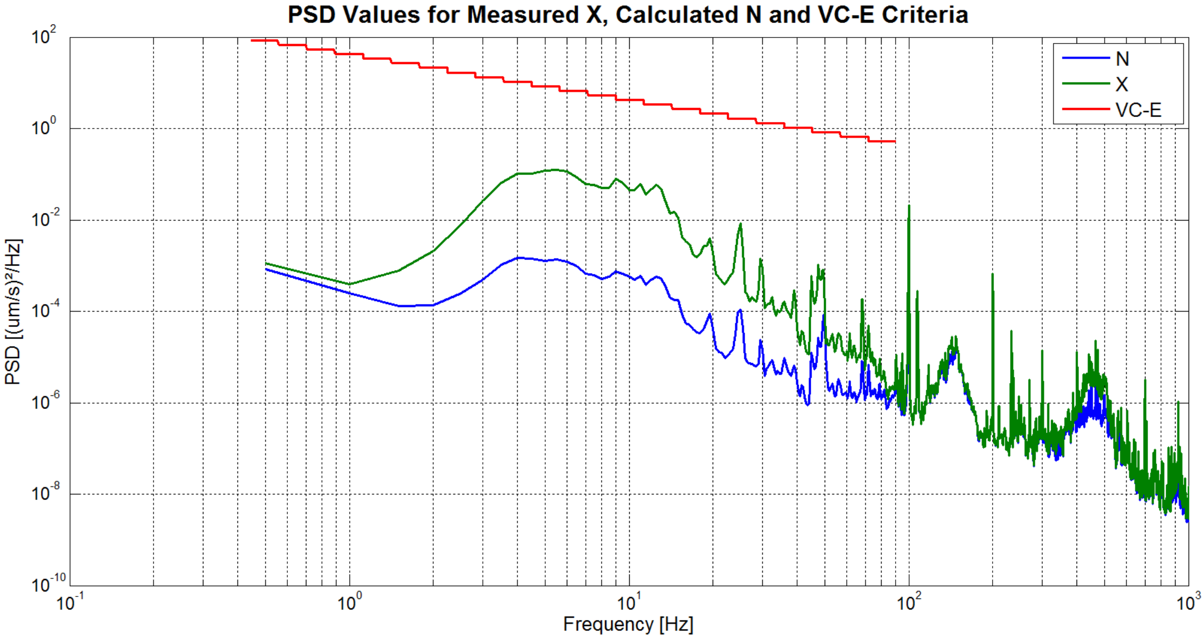

Figure 4-10: PSD Values for Output Signal X and Calculated Noise N

In Figure 4-10, measured PSD of the output signal is approximately 100 times the calculated PSD of the sensor noise for frequencies between $4.5 - 40$ Hz and between $40 - 70$ Hz it is 10 times bigger. Moreover, powers of the output signal and the noise after 70 Hz are almost the same. Note that, we can not estimate the noise level for frequencies lower than 4.5 Hz, since the assumption (4-7) does not hold.

4-2-3 Discussion on Modelling the Sensor Noise

In this section, a technique from [4] is discussed to measure the instrumental noise of a geophone. This technique is especially interesting because it proposes a method to calculate the noise level when the input signal is not known. However, the technique could only be shown to work for the frequencies higher than the natural frequency of the geophone (≈ 4.5Hz).

Based on the results, it is difficult to model the noise at the geophones, since the method fails exactly at the frequencies which are the most important. In order to proceed with the framework, in which models for floor vibration and sensor noise are needed, we can roughly approximate the noise power as a scaled version of the floor vibration, which means that the PSD of the geophone noise is a scaled version of the PSD of the VC-curves. Or another alternative is to model the sensor noise as having a flat power spectrum, by extrapolating level of noise estimate at higher frequency. Here the choice is left to the engineer.

On the other hand, we believe that this difficulty at defining the sensor noise level is not very essential for the performance analysis. That is because we do not know in practice how much the sensor noise has an impact on the overall performance. However, we do know that the parasitic voltage due to the rotations are crucial. This was already mentioned at the end of the Section 3-4-2. Although the geophones are used to measure the translational velocities, rotation of the geophone changes the magnetic flux inside it, resulting in a parasitic voltage which disturbs the accuracy of the measurement. The need for elimination of this horizontal-tilt coupling is also underlined in [27] and a solution to this is provided by the so-called patented Hummingbird technology. For the details of Hummingbird technology, the reader is directed to the reference [28]. We state here again that the modelling of horizontal-tilt crosstalk is left as a future work.

Chapter 5

Performance Assessment

We can define two kinds of errors for high precision measurement systems: deterministic errors and random errors. For repeated measurements, deterministic errors do not change or their change is predictable. For this thesis, we only consider random errors. Random errors are unpredictable, but they can be represented by a normal distribution. The characteristics of a normal distribution is given by its mean value $\bar{x}$ and variance σ_x^2. For n measurements these terms are calculated as:

$$\begin{aligned} \bar{x} &= \frac{1}{n}\sum_{i}^{n} x_i \\ \sigma_x^2 &= \frac{1}{n-1}\sum_{i}^{n}(x_i - \bar{x})^2 \end{aligned} \tag{5-1}$$

These values are useful when defining random signals. Mean and variance of a random signal can be found by:

$$\begin{aligned} \bar{x} &= \lim_{T\to\infty}\frac{1}{2T}\int_{-T}^{T} x(t)dt \\ \sigma_x^2 &= \lim_{T\to\infty}\frac{1}{2T}\int_{-T}^{T} (x(t) - \bar{x})^2 dt \end{aligned} \tag{5-2}$$

Moreover, power of a signal is also proved to be very useful when representing random signals. The power of a random signal is defined as:

$$P_x = \lim_{T\to\infty}\frac{1}{2T}\int_{-T}^{T} x(t)^2 dt \tag{5-3}$$

Here, power is just a mathematical expression, it does not mean the physical power. Square root of the power is defined as the Root Mean Square (RMS) value. Notice that, variance σ_x^2 is the power of a signal P_x around its mean $\bar{x}$. Since we consider AC only signals for calculating the error, the mean value is zero. Hence variance and standard deviation become equal to power and RMS value of the signal respectively. As a result, we will use σ value of the performance signal as it directly relates power and RMS of the signal with variance and standard deviation of the error, which makes this quantity rather easy to interpret.

Recall that in the previous chapter, we have discussed how to model the disturbances in terms of their Power Spectral Density (PSD)s. In this chapter, we will use two methods to calculate σ value of the performance channels when PSD of the inputs are known. The first method is based on computation of Cumulative Power Spectrum (CPS), which is a graphical representation of the cumulative power with respect to frequency. By computing the PSD of the system output corresponding to each of the disturbance sources, one can visualize how each disturbance contributes to the performance, and at which frequencies this happens. This method is called Dynamic Error Budgeting (DEB), see [29] for the details of DEB. The second method is the computation of H_2 norm of the system. This method is based on approximating a colouring filter for the floor vibration and sensor noise. Moreover, we will discuss the application of both methods and underline their advantages and disadvantages based on illustrative examples and a case study.

5-1 Power Spectral Density and Cumulative Power Spectrum

Sofar, we introduced the σ value of a signal in time domain (5-2) and underline its connection to the power of a signal. PSD describes how the power of a signal is distributed with frequency. Hence, in frequency domain power of a signal y can be found using PSD function $S_y(w)$:

$$\sigma_y^2 = \frac{1}{2\pi} \int\limits_{-\infty}^{\infty} S_y(w) dw \tag{5-4}$$

Then RMS value can be calculated as:

$$\sigma_y = \sqrt{\frac{1}{2\pi} \int_{-\infty}^{\infty} S_y(w) dw} \tag{5-5}$$

Therefore, in order to obtain a quantitative measure of the performance, we can calculate RMS of the performance channels σ using the PSD functions $S(w)$. In the next section we will show how to calculate the PSD of the output for multiple inputs.

5-1-1 Obtaining PSD of the Output

Theory of Propagation

For a closed loop Single-input Single-output (SISO) system with a transfer function $H(s)$, PSD of the output $S_y(w)$ can be calculated from PSD of the input $S_u(w)$ using the formula [30]:

$$S_y(w) = |H(jw)|^2 S_u(w) \tag{5-6}$$

where $|H(jw)|$ is Bode magnitude of the transfer function from input u to the output y. For multi-variable signals, the propagation formula becomes [29]:

$$S_y(w) = H(jw)S_u(w)H^*(jw) \tag{5-7}$$

where * is the complex conjugate transpose.

Remember that, we have modelled the floor vibration in x, y and z as 3 mutually independent vibrations in order to keep the calculations simple. Moreover, it was assumed that the sensors are 7 uncorrelated noise sources. Therefore, the PSDs of the disturbance inputs are considered to be all uncorrelated among each other. Hence, $S_u(w)$ is diagonal for both floor vibration $u = \mathbf{w}$ and sensor noise $u = \mathbf{n}$, meaning that the Cross Spectral Density (CSD) of the inputs are zero. On the other hand, since we have couplings between the motions, CSD of the outputs are not zero.

Performance with Multiple Input Sources

The schematic that we have shown when obtaining transmissibility and noise sensitivity in Section 3-5-3 is repeated here without showing the block matrices:

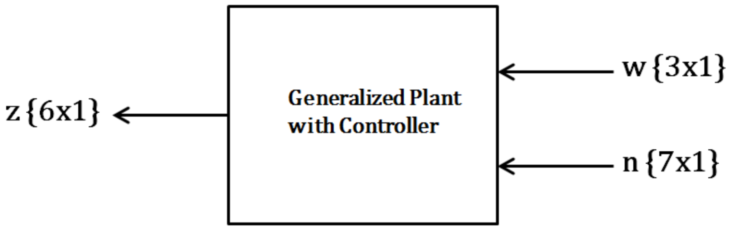

Figure 5-1: Inputs $\mathbf{w}$, $\mathbf{n}$ and Performance Channel $\mathbf{z}$ of the System

We define the performance criteria for each input/output channel separately. Therefore, when we evaluate performance, we will consider the motion only in single Degree of Freedom (DOF). Hence the performance signal $\mathbf{z}$ is defined as the motion along either x, y, z, α, β or γ. Thus, the transfer functions from floor vibration $\mathbf{w}$ and sensor noise $\mathbf{n}$ to performance channel $\mathbf{z}$ are Multi-input Single-output (MISO).

Using the theory of propagation (5-7) one can calculate the total power of a single performance channel $\mathbf{z}$ resulting from floor vibration $\mathbf{w}_{3x1}$ and sensor noise $\mathbf{n}_{7x1}$ by using sum of the squares formula [26]:

$$\sigma_{\mathbf{z}}^2 = \sigma_1^2 + \sigma_2^2 \tag{5-8}$$

where

$$\begin{aligned}\sigma_1^2(w) &= G_{wz}(jw)S_w(w)G_{wz}^*(jw)\\ \sigma_2^2(w) &= G_{nz}(jw)S_n(w)G_{nz}^*(jw)\end{aligned} \tag{5-9}$$

where in this case G_{wz} and G_{nz} are MISO real rational transfer matrices with dimensions (1x3) and (1x7) respectively. Moreover, $S_w(w)$ and $S_n(w)$ are the diagonal PSD matrices for floor vibration and sensor noise respectively.

As a result, when the disturbances are described in terms of PSD, and the transfer functions from corresponding disturbance to the performance channel is known, we can find their combined effect on the performance using (5-8).

5-1-2 Calculating Cumulative Power Spectrum

Using PSD one can obtain the total power at each frequency due to different disturbance sources. However, in a PSD graph, because of its logarithmic scale, it is difficult to determine whether a small peak at higher frequencies has less or more energy than a broad bulge at lower frequencies [27]. This, however, is nicely made visible by so-called CPS, defined by:

$$CPS(w_{end}) = \int_0^{w_{end}} PSD(v)dv \tag{5-10}$$

where $PSD(v)$ here refers to one-sided power spectral density function. Notice that, $CPS(w_{end})$ represents the total power of a signal up to the frequency w_{end}. Taking the root of the end value $CPS(w_{end})$ gives the RMS of the signal between frequencies $0 - w_{end}$:

$$\sigma = \sqrt{CPS(w_{end})} \tag{5-11}$$

Hence, CPS is very suitable for comparing the effects of different disturbance sources and it is rather straightforward to quantify total resulting error in terms of the RMS value.

Next, we will investigate the same illustrative example that we have discussed in Section 3-5-4 to show the trade-off between transmissibility and sensor noise sensitivity. However, this time we will use CPS and RMS velocity instead of the magnitude Bode diagrams for evaluating the performance.

5-1-3 Illustrative Example 2

For this example, we consider the performance in terms of velocity along the vertical axis $\mathbf{z} = \dot{z}$. Thus RMS value show average error in vertical velocity. The disturbances are floor vibration in vertical axis Z_f and sensor noise in 3 vertical sensors S_{z_1}, S_{z_3}, S_{z_4}. For the moment, the disturbances are assumed to be uncorrelated white noise signals with $S_u(w) = 1$. Figures below provide CPS for transmissibility and sensor sensitivity. The result clearly shows the trade-off between the two performance measures.

In Figures 5-2, 5-3, 5-4 cumulative power of the performance channel is shown on the left axis. Corresponding RMS values are also provided for comparison.

In Figure 5-2, CPS makes a peak around the natural frequencies of the system for the passive isolation. This peak is reduced by using skyhook damping. Hence, it is clear that active isolation increases performance for transmissibility such that the RMS value is decreased from 9.37mm/s to 2.548mm/s (for $\mathbf{K_v} = 5$) and to 1.308mm/s (for $\mathbf{K_v} = 20$).

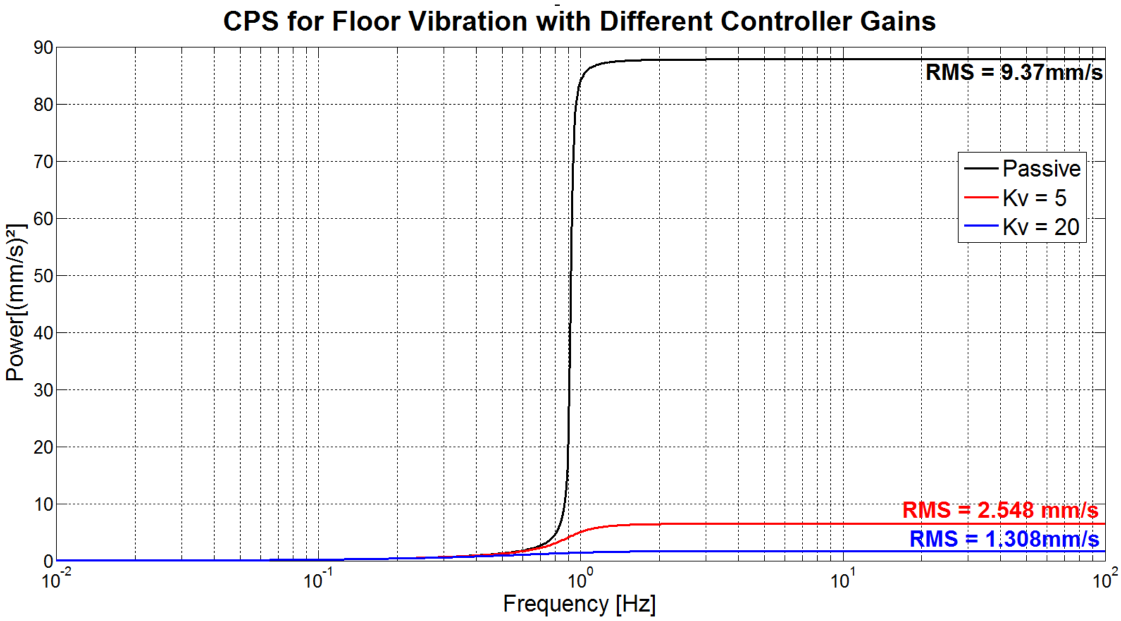

Figure 5-2: CPS for Vertical Transmissibility

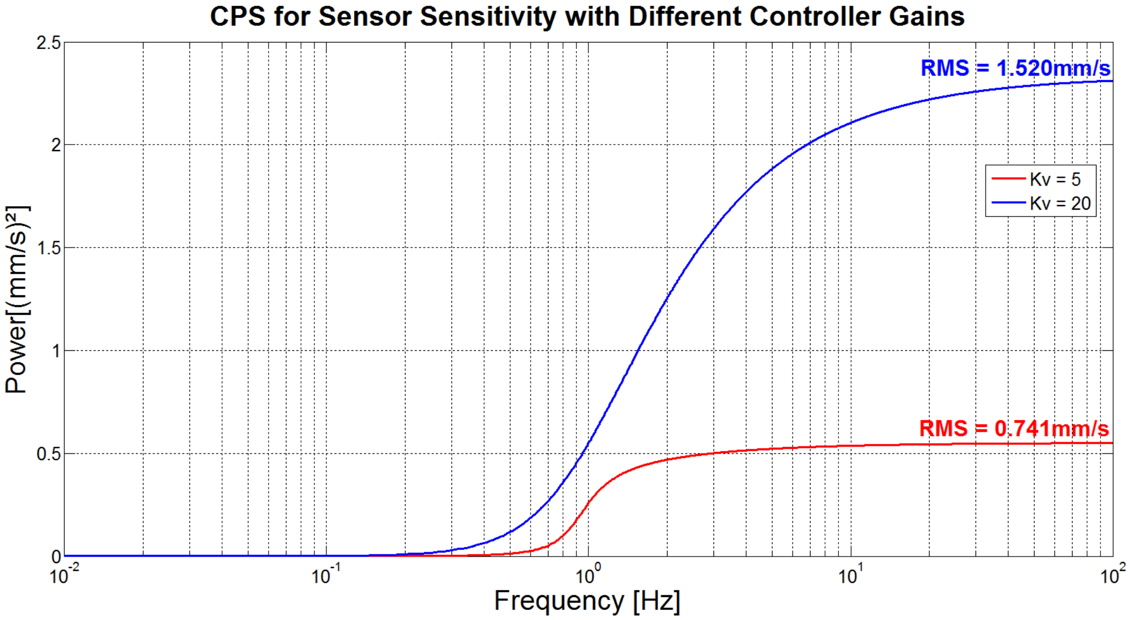

Figure 5-3: CPS for Vertical Sensor Noise

On the other hand, Figure 5-3 shows that, increasing controller gain increases sensitivity to sensor noise, hence decreases the performance. Notice that, for high controller gain $\mathbf{K_v} = 20$, error due to sensor noise (1.520mm/s) is even larger than error due to floor vibration (1.308mm/s).

Moreover, in Figure 5-4, we provide total CPS in vertical axis for three different controller gains resulting from both vertical floor vibration and vertical sensor noise.

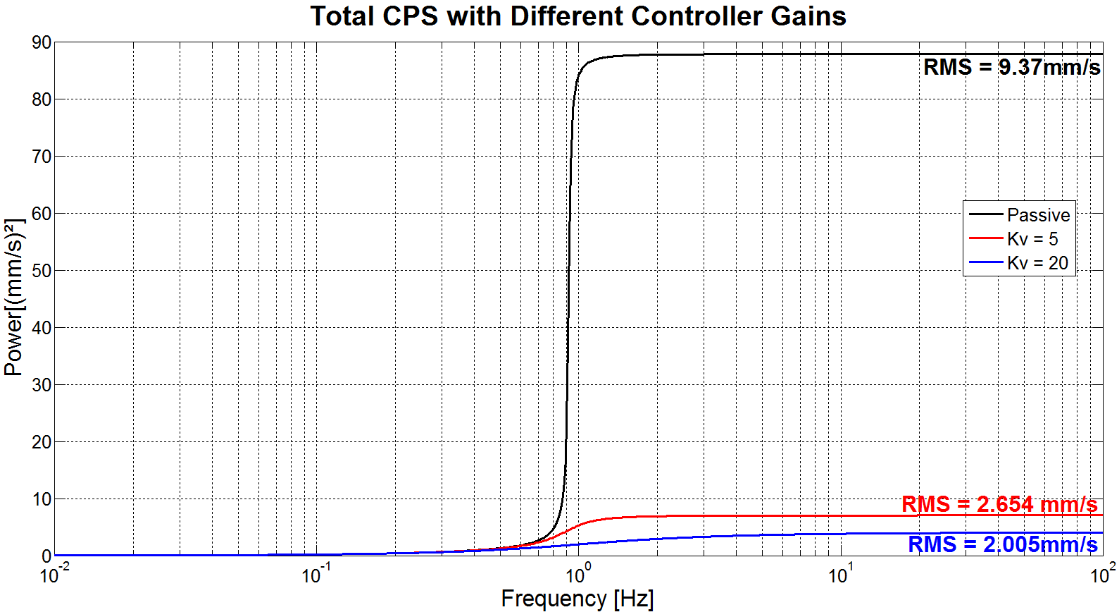

Figure 5-4: Total CPS

The results also provide us important information about at which frequencies the power is concentrated. For small controller gains, power is concentrated around the natural frequency of the system, while for higher controller gains power is distributed in a larger frequency band.

We need to underline here several important issues when numerically calculating CPS using formula (5-10).

First, it is clear that we do not have to do the calculations beginning from $w_b = 0$ Hz, since neither floor vibration nor sensor noise has significant power contribution for frequencies less than $f = 0.1$ Hz. Hence, if we begin numerical integration from 0.1 Hz, we will neglect only tiny amount of power and RMS value will be almost the same. This can be advantageous if we are dealing with large amounts of data.

Second, similar to the beginning frequency, choosing the end frequency w_{end} for integration is also crucial. For example, CPS graph of sensor noise (Figure 5-3), does not arrive at an end value at higher frequencies when $\mathbf{K_v} = 20$; where for floor vibration (Figure 5-2), CPS curve is already converged at 1 Hz. That means, when $\mathbf{K_v} = 20$ we have neglected small amount of sensor noise at frequencies larger than 100 Hz. Therefore, we expect that calculated RMS (until 100Hz) for sensor noise is a bit smaller than its total value. Indeed, when we increase the end frequency from 100 Hz to 200 Hz, RMS value increases from 1.520mm/s to 1.527mm/s.

Third issue is the number of gridding points. When numerically integrating a non-smooth function, number of gridding points should be as small as possible to increase the accuracy of integration. For this simulation we increased the frequency by 0.01 Hz. Lightly damped systems like air-mounts can show high peaks at their natural frequencies. See the peak at the natural frequency of vertical motion in Figure 3-16. Therefore, we may expect accuracy loss for passive isolation system when calculating CPS for transmissibility. Nevertheless, optimum number of frequency points for an application can be found by calculating the CPS for smaller grid points and observing if the total power changes.

5-2 H$_2$ Norm

Figure 5-1 is a representation of the active vibration isolation system where the inputs are defined as the floor vibration (**w**) and sensor noise (**n**); the output (**z**) is defined as the motion of a point in terms of velocity (or displacement). For a good performance against disturbances, the performance signal **z** should be as small as possible. In other words, a good performance for such a system is the measure of the amplification provided by the system for given input [31]. In order to quantify how small the attenuation is, some system norms are used. One of these system norms is H_2 norm which can be used to compute the total energy of the output. In the frequency domain, it is defined as:

$$||H(s)||_2 = \sqrt{\frac{1}{2\pi}\int_{-\infty}^{\infty} tr[H^*(jw)H(jw)]dw} \tag{5-12}$$

where $||H(s)||_2$ denotes the H_2 norm of the transfer function $H(s)$ and tr is the trace operator.

5-2-1 Stochastic Interpretation of H$_2$ Norm

RMS Value

Remember that, in (5-5) we have defined the RMS of a signal σ_y using the PSD function. Moreover, in (5-7) we have provided the formula for calculating the PSD of the output signal given the PSD of the input signal $S_u(w)$ for the system $H(jw)$. Putting (5-7) into (5-5), we can find the RMS value of the output σ_y by using $S_u(w)$ and $H(jw)$:

$$\sigma_y = \sqrt{\frac{1}{2\pi}\int_{-\infty}^{\infty} H(jw)S_u(w)H^*(jw)dw} \tag{5-13}$$

Moreover, if we consider the input to be a white noise signal with a unity PSD:

$$S_{white}(w) = 1 \tag{5-14}$$

then, (5-13) reduces to:

$$\sigma_y = \sqrt{\frac{1}{2\pi}\int_{-\infty}^{\infty} H(jw)H^*(jw)dw} \tag{5-15}$$

Notice that, for SISO systems, the definition of H_2 norm (5-12) is equal to the definition of RMS for a system with white noise input signal (5-15) and it can be calculated as:

$$||H(s)||_2 = \sigma_y = \sqrt{\frac{1}{2\pi}\int_{-\infty}^{\infty} |H(jw)|^2 dw} \tag{5-16}$$

To formulate the relation for MISO case, consider $H(jw)$ as a 1x3 transfer function with 3 inputs and 1 output:

$$H(jw) = \begin{bmatrix} H_1(jw) & H_2(jw) & H_3(jw) \end{bmatrix} \tag{5-17}$$

where $H_i(jw)$ represents the SISO transfer function from the white noise input u_i to the output y. The complex conjugate transpose of $H(jw)$ can be found by first taking the transpose and then taking the complex conjugate of each entry:

$$H^*(jw) = \begin{bmatrix} H_1^*(jw) & H_2^*(jw) & H_3^*(jw) \end{bmatrix}^T \tag{5-18}$$

Here, $*$ represents the complex conjugate and the transpose operator is denoted by ^{T}. If the 3 white noise inputs are uncorrelated, then $S_u(w)$ is a 3x3 identity matrix and (5-13) becomes:

$$\sigma_y = \sqrt{\frac{1}{2\pi}\int_{-\infty}^{\infty} \begin{bmatrix} H_1(jw) & H_2(jw) & H_3(jw) \end{bmatrix} \begin{bmatrix} 1 & 0 & 0 \\ 0 & 1 & 0 \\ 0 & 0 & 1 \end{bmatrix} \begin{bmatrix} H_1^*(jw) \\ H_2^*(jw) \\ H_3^*(jw) \end{bmatrix} dw} \tag{5-19}$$

Notice that, (5-19) is equal to the definition of H_2 norm (5-12). That means for MISO systems, if the input spectrum is diagonal and CSDs are zero (each component corresponding to a white noise signal), then H_2 norm of the system is the same as RMS value of the output:

$$||H(s)||_2 = \sigma_y \tag{5-20}$$

Therefore, instead of calculating the RMS from PSD of the output, we can directly find it by computing the H_2 norm of the transfer function. Moreover, total power from different uncorrelated sources (floor vibration and sensor noise) can be obtained using sum of the squares formula (5-8).

Next, we will investigate the same illustrative example that we have discussed to show the trade-off between transmissibility and sensor noise sensitivity, and compare the results of H_2 norm and CPS.

5-2-2 Illustrative Example 3

For this example, we have the same inputs ($\mathbf{w} = Z_f$; $\mathbf{n} = \{S_{z_1}\ S_{z_3}\ S_{z_4}\}$) and output ($\mathbf{z} = \dot{z}$) as in Section 5-1-3, which allows us to compare the two methods, namely CPS and H_2.

H_2 norms of the transmissibility and sensor noise sensitivity transfer functions are computed using *norm* function in *Matlab*. Below, we show the results and compare the two methods. Note that, dashed lines show the square of the H_2 norm.

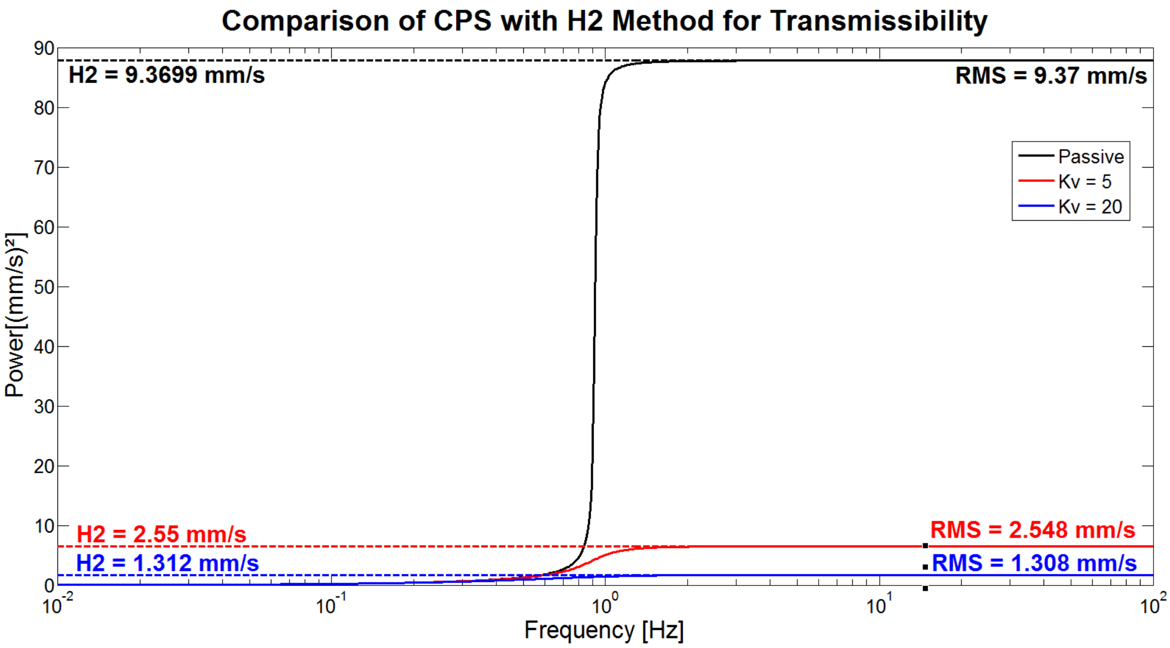

Figure 5-5: Comparison of the Two Methods for Transmissibility

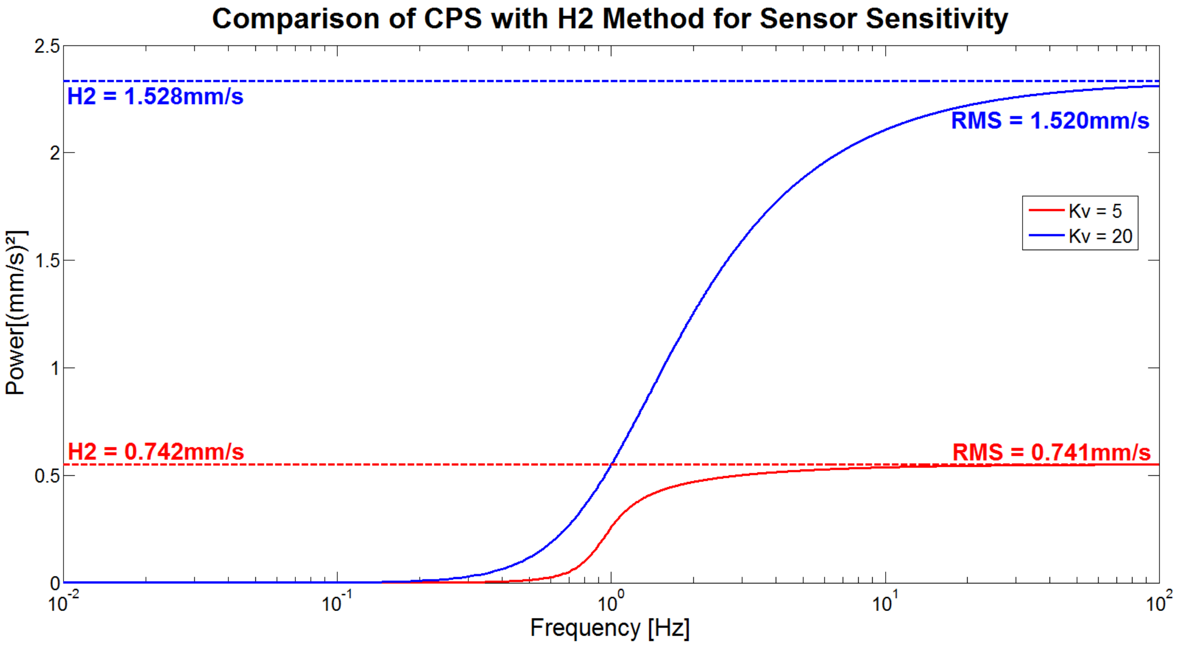

Figure 5-6: Comparison of the Two Methods for Sensor Sensitivity

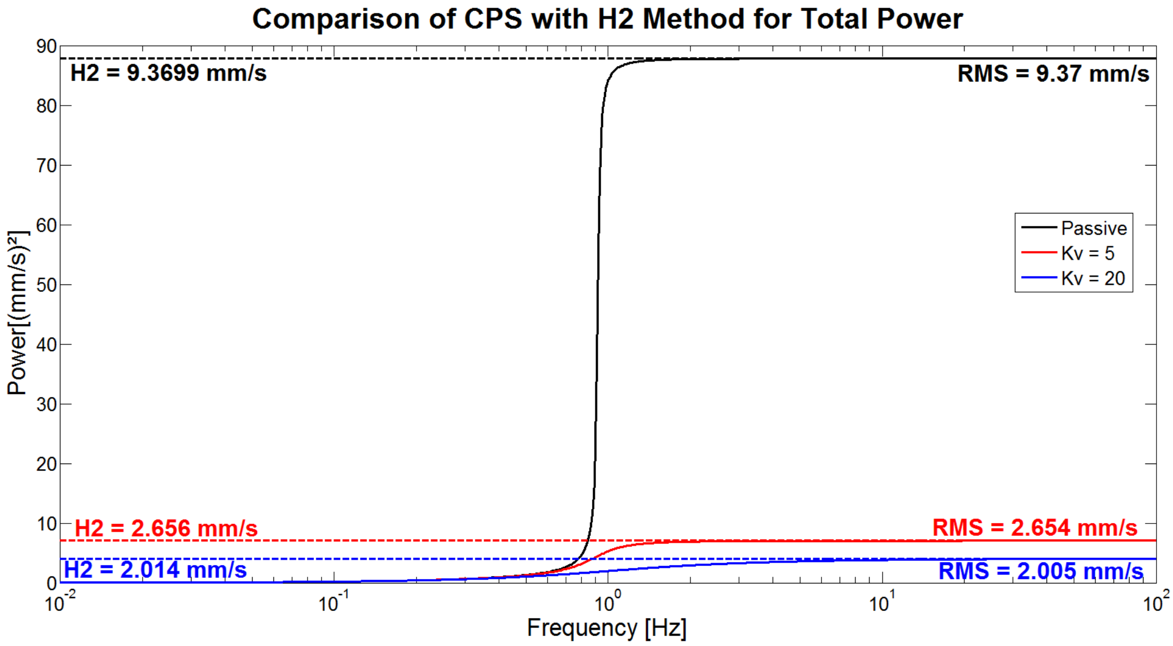

Figure 5-7: Comparison of the Two Methods for Total Power

Instead of computing the integral in (5-12) directly, H_2 norm of a transfer function can be calculated algebraically using the state space matrices [32], which is an important advantage over CPS calculation. Notice that, H_2 norm considers all the frequencies of the frequency response function: $w \in [\infty, -\infty]$. Therefore, we do not have the same considerations about defining the frequency range and number of grid points as in calculating CPS. This is an important advantage because determining frequency gridding points requires knowledge about the system (eigen-frequencies).

In the previous illustrative example, we have argued possible error sources when calculating CPS. For the transmissibility of the passive system (Figure 5-5), H_2 norm is 0.0001mm/s smaller than RMS value, which in theory is not possible. This can be explained by the expected accuracy loss of CPS due to the peak at natural frequency. Indeed, when the simulation is run again with the same beginning and end frequency, but this time for smaller gridding ($f_{grid} = 0.001\text{Hz}$ instead of $f_{grid} = 0.01\text{Hz}$) RMS value for transmissibility of the passive system decreases to 9.3689mm/s.

The results show that, H_2 norm computation is more robust and easier than using CPS function to calculate the RMS value. Next, we will consider another illustrative example where we will compute H_2 norm for different configurations of the isolators.

5-2-3 Illustrative Example 4

In this example, we will analyze how the system sensitivity to sensor noise changes for different configurations of the isolators. We will examine the sensitivity for different vertical distances where in the first simulation $h_1 = 210\text{mm}$, in the second $h_1 = 0\text{mm}$. In Figure 5-8, we illustrate the two different configurations of the isolation system:

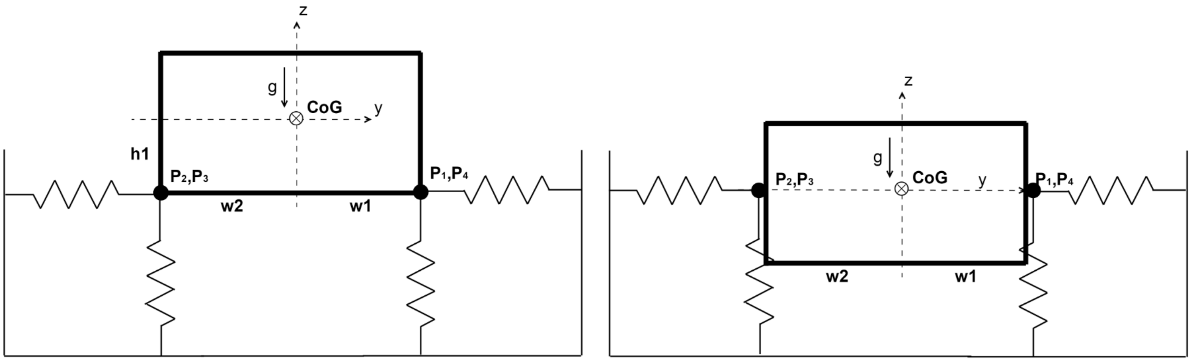

Figure 5-8: Two Different Configurations of the Isolators

In the first analysis we consider white noise input signals only at the vertical sensors S_{z_1}, S_{z_3}, S_{z_4}. These sensors are used for sensing the motion in logical axis for $\dot{z}_L$, $\dot{\alpha}_L$, $\dot{\beta}$, which is clear from the equations in (3-34). Hence, noise at these sensors basically cause vertical disturbance forces at the points of action. We compute the H_2 norm of the transfer function from these sensors to the performance channel $\mathbf{z}$ for each degree of freedom (x, y, z, α, β, γ) to interpret the sensitivity to vertical sensor noise with respect to different h_1. The results are shown below in Table 5-1.

Table 5-1: H2 norm due to Vertical Sensors for Different Heights

	$\dot{x}$	$\dot{y}$	$\dot{z}$	$\dot{\alpha}$	$\dot{\beta}$	$\dot{\gamma}$
$h_1 = 210\text{mm}$	0.512	0.512	1.53	2.49	2.49	0
$h_1 = 0\text{mm}$	0	0	1.53	2.65	2.65	0

Since the vertical sensors S_{z_1}, S_{z_3}, S_{z_4} are used for $\dot{z}_L$, $\dot{\alpha}_L$, $\dot{\beta}_L$, sensor noise cause error in z, α, β. Furthermore, when $h_1 \neq 0$, the system motion in x and y is coupled with β and α respectively, as we have concluded in Chapter 2. This is clearly visible when looking at the H_2 norms. Vertical forces at points of action cause rotations along α and β; in particular when $h_1 \neq 0$, we obtain error also along y and x.

In the second analysis we consider white noise input signals only at the horizontal sensors S_{x_1}, S_{y_2}, S_{x_3} and S_{y_4}. These sensors are used for sensing the motion in logical axis for $\dot{x}_L$, $\dot{y}_L$, $\dot{\gamma}_L$, which is clear from the equations (3-34). Noise at these sensors basically cause horizontal disturbance forces in the xy-plane. We compute the H_2 norm of the transfer function from these sensors to the performance channel $\mathbf{z}$ for each degree of freedom to interpret the sensitivity to horizontal sensor noise with respect to different h_1. The results are shown below in Table 5-2.

Table 5-2: H2 norm due to Horizontal Sensors for Different Heights

	$\dot{x}$	$\dot{y}$	$\dot{z}$	$\dot{\alpha}$	$\dot{\beta}$	$\dot{\gamma}$
$h_1 = 210\text{mm}$	1.44	1.44	0	0.897	0.897	2.62
$h_1 = 0\text{mm}$	1.53	1.53	0	0	0	2.62

Since the horizontal sensors S_{x_1}, S_{y_2}, S_{x_3}, S_{y_4} are used for $\dot{x}_L$, $\dot{y}_L$, $\dot{\gamma}_L$, sensor noise cause error along the axes x, y, γ. Furthermore, horizontal forces at points of action cause rotations α and β; in particular when $h_1 \neq 0$.

Consequently, using H_2 norm, we can understand the system and easily interpret how the performance changes with different configurations.

5-2-4 Spectral Decomposition and PSSSID

In Chapter 4, we have discussed about modelling the floor vibration and sensor noise in the system. In order to keep our analysis more appropriate for the concept design phase, we have argued to use Vibration Criteria Curves (VC-curves) as floor specification.

H_2 norm measures square root of steady state power -or RMS of the output response- to unit white noise inputs. However, unlike white noise, PSD of VC-curves does not show flat characteristics (see Figure 4-5). Therefore, in order to compute the error for the disturbances with VC spectra, we need to find a colouring filter $F_C(s)$, which fits to the PSD of VC-curves in the following sense: The response of $F_C(s)$ given a white noise input is a signal with the desired PSD of the VC-curves. This is illustrated in Figure 5-9.

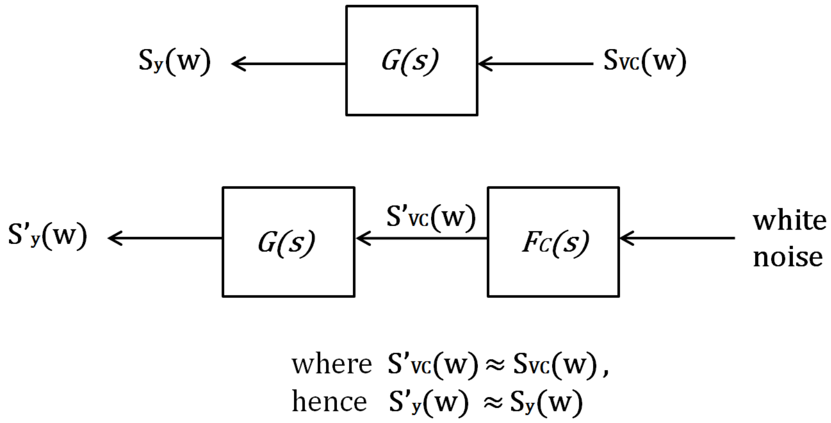

Figure 5-9: Approximating the Input Spectra with a Colouring Filter $F_C(s)$

As a result, RMS value of the output σ_y for the coloured noise input $S_{VC}(w)$ can be estimated as:

$$\sigma_y = ||H(s)||_2 \tag{5-21}$$

where

$$H(s) = G(s)F_C(s) \tag{5-22}$$

The procedure of obtaining a colouring filter $F_C(s)$ is called spectral factorization. Power Spectrum SubSpace IDentification (PSSSID) is one of the spectral factorization algorithms in the literature that approximates the colouring filter for a given power spectrum [33]. We will apply this algorithm in order to obtain $F_C(s)$ for VC-curves. However, the algorithm PSSSID is particularly powerful as it can be applied to multivarible PSD leading to Multi-input Multi-output (MIMO) filter $F_C(s)$.

PSSSID is an identification algorithm that is based on a wide field known as subspace identification techniques. It estimates the state space matrices (A, B, C, D) of a minimum-phase spectral factor $F_C(s)$ from a given discrete time frequency domain power spectrum. The user can provide the model order by looking at the singular values of the Hankel matrix. The accuracy of the fit is quantified by means of the cost function:

$$J = \sum_{k=1}^{N} vec_S(\Phi_k - \Phi_k')^T W_k vec_S(\Phi_k - \Phi_k') \tag{5-23}$$

where Φ_k is the equidistantly distributed samples of the original spectrum and Φ_k' is the estimated power spectrum of the filter $F_C(s)$. Optionally the user can specify a frequency dependent weighting function W_k, which makes it possible to improve the accuracy at a certain frequency band. Interested reader may refer to [33] for details.

Applying PSSSID to Approximate the VC-curves

PSSSID algorithm is applied to approximate VC-D curve. Previous discussions and illustrative examples show that, low frequencies are more critical than high frequencies for the isolation system. Therefore, we want to increase the fit at lower frequencies. To achieve this, frequency dependent weighting function is chosen as $1/f$. By looking at the Hankel sigular values, the order of the filter is selected to be $n = 4$. The result is shown in Figure 5-10.

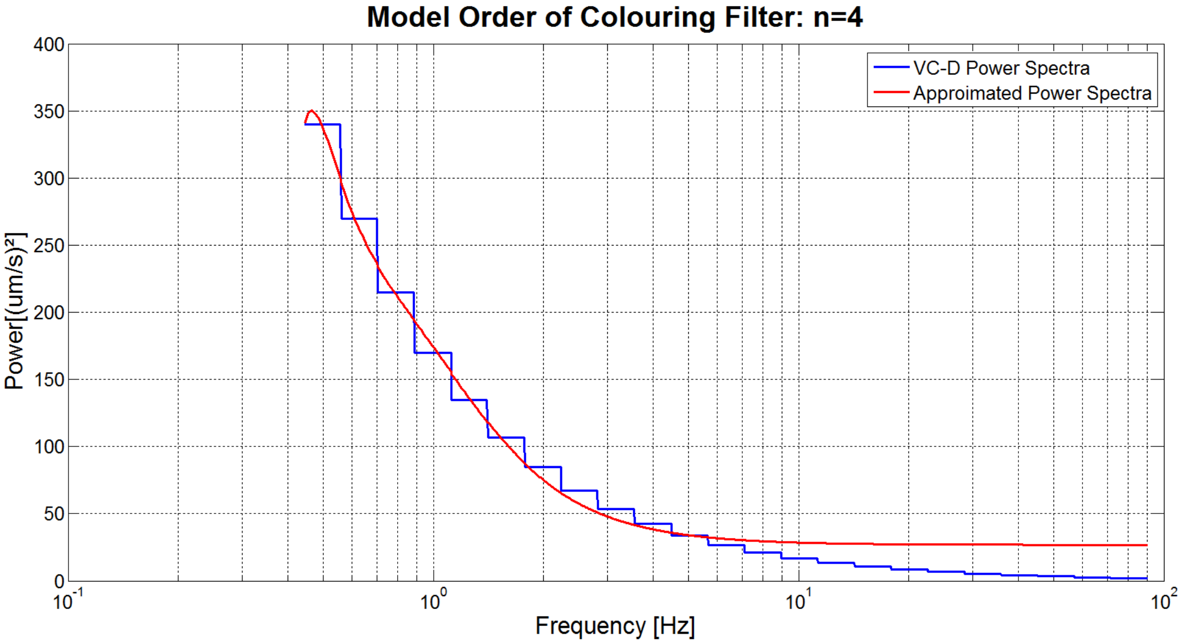

Figure 5-10: Approximating the VC-D Spectra with a Colouring Filter F(s) of Order n=4

In order to check how good the fit is, error between the real and estimated spectra is calculated for each frequency. Absolute value of the error is shown in Figure 5-11.

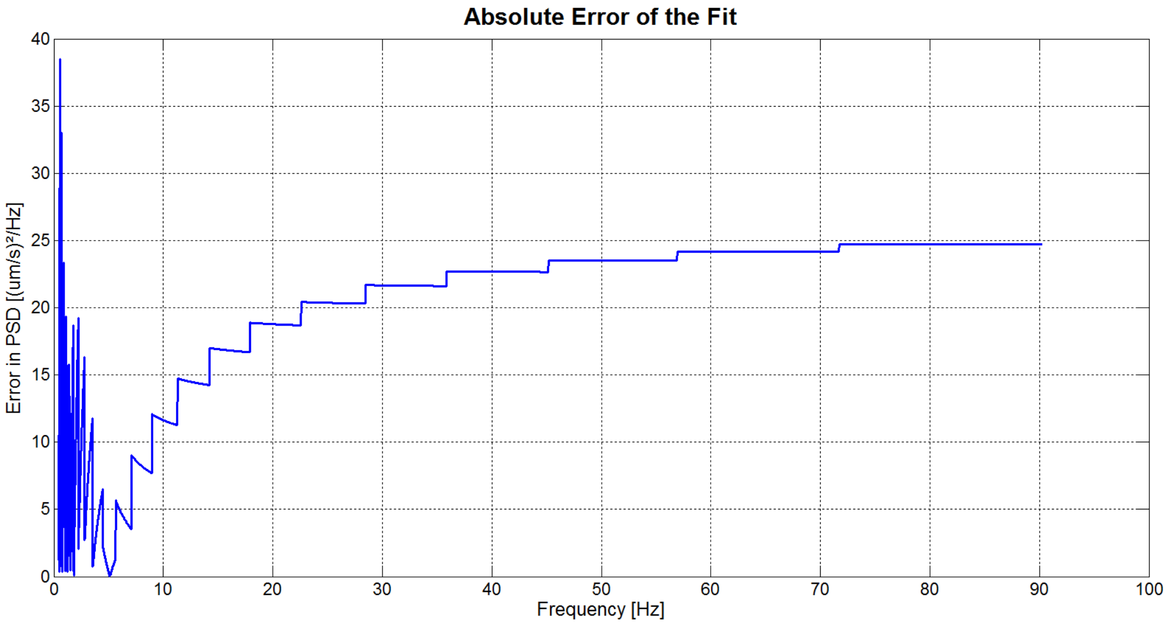

Figure 5-11: Absolute Error of the Fit vs. Frequency

As we increase the order, we observe that the error at low frequencies does not necessarily decrease. This is due to the big jumps of the VC power spectra at low frequencies. Moreover, we are not concerned about the errors at high frequencies, since high frequency vibrations are eliminated by the isolation system. Still looking at Figure 5-10, we can conclude that the filter does estimate VC spectra in the sense that both graphs are exponentially decaying and have approximately same magnitudes. Therefore, we conclude that, power spectrum of a floor satisfying VC-D criteria can be approximated by the colouring filter $F_C(s)$ calculated by the PSSSID.

If we now use PSSSID algorithm to compute a colouring filter $F_C(s)$ for an input with VC-D spectrum, combining our results, the velocity RMS value of the performance channel $\sigma_{\mathbf{z}}$ is equal to the H_2 norm:

$$\sigma_{\mathbf{z}} = ||G_i(s)F_C(s)||_2 \tag{5-24}$$

where $G_i(s)$ is the transfer function from some disturbance input with VC-D spectrum to the performance channel $\mathbf{z}$.

Next, we will compare the overall performance of two different configurations by taking advantage of H_2 norm and CPS.

5-3 Case Study

In this section we will compare the dynamic performance of the active vibration isolation system for two different configurations. The two configurations can be seen in Figure 5-8, where the top view of the Active Vibration Isolation System (AVIS) can be seen in Figure 3-11. In the first case, the body is supported from below its Center of Gravity (CoG). In the second case vertical distance of the isolators to the CoG is zero. We will compare the performance in vertical direction, hence the RMS value of the vertical performance channel will be calculated.

Values of the physical parameters are given in Table 5-3. The definition of all parameters are summarized in Figure 3-3.

Table 5-3: Values of the Parameters

Physical Parameter	Symbol	Value
Horizontal Springs	$k_{pi} = k_{qi}$	12 [N/mm]
Vertical Springs (Right)	$k_R = k_{r1} = k_{r4}$	15.38 [N/mm]
Vertical Springs (Left)	$k_L = k_{r2} = k_{r3}$	19.7 [N/mm]
Damping	$d_{xi} = d_{yi} = d_{zi}$	0.1 [N/(mm/s)]
Distance along x	d	615 [mm]
Distance along y for Points P1,P4	w_1	570 [mm]
Distance along y for Points P2,P3	w_2	445 [mm]
Mass	m	2.1 [tones]
Gravity	g	9810 [mm/s^2]
Moment of Inertia along X	Ixx	48000 [tones x mm^2]
Moment of Inertia along Y	Iyy	50000 [tones x mm^2]
Moment of Inertia along Z	Izz	64000 [tones x mm^2]
Rotation Angles	θ_i	0 [deg]
Skyhook Damping for each DoF	k_{vi}	50

Moreover, in the first configuration the height is equal to $h_1 = 210$mm while it is $h_1 = 0$mm in the second configuration. Level of floor vibration is not available at the time but we assume that the floor satisfies VC-D criteria. Therefore, we will use the same colouring filter $F_C(s)$ that we have found with PSSSID algorithm at the end of the previous section. Since we have assumed that the x, y, z vibrations of the floor are uncorrelated, we can extend the colouring filter for multi-variable white noise inputs as:

$$\mathbf{W_F(s)} = diag(F_C(s))_{3x3} \tag{5-25}$$

Similarly, the sensor noise is assumed have a flat PSD with a value of $20[(\mu\text{m/s})^2/\text{Hz}]$, which corresponds to the PSD of VC-D curve at 10 Hz. Then, 7 uncorrelated sensor noise power can be approximated by the filter:

$$\mathbf{W_N} = diag\left(\sqrt{20}\right)_{7x7} \tag{5-26}$$

Adding the input weights (5-25) and (5-26) to the block matrices of the overall system we can represent the system as driven by white noise inputs which is shown in Figure 5-12.

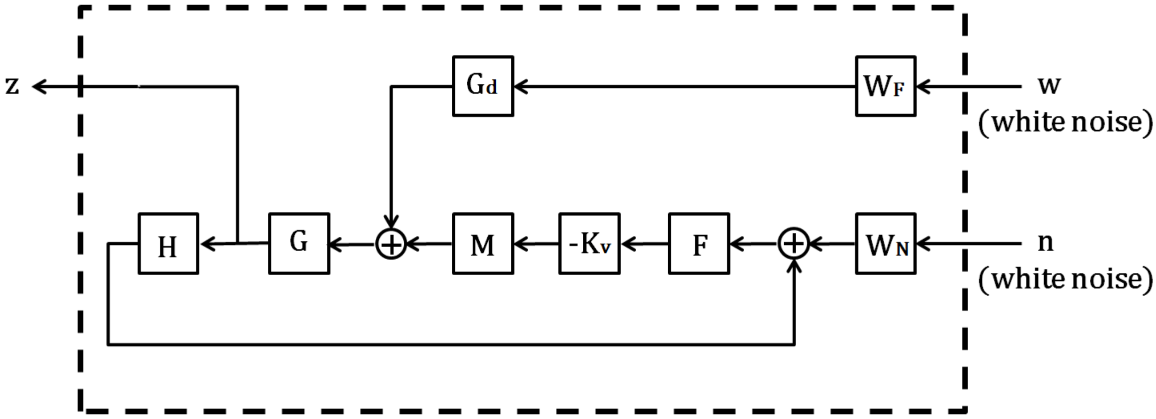

Figure 5-12: Block Matrices with Colouring Filters $\mathbf{W_F}$ and $\mathbf{W_N}$

Now, in order to compute the RMS value of the performance channel $\mathbf{z}$, we calculate the H_2 norm of the transfer function from all the inputs $\mathbf{w}_{3x1}$ and $\mathbf{n}_{7x1}$ to $\mathbf{z} = \dot{z}$:

$$\begin{aligned} \sigma_{\mathbf{wz}} &= ||G_{wz}(s)||_2 \\ \sigma_{\mathbf{nz}} &= ||G_{nz}(s)||_2 \end{aligned} \tag{5-27}$$

where

$$\begin{aligned} G_{wz}(s) &= [(I + \mathbf{GMK_vFH})^{-\mathbf{1}}\mathbf{GG_dW_F}]_{1x3} \\ G_{nz}(s) &= [(I + \mathbf{GMK_vFH})^{-\mathbf{1}}\mathbf{GM}(-\mathbf{K_v})\mathbf{FW_N}]_{1x7} \end{aligned} \tag{5-28}$$

Results for $h_1 = 210$mm and $h_1 = 0$mm are shown in Table 5-4.

Table 5-4: Velocity RMS Values for Different Heights Computed with H2 Norm [μm/s]

	Floor Vibration	Sensor Noise	Total
$h_1 = 210$mm	13.8169	11.1981	17.7850
$h_1 = 0$mm	13.8097	11.2137	17.7892

According to Table 5-4, we can conclude that the first configuration, where $h_1 = 210$mm, results in less error in terms of velocity. On the other hand, the difference between the two errors are very small. Moreover, we provide the PSD values of the performance channel for $h = 0$mm due to floor vibration and sensor noise in Figure 5-13.

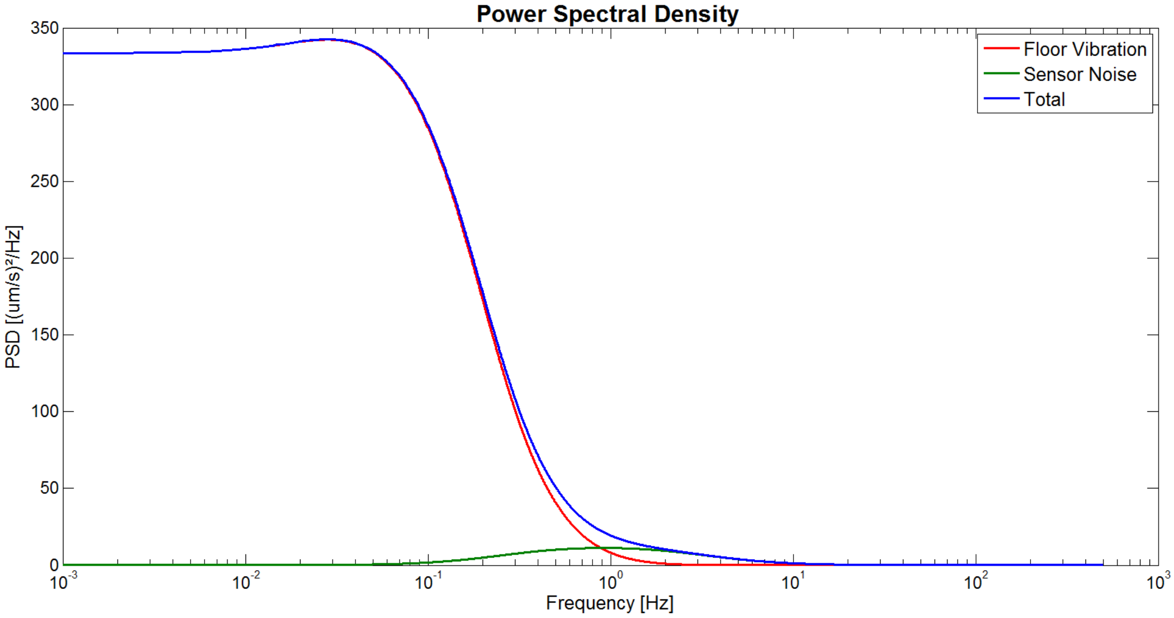

Figure 5-13: Power Spectral Density for $h_1 = 0$mm

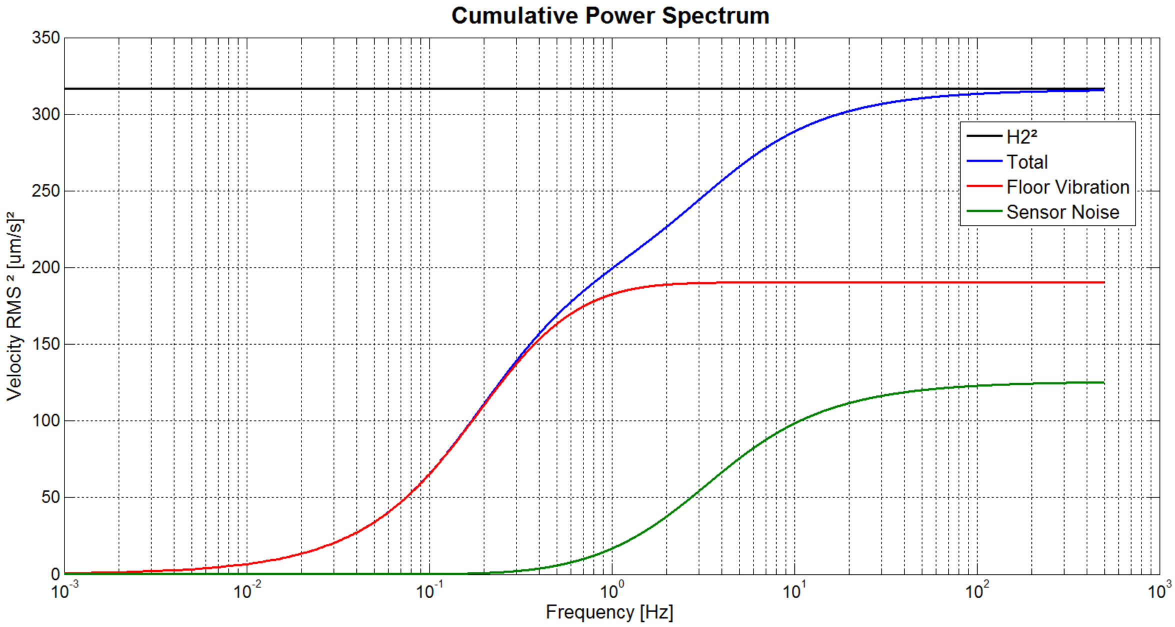

Figure 5-14: Cumulative Power Spectrum for $h_1 = 0$mm

As we have discussed before, PSD can be misleading, because it is difficult to know if a small peak at higher frequencies has more energy than a big bulge at lower frequencies. In order to identify at which frequencies the power is concentrated, CPS due to floor vibration and sensor noise is shown in Figure 5-14.

Frequency points for PSD and CPS calculation are chosen between $0.001 - 500$ Hz with a grid of 0.001 Hz. By looking at the CPS, we can see that the output power is concentrated approximately between the frequencies $0.01 - 100$ Hz.

Furthermore, Figure 5-15 shows a time simulation of the floor velocity in z and the performance channel $\mathbf{z} = \dot{z}$, which is the vertical velocity of the CoG. These are obtained by giving a white noise input to the system. Notice that, the standard deviation of the CoG is 13.8739μm/s, which is very close to the H_2 norm due to the floor vibration.

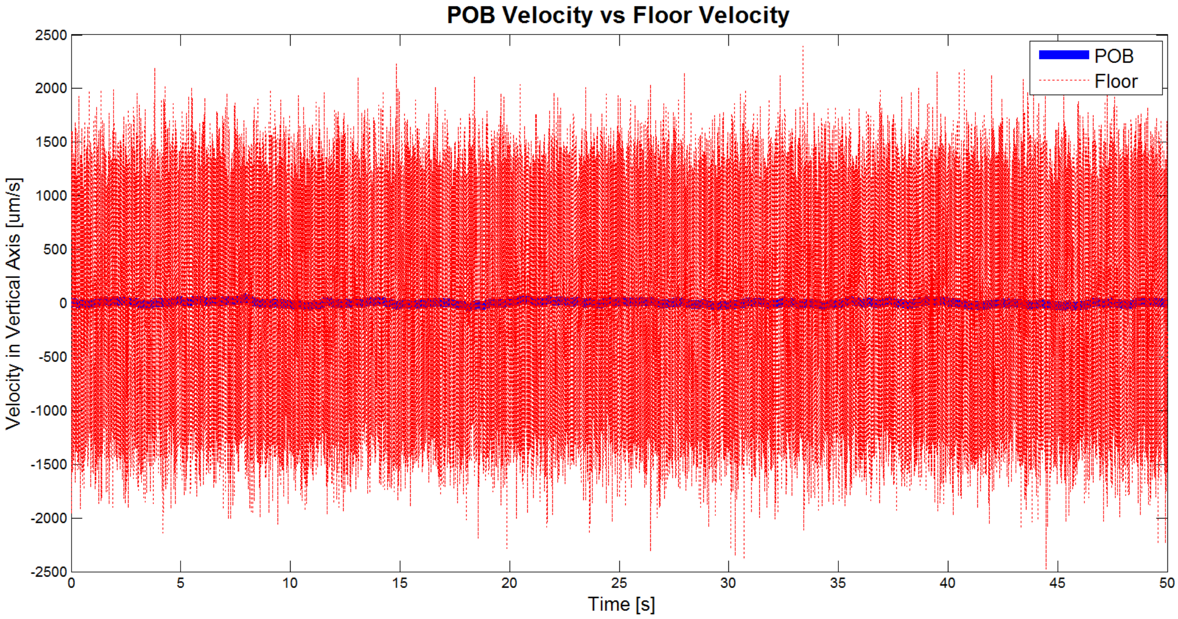

Figure 5-15: Floor and CoG Velocity in Vertical Axis vs Time for $h_1 = 0$mm

Now, more interesting would be to calculate the total error in terms of position in order to roughly estimate which precision we can achieve for the both configurations of the system. To do this, performance is defined as $\mathbf{z} = z$. However, H_2 norm of the transfer function from floor velocity to $\mathbf{z} = z$ becomes infinity, because the magnitude of the transfer function goes to infinity when frequency goes to minus infinity. On the other hand, by looking at the velocity CPS in Figure 5-14, we see that the increase in the power before 0.01Hz is very low, which means that contribution of the signals with lower frequencies can be neglected. Therefore, to numerically compute the integral after 0.01 Hz, we define the following integration operator $\Upsilon(s)$:

$$\Upsilon'(s) = \frac{1}{s + 0.02\pi} \tag{5-29}$$

By calculating the H_2 norm of the the series connection between $\Upsilon(s)$ and the transfer function from disturbance inputs to $\mathbf{z} = \dot{z}$, we can obtain the RMS value of the error in terms of position (z):

$$\sigma_{\mathbf{wz}} = ||\Upsilon'(s)G_{wz}(s)||_2$$
$$\sigma_{\mathbf{nz}} = ||\Upsilon'(s)G_{nz}(s)||_2 \tag{5-30}$$

where $G_{wz}(s)$ and $G_{nz}(s)$ can be found in (5-28).

The result for two different configurations are shown in Table 5-5. Total RMS value of the position error for both configurations are almost the same.

Table 5-5: Position RMS Values for Different Heights Computed with H2 Norm [μm]

	Floor Vibration	Sensor Noise	Total
$h_1 = 210$mm	50.7618	1.9047	50.7975
$h_1 = 0$mm	50.7626	1.8972	50.7980

Furthermore, in Figure 5-16, we provide the time simulation for the CoG position in vertical axis due to the vertical floor velocity.

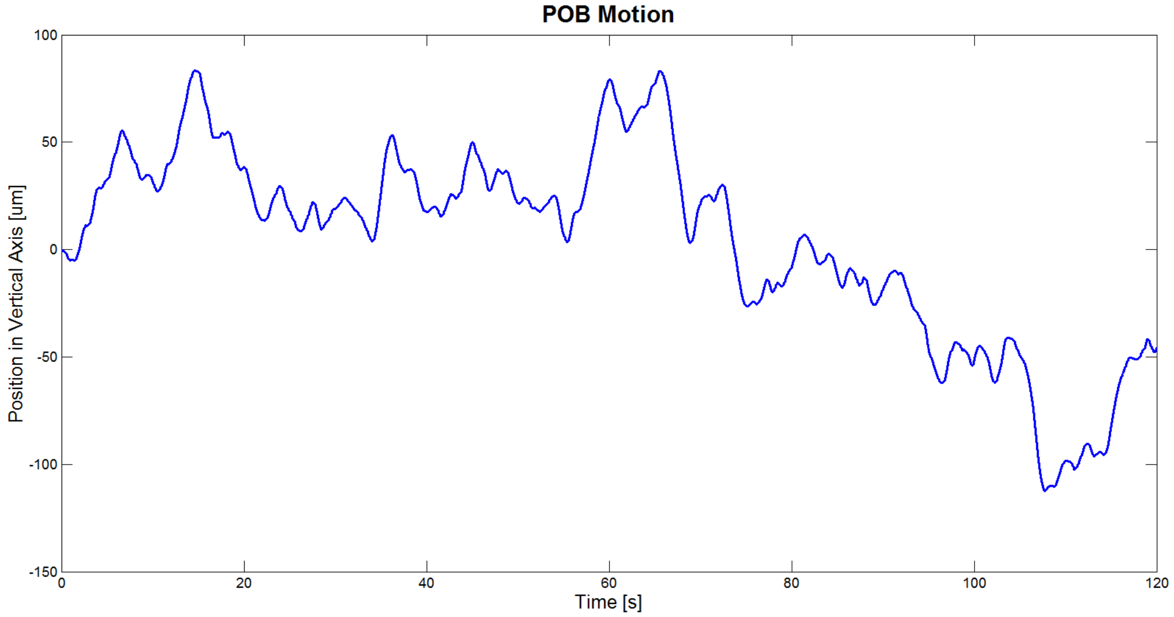

Figure 5-16: Vertical Displacement of CoG due to Vertical Floor Vibration vs Time for $h_1 = 0$mm

The result of the case study shows that our model is robust against changes in vertical distance of the isolators (h_1) for the given floor vibration and sensor noise spectra.

In Appendix B, we provide the *Matlab* code that is used for this case study.

5-4 Summary

In this chapter, we have discussed two methods for measuring the standstill performance in terms of the RMS value. The first method calculates PSD of the performance channel by using power spectrum of the disturbance inputs. Then total power is found by computing the area under PSD curve. In a graphical representation of CPS, we can easily compare the amount of contribution from each disturbance source with respect to frequency. Drawbacks of this method are discussed based on illustrative examples.

Calculating the H_2 norm is the second method to obtain RMS value of the performance channel. Based on an illustrative example, we have shown that this method is more robust than the previous one. However, it calculates the output RMS only when the input is a white noise signal. Therefore, we have introduced the PSSSID algorithm, which estimates a colouring filter to approximate the input power spectrum. Using the colouring filter, we have approximated VC-D criteria. By computing the H_2 norm for the series connection of the colouring filter and system's transfer function (transmissibility or sensor noise sensitivity), we obtain the RMS value of the performance channel.

Lastly, a case study is discussed, where we have applied the methodology that we have developed in order to compare the performance of two different configurations based on CPS and H_2 norm computation.

Chapter 6

Conclusion

6-1 Summary

We have developed a quick performance assessment method for a typical Active Vibration Isolation System (AVIS) as it can be seen in lithography industry. The presented methodology could help engineers to better understand the system by allowing them to quickly compare different system configurations. The methodology consists of 3 steps.

Since we focus on concept phase of a project, we need elementary models to do quick comparisons in order to decide different concept designs. The first step is to obtain the analytical 3 Dimensional (3D) lumped elements model of the 6 Degree of Freedom (DOF) system. The linear model is based on a compact description of mass, stiffness and damping matrices.

In the literature, the models of a rigid body supported by 4 springs are given for the unloaded configuration of the springs, where we consider the loaded configuration of the vertical springs and take into account the effect of gravitational field. Based on the inverse pendulum configuration, we showed a derivation to include the gravity to the linear equations of motion. Moreover, we calculated the natural frequencies of the system in the absence of gravity and with the gravity included. The result shows that the effect of gravity on the dynamics is rather important.

As a result, the obtained elementary 3D model enables us:

- to incorporate gravitational field and its impact on dynamics
- to represent coupling between different DOFs
- to choose different isolator locations and payload inertial properties
- to include subcomponents that represent skyhook control
- to define transmissibility and sensor noise sensitivity as performance measures

Having a model of AVIS the next step is to define the disturbances of the system in terms of their power spectrum. In order to use standardized inputs that can even serve as specification later on, we have used general vibration criteria to model the floor vibration. For the analysis purposes, we have converted Vibration Criteria Curves (VC-curves) from one-third octave Root Mean Square (RMS) values to Power Spectral Density (PSD)s. Then using Power Spectrum SubSpace IDentification (PSSSID) algorithm, we have calculated a colouring filter that approximates the power spectrum of the VC-curves. Moreover, as noise models for geophones are difficult to obtain, we tested an algorithm taken from literature, that is based on 2 geophones that are driven by the same input. Using the algorithm, we estimated the noise level at frequencies above where the geophone dynamics can be neglected, i.e. frequencies higher than 4.5 Hz. However, it is a topic for future research, to model geophone behaviour and sensor noise more accurately.

The third step is to quantitatively measure the performance of the active vibration isolation system. This can be done by computing the H_2 norm of the series connection between the corresponding transfer function and the colouring filter. Moreover the Cumulative Power Spectrum (CPS) provides a graphical representation of performance versus frequency. We have discussed the application of H_2 norm and CPS based on illustrative examples and a case study.

Results show that we can apply the methodology in order to answer questions such as:

- how do parameters of active and passive components realize system performance?
- what is the sensitivity of the system for different configurations of the isolators?
- how can we model floor vibration in terms of PSD functions by using vibration criteria and how the performance changes for different floor specifications?
- what is the effect of noise on the overall performance?
- how do different disturbance sources with certain power spectra contribute to the total error and in which frequencies are they dominant?

6-2 Recommendations for Future Work

In order to use the PSD and the H_2 norm to calculate the RMS value of the performance channels, we have assumed that the disturbances in the system are stochastic. For deterministic disturbances, more appropriate analysing tools should be used.

The sensitivity to sensor noise can be calculated more accurately when the internal dynamics of the geophones and parasitic voltage due to rotational movements are modelled. In particular, when we also model the direct disturbance forces in the system, then we can apply error budgeting to allocate how much each component is allowed to contribute to the total error [34]. In that sense, Dynamic Error Budgeting (DEB) is a promising tool for designing high precision systems. For practical applications of DEB please refer to [29], [35].

The obtained lumped elements 3D model with 6 DOF depends on physical parameters. For a certain system, most of these parameters cannot be measured directly. In case a Finite

Element Modelling (FEM) of the system is available, or the analysis is to be done for a system that exists, identification of the parameters in our model is known as grey-box identification. See [18] where Extended Kalman Filter [36] is used to estimate the unknown parameters of an active vibration isolation system.

The overall performance of the active vibration isolation depends on the configuration of the system. An interesting future work is to express the changes in performance using a Linear Parametric Varying (LPV) model. By capturing the parametric varying behaviour of the system, we can avoid making many iterations over different system configurations and we can describe the uncertainties of the system in a compact way. Especially, we can then be able to analyze the robust performance of the system. Interested reader can refer to [37] for an application of LPV modelling and control of an H-drive unit.

Appendix A

A1

A-1 Deriving the Equations of Motion for 3D Rigid Body

Here we will show how the equations of motion for 3 Dimensional (3D) rigid body supported by 4 isolators can be obtained. We assume the local axis of the springs $\{p_i \ q_i \ r_i\}$ coincide with Center of Gravity (CoG)'s coordinate axis $\{x \ y \ z\}$. Therefore, stiffness of the springs will be denoted with k_{xi}, k_{yi}, k_{zi} for i^{th} spring. Moreover, the isolators have certain symmetry with respect to CoG. The configuration of the body and springs are shown below in Figure A-1.

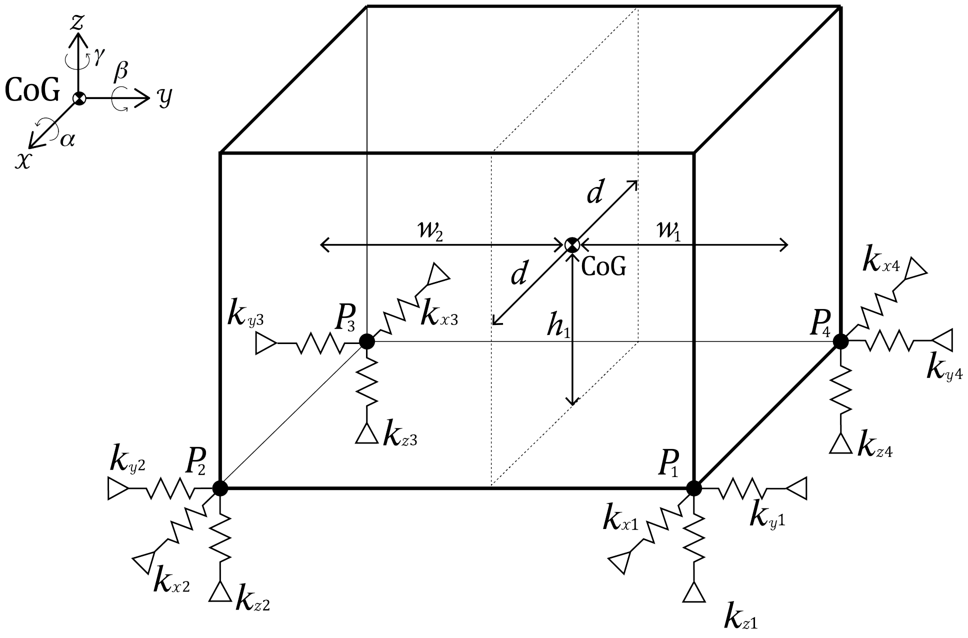

Figure A-1: Configuration of the Body and Springs

It is assumed that the springs have the same free length L_0 and same lengths at the equilibrium L. Moreover, vertical motion is fully decoupled and the body is parallel to the ground at its equilibrium. Furthermore, we assume:

$$\begin{aligned} k_{z1} &= k_{z4} \\ k_{z2} &= k_{z3} \end{aligned} \tag{A-1}$$

Hence, the springs k_{z1}, k_{z2} carry the half of the weight, while the springs k_{z3}, k_{z4} carry the other half. By looking from x, the front view of the body can be seen in Figure A-2:

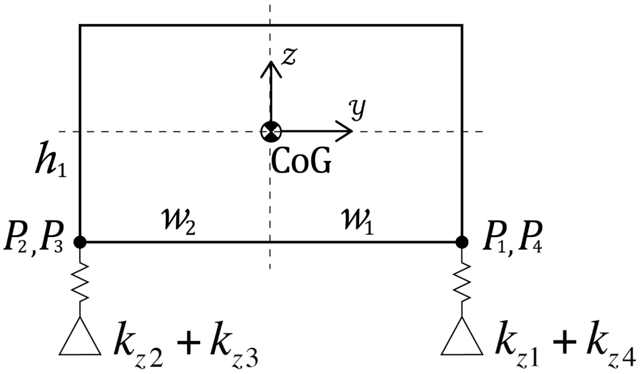

Figure A-2: Projection on yz Plane

Writing the moment equations at the equilibrium, one can obtain:

$$(k_{z1} + k_{z4}) * w_1 = (k_{z2} + k_{z3}) * w_2 \tag{A-2}$$

Moreover, using (A-1) and (A-2) the pre-stress forces $F_{pi,z}$ can be calculated as:

$$\begin{aligned} F_{p1,z} = F_{p4,z} &= \frac{mg}{2} * \frac{w_2}{w_1 + w_2} \\ F_{p2,z} = F_{p3,z} &= \frac{mg}{2} * \frac{w_1}{w_1 + w_2} \end{aligned} \tag{A-3}$$

We can find the negative stiffness values for the horizontal springs by dividing the pre-stress forces to the length of the vertical springs:

$$\begin{aligned} k_{x1-} = k_{y1-} &= -\frac{mg}{2L} * \frac{w_2}{w_1 + w_2} \\ k_{x2-} = k_{y2-} &= -\frac{mg}{2L} * \frac{w_1}{w_1 + w_2} \\ k_{x3-} = k_{y3-} &= -\frac{mg}{2L} * \frac{w_1}{w_1 + w_2} \\ k_{x4-} = k_{y4-} &= -\frac{mg}{2L} * \frac{w_2}{w_1 + w_2} \end{aligned} \tag{A-4}$$

Off-diagonal terms of the inertia tensor J are assumed to be zero and the inertia of the body is constant since the rotations are very small.

Using the first order Taylor approximations, $sin\alpha$ and $cos\alpha$ are assumed to be equal to α and 1 respectively. Then, the equations of motion for CoG around the equilibrium can be obtained by calculating sum the of forces and moments as:

$$
\begin{aligned}
\sum F_x &= m\ddot{x} = F_{x1} + F_{x2} + F_{x3} + F_{x4} \\
\sum F_y &= m\ddot{y} = F_{y1} + F_{y2} + F_{y3} + F_{y4} \\
\sum F_z &= m\ddot{z} = F_{z1} + F_{p1,z} + F_{z2} + F_{p2,z} + F_{z3} + F_{p3,z} + F_{z4} + F_{p4,z} - mg \\
\sum M_x &= J_x\ddot{\alpha} = +(F_{z1} + F_{p1,z}) * (w_1 + d\gamma + h_1\alpha) + F_{y1} * (h_1 - w_1\alpha + d\beta) \\
&\quad - (F_{z2} + F_{p2,z}) * (w_2 - d\gamma - h_1\alpha) + F_{y2} * (h_1 + w_2\alpha + d\beta) \\
&\quad - (F_{z3} + F_{p3,z}) * (w_2 + d\gamma - h_1\alpha) + F_{y3} * (h_1 + w_2\alpha - d\beta) \\
&\quad + (F_{z4} + F_{p4,z}) * (w_1 - d\gamma + h_1\alpha) + F_{y4} * (h_1 - w_1\alpha - d\beta) \\
\sum M_y &= J_y\ddot{\beta} = -(F_{z1} + F_{p1,z}) * (d - w_1\gamma - h_1\beta) - F_{x1} * (h_1 - w_1\alpha + d\beta) \\
&\quad - (F_{z2} + F_{p2,z}) * (d + w_2\gamma - h_1\beta) - F_{x2} * (h_1 + w_2\alpha + d\beta) \\
&\quad + (F_{z3} + F_{p3,z}) * (d - w_2\gamma + h_1\beta) - F_{x3} * (h_1 + w_2\alpha - d\beta) \\
&\quad + (F_{z4} + F_{p4,z}) * (d + w_1\gamma + h_1\beta) - F_{x4} * (h_1 - w_1\alpha - d\beta) \\
\sum M_z &= J_z\ddot{\gamma} = -F_{x1} * (w_1 + h_1\alpha + d\gamma) + F_{y1} * (d - w_1\gamma - h_1\beta) \\
&\quad + F_{x2} * (w_2 - h_1\alpha - d\gamma) + F_{y2} * (d + w_2\gamma - h_1\beta) \\
&\quad + F_{x3} * (w_2 - h_1\alpha + d\gamma) - F_{y3} * (d - w_2\gamma + h_1\beta) \\
&\quad - F_{x4} * (w_1 + h_1\alpha - d\gamma) - F_{y4} * (d + w_1\gamma + h_1\beta)
\end{aligned}
\tag{A-5}
$$

where spring forces F_{xi}, F_{yi}, F_{zi} and pre-stress forces $F_{pi,z}$ are equal to:

$$
\begin{aligned}
F_{x1} &= -k_{x1} * (x - h_1\beta - w_1\gamma) \\
F_{y1} &= -k_{y1} * (y + h_1\alpha + d\gamma) \\
F_{z1} &= -k_{z1} * (z + w_1\alpha - d\beta) \\
F_{p1,z} &= \frac{mg}{2}\frac{w_2}{w_1 + w_2} \\
F_{x2} &= -k_{x2} * (x - h_1\beta + w_2\gamma) \\
F_{y2} &= -k_{y2} * (y + h_1\alpha + d\gamma) \\
F_{z2} &= -k_{z2} * (z - w_2\alpha - d\beta) \\
F_{p2,z} &= \frac{mg}{2}\frac{w_1}{w_1 + w_2} \\
F_{x3} &= -k_{x3} * (x - h_1\beta + w_2\gamma) \\
F_{y3} &= -k_{y3} * (y + h_1\alpha - d\gamma) \\
F_{z3} &= -k_{z3} * (z - w_2\alpha + d\beta) \\
F_{p3,z} &= \frac{mg}{2}\frac{w_1}{w_1 + w_2} \\
F_{x4} &= -k_{x4} * (x - h_1\beta - w_1\gamma) \\
F_{y4} &= -k_{y4} * (y + h_1\alpha - d\gamma) \\
F_{z4} &= -k_{z4} * (z + w_1\alpha + d\beta) \\
F_{p4,z} &= \frac{mg}{2}\frac{w_2}{w_1 + w_2}
\end{aligned}
\tag{A-6}
$$

where negative stiffness values in (A-4) are assumed to be added to the horizontal springs.

Putting the forces (A-6) into equations (A-5) and using the assumptions (A-1) and (A-2) one obtains:

$$
\begin{aligned}
\sum F_x = m\ddot{x} = &-x * [k_{x1} + k_{x2} + k_{x3} + k_{x4}] \\
&- \beta * [-h_1(k_{x1} + k_{x2} + k_{x3} + k_{x4})] \\
&- \gamma * [-w_1(k_{x1} + k_{x4}) + w_2(k_{x2} + k_{x3})] \\
\sum F_y = m\ddot{y} = &-y * [k_{y1} + k_{y2} + k_{y3} + k_{y4}] \\
&- \alpha * [h_1(k_{y1} + k_{y2} + k_{y3} + k_{y4})] \\
&- \gamma * [d(k_{y1} + k_{y2} - k_{y3} - k_{y4})] \\
\sum F_z = m\ddot{z} = &-z * [k_{z1} + k_{z2} + k_{z3} + k_{z4}] \\
\sum M_x = J_x\ddot{\alpha} = &-y * [h_1(k_{y1} + k_{y2} + k_{y3} + k_{y4})] \\
&- \alpha * [-mgh_1 + h_1^2(k_{y1} + k_{y2} + k_{y3} + k_{y4}) + w_1^2(k_{z1} + k_{z4}) + w_2^2(k_{z2} + k_{z3})] \\
&- \gamma * [h_1 d(k_{y1} + k_{y2} - k_{y3} - k_{y4})] \\
\sum M_y = J_y\ddot{\beta} = &-x * [-h_1(k_{x1} + k_{x2} + k_{x3} + k_{x4})] \\
&- \beta * [-mgh_1 + h_1^2(k_{x1} + k_{x2} + k_{x3} + k_{x4}) + d^2(k_{z1} + k_{z4} + k_{z3} + k_{z4})] \\
&- \gamma * [h_1(w_1 k_{x1} - w_2 k_{x2} - w_2 k_{x3} + w_1 k_{x4})] \\
\sum M_z = J_z\ddot{\gamma} = &-x * [-w_1(k_{x1} + k_{x4}) + w_2(k_{x2} + k_{x3})] \\
&- y * [d(k_{y1} + k_{y2} - k_{y3} - k_{y4})] \\
&- \alpha * [h_1 d(k_{y1} + k_{y2} - k_{y3} - k_{y4})] \\
&- \beta * [h_1(w_1 k_{x1} - w_2 k_{x2} - w_2 k_{x3} + w_1 k_{x4})] \\
&- \gamma * [w_1^2(k_{x1} + k_{x4}) + w_2^2(k_{x2} + k_{x3}) + d^2(k_{y1} + k_{y2} + k_{y3} + k_{y4})]
\end{aligned}
\tag{A-7}
$$

where the higher order terms are neglected. By partitioning the equations in (A-7), 6x6 stiffness matrix can be found.

Appendix B

B1

B-1 Matlab Code for the Case Study

```
%% Quick System Assessment Method for Active Vibration Isolation Systems
% by: Alper Nizamoglu, 06.06.2015
% [1][Analytical Modeling of Single and Two Stage Vibration Isolation
    Systems by Stephen Moore, 2011]
% [2] Generic Vibration Criteria for Vibration Sensitive Equipment. Colin
    Gordon
% [3] Robust Spectral Approximation of Discrete-Time Frequency Domain
    Power Spectra. Hinnen, Verhaegen, Doelman (PSSSID)

% PART 1: Equations of Motion of a 3D Rigid Body Supported by 4 Springs
    [1]
% PART 2: Closed Loop System with 8 Actuators, 7 Sensors and a Skyhook
    Controller (Generalized Plant)
% PART 3: Floor Vibration and Sensor Noise Modeling [2],[3]
% PART 4: Cumulative Power Spectrum & H2 Norm as Performance Measures

% Parameters to specify for each isolator:
% Spring constants (kp(i), kq(i), kr(i))
% Damping values (cp(i), cq(i), cr(i))
% Location of the Isolators (arm-lengths): Height(h), Depth(d), Width(w1,
    w2)
% Orientation of the isolators (angle of rotation along z: theta(i))
% Geometry of the body: mass(m) and inertia(Ixx,Ixy,Ixz,Iyx,Iyy,Iyz,Izx,
    Izy,Izz)
% Controller Gains (Kv(i))
% Current system is symmetric along X, non-symmetric along Y.

% Since the state space model depends on physical parameters, it can be
    used
% as a Grey-box model. The model can also be used for parameter
```

```
% estimation (pem) or greybox identification (greyid) after a simple modification
% (see pem, greyest, ssest, greyid functions in Matlab).

%%
close all
clc
clear all

%%%%%%%%%%%%%%%%%%%%%%%%%%%%%%%% PART 1 %%%%%%%%%%%%%%%%%%%%%%%%%%%%%%%%%
g = 9810; % [mm/s^2]

%% Define Stiffness along Local Axis:
kp1 = 12;   kq1 = 12;   kr1 = 15.38; % isolator 1 %
kp2 = 12;   kq2 = 12;   kr4 = 15.38; % isolator 2 %
kp3 = 12;   kq3 = 12;   kr3 = 19.7;  % isolator 3 %
kp4 = 12;   kq4 = 12;   kr2 = 19.7;  % isolator 4 %
% Negative Stiffness values are assumed to be added to kpi,kqi

K1 = [kp1 kq1 kr1];
K2 = [kp2 kq2 kr2];
K3 = [kp3 kq3 kr3];
K4 = [kp4 kq4 kr4];

%% Define Damping along Local Axis (approximately between 2-4%)

cp1 = 0.1;   cq1 = 0.1;   cr1 = 0.1; % isolator 1 %
cp2 = 0.1;   cq2 = 0.1;   cr2 = 0.1; % isolator 2 %
cp3 = 0.1;   cq3 = 0.1;   cr3 = 0.1; % isolator 3 %
cp4 = 0.1;   cq4 = 0.1;   cr4 = 0.1; % isolator 4 %

DD1 = [cp1 cq1 cr1];
DD2 = [cp2 cq2 cr2];
DD3 = [cp3 cq3 cr3];
DD4 = [cp4 cq4 cr4];

%% Define Geometric Distances:

% Length along X:
d = 615;   %d = abs(x0 - x(1));
dd = d*2;

% Length along Y:
w2 = 445;   %L1 = abs(y0 - y(3));
w1 = 570;   %L2 = abs(y0 - y(1));
ww = w2 + w1;

% Length along Z:
h= 0; %210;     %h  = abs(z0 - z(1));
hh = 2*h;

%% Mass, Inertia:
```

```

m = 2.1; % in tones

% Inertia is fixed, not varying wrt gravity (real values)
Ixx = 4.8*10^5;  Iyy = 5*10^5;  Izz = 6.4*10^5;

Ixy = 0;         Iyx = 0;       Izx = 0;
Ixz = 0;         Iyz = 0;       Izy = 0;

Inertia = [Ixx -Ixy -Ixz; -Iyx Iyy -Iyz; -Izx -Izy Izz];
Mass = m*eye(3);

%% Rotation of r,p,q for each isolator along z axis only:
% Rotation is allowed only along z because this does not change the equilib

% Angles in degrees:
theta(1) = 0; theta(2) = 0; theta(3) = 0; theta(4) = 0;

%% Find Global M, K, Damp:
% [1] Analytical Modeling of Single and Two Stage Vibration Isolation Systems. Stephen Moore, 2011

% M Matrix: M=[m 0; 0 I]
M = [Mass zeros(3); zeros(3) Inertia]; % (6x6) %

% Finding Global Stiffness and Damping:
[K,Damp,Rp,Rz] = FindK(K1,K2,K3,K4, DD1,DD2,DD3,DD4, d,d,w2,w1,h, theta);
% Look at the end of the code for the function FindK !
% Rp is the position matrix of arm lengths, it is needed to caculate B matrix.
% Rz is the Direction of Cosines Matrix(Rotation), it is needed to calculate B matrix.

%% Add the Gravity Terms to K Matrix due to non-symetrical geometry (caused by h):
% Since the mass is supported below CoG, gravitational field changes the dynamics of the body:

K(4,4) = K(4,4) - (m*g*h);
K(5,5) = K(5,5) - (m*g*h);

% No gravity compensation for Damp because damping is defined 2-3% for each eigenmode.
% With viscous damping ci=0.1 we obtain 2-3% damping for each eigenmode. Hence no compensation needed.

%% Forming A matrix from M,K,Damp:

% A = [0 I; -inv(M)*K -inv(M)*Damp]
A = [zeros(6,6) eye(6,6); -M\K -M\Damp]; % (12x12) %

%% Check Eigenfrequencies:
```

```
[V,eig_val] = eig(K,M);
w = sqrt(diag(eig_val));
f = w/(2*pi);

%% Forming B (input matrix):
% Reference [1]

BB = zeros(6,3,4); % Preallocate for speed
for i=1:1:4
   BB(:,:,i) = [Mass\Rz(:,:,i); Inertia\(Rp(:,:,i)*Rz(:,:,i))]; % (6x3) %
end

B2 = [BB(:,:,1) BB(:,:,2) BB(:,:,3) BB(:,:,4)]; % (6x12) %

% Inputs from all the isolators:
B = [zeros(6,12); B2]; % (12x12) % (12 inputs)

%% Forming C, D:

C = [zeros(6,6) eye(6,6)]; % (6x12) translational and angular velocities of CoG

D = zeros(6,12); % 6 outputs

%% Plant:

G = ss(A,B,C,D); % (6x12) %

%%%%%%%%%%%%%%%%%%%%%%%%%%%%%%%%% PART 2 %%%%%%%%%%%%%%%%%%%%%%%%%%%%%%%%%%

%% Controller:

kvi = 50;

Kv1 = kvi; % x
Kv2 = kvi; % y
Kv3 = kvi; % z
Kv4 = kvi; % Rx % not the rotation in angles scaled version
Kv5 = kvi; % Ry % not the rotation in angles scaled version
Kv6 = kvi; % Rz % not the rotation in angles scaled version

Kv = [Kv1 0 0 0 0 0; 0 Kv2 0 0 0 0; 0 0 Kv3 0 0 0;
      0 0 0 Kv4 0 0; 0 0 0 0 Kv5 0; 0 0 0 0 0 Kv6]; % (6x6) diag Skyhook

%% Motor Matrix (M):

%         Ux  Uy  Uz    Urx     Ury    Urz
Motor = [0.5  0   0     0       0     -0.5;
         0    0   0     0       0      0;
         0    0   0.25  0.25   -0.25   0;
         0    0   0     0       0      0;
```

```
            0    0.5  0      0         0      0;
            0    0    0.25  -0.25  -0.25      0;
            0.5  0    0      0         0    0.5;
            0    0    0      0         0      0;
            0    0    0.25  -0.25   0.25      0;
            0    0    0      0         0      0;
            0    0.5  0      0         0      0;
            0    0    0.25   0.25   0.25      0];    % (12x6) %

%% Sensor Matrix (F):

%            x1   z1    y2   x3   z3   y4    z4
Sensor =  [0.5    0     0   0.5    0    0     0;    % x
             0    0    0.5   0     0   0.5    0;    % y
             0   0.5    0    0    0.5   0     0;    % z
             0    0     0    0   -0.5   0   0.5;    % rx
             0  -0.5    0    0     0    0   0.5;    % ry
          -0.5    0     0   0.5    0    0     0];   % rz   % (6x7) %

%% Inverse Kinematics Matrix (H'):

%             % x y z alpha beta gamma
Transform = [1 0 0    0    -h    -w1; % x1
              0 1 0    h     0     d; % y1
              0 0 1    w1   -d     0;  % z1
              1 0 0    0    -h     w2; % x2
              0 1 0    h     0     d; % y2
              0 0 1   -w2   -d     0;  % z2
              1 0 0    0    -h     w2; % x3
              0 1 0    h     0    -d; % y3
              0 0 1   -w2    d     0; % z3
              1 0 0    0    -h    -w1; % x4
              0 1 0    h     0    -d; % y4
              0 0 1    w1    d     0]; % z4 % (12x6) %

%% Selective Input Matrix (H = H'*Sel):

% After the transformation there are 12 velocities available (4 isolators
    , in 3 axes)
% However, only 7 of them (x1,z1,y2,x3,z3,y4,z4) are available for
    measurement.
% Hence, we need to cancel out the velocities which are not used.

%       x1 y1 z1 x2 y2 z2 x3 y3 z3 x4 y4 z4
Sel = [1   0  0  0  0  0  0  0  0  0  0  0; % x1
        0   0  1  0  0  0  0  0  0  0  0  0; % z1
        0   0  0  0  1  0  0  0  0  0  0  0; % y2
        0   0  0  0  0  0  1  0  0  0  0  0; % x3
        0   0  0  0  0  0  0  0  1  0  0  0; % z3
        0   0  0  0  0  0  0  0  0  0  1  0; % y4
        0   0  0  0  0  0  0  0  0  0  0  1];% z4 % (7x12) % x1,z1,y2,x3,z3
            ,y4,z4 used by ZEISS

```

```
%% Transfer function from velocity to force for 3 DoF of 4 Isolators:

pp = 0.000001; % The pole is not put to zero, instead very close to zero.
% for pp=0 system becomes unstable (very small poles at RHP are observed)

% Isolator 1:
T1 = tf([cp1 kp1],[1 pp]); % transfer function from velocity to force
T2 = tf([cq1 kq1],[1 pp]);
T3 = tf([cr1 kr1],[1 pp]);
Z1 = [T1 0 0; 0 T2 0; 0 0 T3];

% Isolator 2:
T4 = tf([cp2 kp2],[1 pp]);
T5 = tf([cq2 kq2],[1 pp]);
T6 = tf([cr2 kr2],[1 pp]);
Z2 = [T4 0 0; 0 T5 0; 0 0 T6];

% Isolator 3:
T7 = tf([cp3 kp3],[1 pp]);
T8 = tf([cq3 kq3],[1 pp]);
T9 = tf([cr3 kr3],[1 pp]);
Z3 = [T7 0 0; 0 T8 0; 0 0 T9];

% Isolator 4:
T10 = tf([cp4 kp4],[1 pp]);
T11 = tf([cq4 kq4],[1 pp]);
T12 = tf([cr4 kr4],[1 pp]);
Z4 = [T10 0 0; 0 T11 0; 0 0 T12];

Gd = [Z1; Z2; Z3; Z4]; % (12x3) % From Floor Vibration to Force
Gd = minreal(ss(Gd)); % (12x3) %

%% Transfer Functions:

% Open Loop Transmissibility :
Tp = minreal(G*Gd);      % (6x3) %

% From Floor Vibration (w) to CoG (z):
Transfer_wz = Tp; % (6x3) %

% Closed Loop (Velocity to Velocity):

% Sensitivitiy: CoG_vel -> CoG_vel:
Lz = minreal(inv(eye(6,6)+G*Motor*Kv*Sensor*Sel*Transform)); % (6x6) %
%

% From w To z -> Closed Loop Transmissibilities: vel->vel OR pos->pos the
    same:
Gwz = minreal(Lz*Tp); % (6x3) %

% From n To z:
Gnz = minreal(Lz*G*Motor*(-Kv)*Sensor); % (6x7) %

```

```matlab
%%%%%%%%%%%%%%%%%%%%%%%%%%%%%%%%% PART 3 %%%%%%%%%%%%%%%%%%%%%%%%%%%%%%%%%%

%% BBN Criteria:
% [2] Generic Vibration Criteria for Vibration Sensitive Equipment. Colin Gordon

VC_E = 3.12; % 3.12um/s RMS in one-third octave bands
VC_D = 6.25; % 6.25um/s RMS in one-third octave bands
VC_C = 12.5; % 12.5um/s RMS in one-third octave bands
% For a better fit, keep VC Criteria in um/s , do not convert to mm/s (scaling issues..)

VC = VC_D;

% Center Frequencies:
fc = [0.5 0.63 0.79 1 1.26 1.59 2 2.52 3.17 4 5.04 6.35 8 10.08 12.7 16 ...
     20.16 25.4 32 40.32 50.8 64 80.64];

% Using Constant VC Spectrum calculate PSD:
f = 0;
psd = 0;
fgrid = 0.01;
for i=1:1:length(fc)
    bw = fc(i)*0.23; % Proportinal Bandwidth
    psd_amp = (VC^2)/bw;
    ff = fc(i)*0.89:fgrid:fc(i)*1.12; % Equidistant Frequency Gridding for each Bandwidth
    f = horzcat(f,ff);
    psd_vec = psd_amp*ones(1,length(ff));
    psd = horzcat(psd,psd_vec);
end
f = f(2:end); % from 0.45 Hz to 90.49 Hz
psd = psd(2:end);

%% PSSSID:
% [3] Robust Spectral Approximation of Discrete-Time Frequency Domain Power Spectra. Hinnen, Verhaegen, Doelman (PSSSID)

% Weighting Function for PSSSID increase the fit at low frequncies
ww_freq = zeros(1,length(f));
for iii=1:1:length(f)
    ww_freq(iii) = 1/f(iii);
end

[Af1,Bf1,Cf1,Df1] = psssid_alper2(psd,ww_freq,[],4);
% psssid.m just works for matrix PSD. psssid_alper2 is the modification to use it also for scalar psd values
% contact to the writers of [3] for psssid.m

Sid_f1 = evalspec(Af1,Bf1,Cf1,Df1,length(psd));
```

```
% EVALCSPEC evaluates theoretical the powerspectrum S corresponding to the LTI system defined by the quadrupole (A,B,C,D),
% in N+1 equidistant points over the unit circle. Provided by psssid.m
Sid_f1 = squeeze(Sid_f1)';
Sid_f1 = Sid_f1(2:end);

% Compare VC-Spectra with the Colouring Filter
figure;
semilogx(f,psd);
hold on
semilogx(f,Sid_f1,'r');
grid on
title('Model Order of Colouring Filter: n=4')
legend('VC-D Power Spectra','Approimated Power Spectra')
xlabel('Frequency [Hz]')
ylabel('Power[(um/s)š]');

% Calcualte the error in the fit and plot it wrt frequencies:
error_f2 = zeros(1,length(f));
for i=1:1:length(f)
    error_f2(i) = (abs(Sid_f1(i)-psd(i)));
end
figure;
plot(f,error_f2);
title('Absolute Error')

% Convert the colouring filter from discrete time to continuous time:
Ts_F = (90.49-0.45)/(length(f)*fgrid*pi*90.49);
F = minreal(ss(Af1,Bf1,Cf1,Df1,Ts_F));
F = minreal(d2c(F,'tustin'));

% Colouring Filter for Floor Vibration:
F_vib=F;

% Colouring Filter for Sensor Noise:
F_noise = sqrt(20); % 20[(um/s)š/Hz] is the PSD value of VC-D curve at 10 Hz

%%%%%%%%%%%%%%%%%%%%%%%%%%%%%%%%%% PART 4 %%%%%%%%%%%%%%%%%%%%%%%%%%%%%%%%%%

%% H2 norm for the Velocity:

% Response to coloured noise (ground vibration) is the response to white noise for the series interconnection of the system and the colouring filter F(s).
% Y_rms = ||G(s)*F(s)||
%                       2

% Transmissibility (Transfer Function with the Filter):
H2_vel_vib_io = minreal(Gwz(3,:)*eye(3)*F_vib);  % (1x3) % Closed Loop
% Sensor Noise Sensitivity:
```

```
H2_vel_noise_io = minreal(Gnz(3,:)*eye(7)*F_noise); % (1x7) % Noise Sensitivity

% H2 norm of the velocity:
H2_vel_vib = norm(H2_vel_vib_io,2);
H2_vel_noise = norm(H2_vel_noise_io,2);
H2_vel_total = sqrt(H2_vel_vib^2+H2_vel_noise^2);

%% Calculate the Cumulative Power Spectrum for Velocity

format long

% Frequency Points (Check how robust is gridding!):
freq_begin = 0.001; % starting frequency for the calculation of CPS
freq_grid = 0.001; % frequency grid points for CPS
freq_end = 500; % ending frequency of CPS
freq_rms = freq_begin:freq_grid:freq_end;

% Find Frequency Reponse H(jw) at frequency points to calculate CPS: CUM(Syy(jw))
H_vel_vib = freqresp(H2_vel_vib_io,freq_rms,'Hz'); % (1x3) % H(jw)
H_vel_noise = freqresp(H2_vel_noise_io,freq_rms,'Hz'); % (1x7) % H(jw)

% Output PSD: Syy(jw)= H(jw)*Hermitian(H(jw)):
Syy_vel_vib = zeros(1,length(freq_rms)); % Pre-allocate for speed
Syy_vel_noise = zeros(1,length(freq_rms)); % Pre-allocate for speed
Syy_vel_total = zeros(1,length(freq_rms)); % Pre-allocate for speed
for i=1:1:length(freq_rms)
    Syy_vel_vib(i) = (H_vel_vib(:,:,i)*H_vel_vib(:,:,i)'); % 1xlength(rms_freq) %
    Syy_vel_noise(i) = (H_vel_noise(:,:,i)*H_vel_noise(:,:,i)'); % 1xlength(rms_freq) %
    if abs(imag(Syy_vel_vib(i))) > eps || abs(imag(Syy_vel_noise(i))) > eps
        error('HALLO')
    else
        Syy_vel_vib(i) = real(Syy_vel_vib(i));
        Syy_vel_noise(i) = real(Syy_vel_noise(i));
        Syy_vel_total(i) = Syy_vel_vib(i) + Syy_vel_noise(i);
    end
end

%% PSD of Performance Channel due to Floor Vibration and Sensor Noise:

figure;
title('Power Spectral Density of Performance Channel')
xlabel('Frequency [Hz]')
ylabel('PSD [(um/s)š/Hz]')
semilogx(freq_rms,Syy_vel_vib,'r');
hold on;
semilogx(freq_rms,Syy_vel_noise,'g');
hold on;
semilogx(freq_rms,Syy_vel_total,'b');
```

```
legend('Floor Vibration','Sensor Noise','Total')

%% Cumulative Power Spectrum:
XDiff = freq_grid;
Cum_Syy_vel_vib = 2*cumsum(Syy_vel_vib)*XDiff(1); % factor 2 includes negative frequencies
Cum_Syy_vel_noise = 2*cumsum(Syy_vel_noise)*XDiff(1);
Cum_Syy_vel_total = 2*cumsum(Syy_vel_total)*XDiff(1);

%% Compare the CPS and H2 for the velocity:

figure;
semilogx(freq_rms,H2_vel_total^2*ones(1,length(freq_rms)),'k');
hold on;
title('Cumulative Power Spectrum')
xlabel('Frequency [Hz]')
ylabel('Velocity RMS š [um/s]š')
semilogx(freq_rms,Cum_Syy_vel_total,'b');
hold on;
semilogx(freq_rms,Cum_Syy_vel_vib,'r');
hold on;
semilogx(freq_rms,Cum_Syy_vel_noise,'g');
legend('H2š','Total','Floor Vibration','Sensor Noise')

%% Time Simulation Z Floor Vibration Velocity:

H2_CoG_floor_z = norm(Gwz(3,3)*F_vib,2); % From z floor to z CoG

% Create white noise time signal
dt = 10^-4;
t=(0:dt:50);
u3 = sqrt(1/dt)*randn(size(t));

Floor = lsim(F_vib,u3,t);
POB = lsim(Gwz(3,3)*F_vib,u3,t);

% Calculate the standard deviations of floor vibration and CoG displacement
RMS_POB_vel = std(POB);
RMS_Floor = std(Floor);
difference = abs(H2_CoG_floor_z-RMS_POB_vel)/H2_CoG_floor_z % what is the difference in percentage btw. H2 norm and RMS

% Plot the Time Simulations
figure;
plot(t,POB)
hold on
plot(t,Floor,':r')
legend('POB','Floor');
title('POB Velocity vs Floor Velocity')
ylabel('Velocity in Vertical Axis [um/s]')
xlabel('Time [s]')

```

```
%% Integrate the Velocity to Find the Position:

Integ1 = minreal(tf(1,[1 0.01*2*pi]));

Gwz_pos = minreal(Integ1*Gwz(3,:)); % (1x3) %
Gnz_pos = minreal(Integ1*Gnz(3,:)); % (1x7) %

%% H2 Norm for the Position:

% Transmissibility
H2_pos_vib_io = minreal(Gwz_pos*eye(3)*F_vib); % (1x3) %
% Sensor Noise:
H2_pos_noise_io = minreal(Gnz_pos*eye(7)*F_noise); % (1x7) %

% H2 norm of the position:
H2_pos_vib = norm(H2_pos_vib_io,2);
H2_pos_noise = norm(H2_pos_noise_io,2);
H2_pos_total = sqrt(H2_pos_vib^2+H2_pos_noise^2);

%% Time Simulation Z Floor Vibration Displacement (Similar to Velocity):

H2_POB_floor_z_pos = norm(Gwz_pos(1,3)*F_vib,2); % from floor vibration
    in z to CoG displacement in z

dt = 10^-5;
t=(0:dt:120);
u3 = sqrt(1/dt)*randn(size(t));

Floor = lsim(F_vib,u3,t);
POB = lsim(Gwz_pos(1,3)*F_vib,u3,t);

RMS_POB_pos = std(POB);
RMS_Floor = std(Floor);
difference = abs(H2_POB_floor_z_pos-RMS_POB_pos)/H2_POB_floor_z_pos

figure;
plot(t,POB)
title('POB Motion')
ylabel('Position in Vertical Axis [um]')
xlabel('Time [s]')
```

```matlab
function [K,Damp,R0,R_z] = FindK(K1, K2, K3, K4, D1, D2, D3, D4, d1, d2, w2, w1, h, theta)

%% Translational Stiffness for 4 Isolators:

% x,y,z spring constants of the 4 Isolators
kp(1) = K1(1); kq(1) = K1(2); kr(1) = K1(3);
kp(2) = K2(1); kq(2) = K2(2); kr(2) = K2(3);
kp(3) = K3(1); kq(3) = K3(2); kr(3) = K3(3);
kp(4) = K4(1); kq(4) = K4(2); kr(4) = K4(3);

K_trans = zeros(3,3,4); % Preallocate for speed
for i=1:1:4
    K_trans(:,:,i) = [kp(i) 0 0; 0 kq(i) 0; 0 0 kr(i)];
end

%% Translational Damping for 4 Isolators:

% x,y,z spring constants of the 4 Isolators
cp(1) = D1(1); cq(1) = D1(2); cr(1) = D1(3);
cp(2) = D2(1); cq(2) = D2(2); cr(2) = D2(3);
cp(3) = D3(1); cq(3) = D3(2); cr(3) = D3(3);
cp(4) = D4(1); cq(4) = D4(2); cr(4) = D4(3);

D_trans = zeros(3,3,4); % Preallocate for speed
for i=1:1:4
    D_trans(:,:,i) = [cp(i) 0 0; 0 cq(i) 0; 0 0 cr(i)];
end

%% Point of Action for 4 Isolators wrt CoG:

% pos0 = ([xi;yi;zi], i = #isoaltor)

pos0(1,1) = d1;   pos0(1,2) = d1;   pos0(1,3) = -d2;    pos0(1,4) = -d2;    %X
pos0(2,1) = w1;   pos0(2,2) = -w2;  pos0(2,3) = -w2;    pos0(2,4) = w1;     %Y
pos0(3,1) = -h;   pos0(3,2) = -h;   pos0(3,3) = -h;     pos0(3,4) = -h;     %Z

%% Relative positions of isolators wrt CoG (matrix form):

R0 = zeros(3,3,4); % Preallocate for speed
for i=1:1:4
    R0(:,:,i) = [0 -pos0(3,i) pos0(2,i);
                pos0(3,i) 0 -pos0(1,i);
                -pos0(2,i) pos0(1,i) 0];
end

%% Rotation of r,p,q (elastic axis) along z axis (Direction of cosines):

% Matrix of direction of cosines (Rotation Matrix):
R_z = zeros(3,3,4); % Preallocate for speed
```

```
for i=1:1:4
   R_z(:,:,i) = [cosd(theta(i)) sind(theta(i)) 0;
                 -sind(theta(i)) cosd(theta(i)) 0;
                 0 0 1];
end

%% Find K (Stephen Moore, 2011 -Analy. Modeling of Single and Two Stage
    Vibration Isolation Systems-):

KK = zeros(3,3,4); % Preallocate for speed
for i=1:1:4
   KK(:,:,i) = R_z(:,:,i)*K_trans(:,:,i)*transpose(R_z(:,:,i));
end

%K = [K11 K12; K21 K22]:
K11 = zeros(3); % Preallocate for speed
K12 = zeros(3); % Preallocate for speed
K22 = zeros(3); % Preallocate for speed

for i=1:1:4
   K11 = K11 + KK(:,:,i);
   K12 = K12 + KK(:,:,i)*transpose(R0(:,:,i));
   K22 = K22 + (R0(:,:,i)*KK(:,:,i)*transpose(R0(:,:,i)));
end
K21 = transpose(K12);

K = [K11 K12; K21 K22];

%% Find Damp (Same calculations as in finding K):

DD = zeros(3,3,4); % Preallocate for speed
for i=1:1:4
   DD(:,:,i) = R_z(:,:,i)*D_trans(:,:,i)*transpose(R_z(:,:,i));
end

%Damp = [D11 D12; D21 D22]:
D11 = zeros(3); % Preallocate for speed
D12 = zeros(3); % Preallocate for speed
D22 = zeros(3); % Preallocate for speed

for i=1:1:4
   D11 = D11 + DD(:,:,i);
   D12 = D12 + DD(:,:,i)*transpose(R0(:,:,i));
   D22 = D22 + (R0(:,:,i)*DD(:,:,i)*transpose(R0(:,:,i)));
end
D21 = transpose(D12);

Damp = [D11 D12; D21 D22];

end
```

Bibliography

[1] J. V. Wagoner, “How does extreme unltraviolet photolithography work.” `www.quora.com/How-does-Extreme-Ultraviolet-Photolithography-work`, November 2013. [Online; accessed 19-Oct-2014].

[2] W. J. Zwetsloot, “Design of active vibration isolation systems with power spectrum disturbance models,” Master’s thesis, Delft University of Technology, December 2014.

[3] S. Moore, “Analytical modelling of single and two-stage vibration isolation systems,” in *Proceedings of Acoustics 2011*, November 2011.

[4] A. Barzilai, T. VanZandt, and T. Kenny, “Technique for measurement of the noise of a sensor in the presence of large background signals,” *Review of Scientific Instruments*, vol. 69, no. 7, pp. 2767–2772, 1998.

[5] C. G. Gordon, “Generic vibration criteria for vibration-sensitive equipment,” in *SPIE’s International Symposium on Optical Science, Engineering, and Instrumentation*, pp. 22–33, International Society for Optics and Photonics, 1999.

[6] M. Rothschild, M. W. Horn, C. L. Keast, R. R. Kunz, V. Liberman, S. C. Palmateer, S. P. Doran, A. R. Forte, R. B. Goodman, J. H. Sedlacek, *et al.*, “Photolithography at 193 nm,” *Lincoln Laboratory Journal*, vol. 10, no. 1, 1997.

[7] `https://www.youtube.com/watch?v=8gf_9sa0zms`. [Online; accessed 16-July-2014].

[8] `http://www.zeiss.com/semiconductor-manufacturing-technology/en_de/products-solutions/semiconductor-manufacturing-optics/about-optical-lithography/moore_s-law.html`. [Online; accessed 17-July-2014].

[9] `https://www.youtube.com/watch?v=WbukKUi3vHw`. [Online; accessed 14-July-2014].

[10] G. W. v. d. Poel, *An exploration of active hard mount vinration isolation for precision equipment.* PhD thesis, Universiteit Twente, may 2010.

[11] D. Tjepkema, *Active hard mount vibration isolation for precision equipment.* University of Twente, 2012.

[12] E. Berkman and E. Bender, "Perspectives on active noise and vibration control," *Sound and vibration*, vol. 31, no. 1, pp. 80–101, 1997.

[13] L. Zuo and J.-J. E. Slotine, "Robust vibration isolation via frequency-shaped sliding control and modal decomposition," *Journal of Sound and Vibration*, vol. 285, no. 4, pp. 1123–1149, 2005.

[14] N. L. Wilson, *Semi-active six degree of freedom vibration control.* PhD thesis, University of Maryland, 2012.

[15] M. L. G. Boerlage, *Rejection of disturbance in multivariable motion systems.* PhD thesis, Eindhoven University of Technology, September 2008.

[16] M. H. M. Dassen, "Multivariable control and blind disturbance identification," Master's thesis, Eindhoven University of Technology, August 2006.

[17] O. Y. Baytemir, "Development of a passive vibration analysis and optimization software for mechanical systems," Master's thesis, Middle East Technical University, September 2013.

[18] N. G. M. Rademakers, "Modelling identification and multivariable control of an active vibration isolation system," Master's thesis, Eindhoven University of Technology, June 2005.

[19] L. E. Smollen, "Generalized matrix method for the design and analysis of vibration-isolation systems," *Acoustical Society of America Journal*, vol. 40, p. 195, 1966.

[20] M. Griffis and J. Duffy, "Global stiffness modeling of a class of simple compliant couplings," *Mechanism and Machine Theory*, vol. 28, no. 2, pp. 207 – 224, 1993.

[21] "Geospace technologies." `http://www.geospace.com/geophones-gs-11d/`. [Online; accessed 23-July-2014].

[22] E. E. Ungar, D. H. Sturz, and C. H. Amick, "Vibration control design of high technology facilities," *Sound and Vibration*, vol. 24, no. 7, pp. 20–27, 1990.

[23] H. Amick, "On generic vibration criteria for advanced technology facilities: with a tutorial on vibration data representation," *Journal of the IES*, vol. 40, no. 5, pp. 35–44, 1997.

[24] B. Priedham, "Assessment of ground-borne vibration impacts on sensitive facilities," in *Proceedings of the IMAC-XXVII*, February 2009.

[25] `http://www.zeiss.com/semiconductor-manufacturing-technology/en_de/products-solutions/semiconductor-manufacturing-optics/about-optical-lithography/moore_s-law.html`. [Online; accessed 21-April-2014].

[26] R. Schmidt, G. Schitter, and J. van Eijk, *The Design of High Performance Mechatronics: High-tech Functionality by Multidisciplinary System Integration.* Delft University Press, 2011.

[27] L. Jabben and J. v. Eijk, “Performance analysis and design of mechatronic systems,” *Mikroniek*, vol. 51, no. 2, pp. 5–12, 2011.

[28] B. Bakker and J. v. Seggelen, “The revolutionary hummingbird technology,” *Mikroniek*, vol. 50, no. 2, pp. 14–20, 2010.

[29] L. Jabben, *Mechatronic Design of a Magnetically Suspended Rotating Platform.* PhD thesis, Delft University of Technology, December 2007.

[30] P. Weustink, “Automating dynamic error budgeting,” *Mikroniek*, vol. 52, no. 1, pp. 20–24, 2012.

[31] R. Toscano, *Structured Controllers for Uncertain Systems: A Stochastic Optimization Approach.* Advances in Industrial Control, Springer London, 2013.

[32] “H2 optimal control.” `http://www.mathematik.uni-stuttgart.de/studium/infomat/mst/linearekontrolltheorie/folien/lec8.pdf`. [Online; accessed 20-July-2014].

[33] K. Hinnen, M. Verhaegen, and N. Doelman, “Robust spectral factor approximation of discrete-time frequency domain power spectras,” *Automatica*, vol. 41, no. 10, pp. 1791–1798, 2005.

[34] A. H. Slocum, *Precision machine design.* Society of Manufacturing Engineers, 1992.

[35] T. t. Dam and R. v. d. Kruk, “Towards the practical application of dynamic error budgeting,” *Mikroniek*, vol. 50, no. 5, pp. 52–56, 2010.

[36] L. Ljung, “Asymptotic behavior of the extended kalman filter as a parameter estimator for linear systems,” *Automatic Control, IEEE Transactions on*, vol. 24, no. 1, pp. 36–50, 1979.

[37] M. Steinbuch, R. Van De Molengraft, and A. van der Voort, “Experimental modelling and LPV control of a motion system,” in *American Control Conference, 2003. Proceedings of the 2003*, vol. 2, pp. 1374–1379, IEEE, 2003.

Glossary

List of Acronyms

PCB	Printed Circuit Board
IC	Integrated Circuits
UV	Ultra-violet
EUV	Extreme Ultra-Violet
SMT	Semi-Manufacturing Technology
GmbH	Gesellschaft mit beschränkter Haftung
POB	Projective Optics Box
FRF	Frequency Response Functions
AVIS	Active Vibration Isolation System
DOF	Degree of Freedom
MIMO	Multi-input Multi-output
SISO	Single-input Single-output
CPS	Cumulative Power Spectrum
SDOF	Single Degree of Freedom
3D	3 Dimensional
PSD	Power Spectral Density
FEM	Finite Element Modelling
CoG	Center of Gravity
2D	2 Dimensional

PVIS	Passive Vibration Isolation System
VC-curves	Vibration Criteria Curves
RMS	Root Mean Square
PSSSID	Power Spectrum SubSpace IDentification
MISO	Multi-input Single-output
CSD	Cross Spectral Density
DEB	Dynamic Error Budgeting
LPV	Linear Parametric Varying